DEVELOPMENT AND TESTING OF POSITRON IDENTIFICATION BY COINCIDENT ANNIHILATION PHOTONS (PICAP)

BY

DAN L. TRAN

BA in Astronomy and Physics, Boston University, 2008

DISSERTATION

Submitted to the University of New Hampshire
in partial fulfillment of
the requirements for the degree of

Doctor of Philosophy

in

Physics

May, 2019

This dissertation has been examined and approved in partial fulfillment of the requirements for the degree of Doctor of Philosophy in Physics by:

Dissertation Director, James J. Connell
Associate Professor of Physics

Clifford Lopate
Research Associate Professor of Physics

Mark McConnell
Professor of Physics

Kai Germaschewski
Associate Professor of Physics

Karl Slifer
Associate Professor of Physics

On April 12, 2019

Original approval signatures are on file with the University of New Hampshire Graduate School.

DEDICATION

To my loving parents and family.

My opportunity simply does not exist without their struggle, diligence, perserverance and eventual triumphant success as immigrants in this country. And it is truly an inspiration.

And to the late John McCarthy.

Whose science classroom I will always remember fondly.

Acknowledgments

I would first and foremost like to thank my advisor, Dr. James Connell. While it is obvious that Jim's vast knowledge and experience in the research were of utmost importance, it was his empathy and patience with me that I personally valued the most while being guided through the process.

Speaking of patience, I owe much gratitude to my dissertation committee: Dr. Clifford Lopate, Dr. Mark McConnell, Dr. Karl Slifer, and Dr. Kai Germaschewski. I have tremendous respect for what they do and am grateful for agreeing to a part of my committee.

I would like to give special thanks to Brendan Bickford (BS, UNH '12) and Samuel Galletta (BS, UNH '12) for their roles in bringing PICAP to life. Brendan built it with his mechanical engineering background. Sam helped us understand it by configuring the data acquisition software. When I first started, I relied heavily on the paper that introduced me to PICAP, co-written by Jason Kalainoff (MS, UNH '04). I am grateful to his previous work and proud to have taken up the mantle after him.

Ethan Cascio was our beam operator and liaison at Massachusetts General Hospital's Francis H. Burr Proton Beam Therapy Center. Dr. Daniel Dale and Dr. Tony Forest were our main points of contact and support at the Idaho Accelerator Center at Idaho State University. This work would not be possible without them.

Sincere thanks to the Dan Young, Brendan Harris, Paul Aliotta, Matt Gorby, Carol Weaver, Max Grady, Toby Badman, Kris Maynard, Ryan Zielinski, Ian Cohen, Alex Boyd, Amanda Madden, Zhongwei Dai, John McClain, and Fathima Muzleena Muzamil for always inspiring me and being the rock stars that you guys all are.

The Graduate Student Senate helped me hone my graduate student voice and discover my engagement with the graduate community. The many iterations of trivia teams that I played on (and trivia rivals) offered me an outlet to vent, while crushing our opponents using our collective knowledge of useless facts.

I called Dover, NH home for four years, and in many ways, it was the home I needed away from home (especially 60 Hill).

To all of the strong friendships and bonds that I have made during my time at the University of New Hampshire. I am glad to have called you a friend at any point of our time knowing (and still knowing) each other. This includes roommates, fellow graduate students, students that I have taught, former students turned graduate students and more... I appreciate your love and support, and the opportunity to struggle through the process, grow, and emerge above it all with all of you.

Thank you to Steve St. Pierre and Narin Frichitthavong, the finest barbers I know, for helping me rediscover my inner confidence while giving me a reason to embrace my outer confidence.

And finally... I would like to thank Dan, Stu, Cote, Mike, Guillermo, Chris, Roy, and Allyson for always giving me something to laugh at and helping to keep me sane.

TABLE OF CONTENTS

List of Tables

List of Figures

ABSTRACT

Development and Testing of Positron Identification by Coincident Annihilation Photons (PICAP)

by

Dan L. Tran

University of New Hampshire, May, 2019

Moderate energy positrons (∼few–10 MeV) have seldom been observed in the Heliosphere, due largely to the lack of dedicated instruments. Deep-space measurements of these positrons would have implications in the study of Solar energetic particle events and the transport and modulation of Galactic cosmic rays in the Heliosphere. Positron Identification by Coincident Annihilation Photons (PICAP) is a detector scheme to measure these positrons by simultaneously detecting the two 0.511-MeV γ-ray photons emitted from negatron-positron annihilation of stopping positrons. PICAP is intended for deep-space missions with severe limits on mass, power, and telemetry. This dissertation details the development and testing of a prototype to prove PICAP's viability and performance. Monte Carlo modeling provided expected instrument response. Based on the modeling, a prototype was built. On 1 June 2013, the prototype was tested at the Burr Proton Therapy Center to demonstrate PICAP's ability to discriminate protons from positrons (and electrons). Exposure to energetic protons ranging from 69.6 MeV through 214.9 MeV showed that protons were misidentified as electrons on the order of few per 10^5 and misidentified as positrons on the order of few per 10^6, indicating a high rejection rate for protons. On 9–10 December 2013, the prototype was tested at the Idaho Accelerator Center to determine the response to negatrons and positrons with energies between 4 and 9 MeV. Unforeseen experimental circumstances prevented event-by-event identification of particles, so a maximum likelihood statistical analysis was developed. We showed

for several particle energies that positrons were identified with >5-σ statistical accuracy. The probability of positron measurement was consistent with zero when exposed to negatrons and within a factor of two of the Monte Carlo data when exposed to positrons. Agreement between experimental and simulation data thus confirmed that PICAP can make the required measurements. As a result of this work, the PICAP's NASA Technology Readiness Level (TRL) was advanced from Level 3 to Level 5, where it can be proposed for future space missions.

Chapter 1

Purpose

1.1 Introduction

The Positron Identification by Coincident Annihilation Photons (PICAP) system is a simple, innovative detector scheme designed for the identification of moderate energy (∼few to 10 MeV) positrons [Connell et al., 2008]. Positrons at these energies have never been definitively observed in space, yet their measurement would have implications in the study of the transport and modulation of Galactic cosmic rays in the Heliosphere as well as Solar energetic particle events.

When discussing positrons, it is important to use nomenclature that adequately describes all other possible measurements, and especially when space instrumentation is used, there are measurement techniques that cannot distiguish particles of opposite charge. We have adopted terminology commonly used in space measurements, defining negatively charged leptons of mass 0.511 MeV/c^2 as "negatrons" and positively charged leptons of the same mass as "positrons." The term "electron" refers to any lepton of mass 0.511 MeV/c^2, regardless of charge; thus, an electron is either a negatron *or* a positron.

To date, positron measurements in space have largely been made with magnetic spectrometers at significantly greater energy (at least tens of MeV up to a few TeV). PICAP does not employ a magnet. It identifies a particle's mass by measuring the energy that it deposits as it penetrates a cylindrical stack of detector elements before depositing its remaining energy and stopping, a technique referred to as dE/dx vs. E' (energy loss vs. residual energy). When positrons stop and encounter their antiparticle, the negatron, they annihilate, resulting in the emission of two 0.511-MeV gamma (γ) ray photons, moving in opposite directions. If both photons can be measured, it serves as a direct way to detect the presence of a positron.

The concept was originally inspired by the ATLAS Positron EXperiment (APEX), a spectrometer constructed at Argonne National Laboratory's ATLAS Accelerator Facility [Ahmad et al., 1996]. APEX was designed to study the production of negatrons and positrons in heavy-ion collisions. The instrument consisted of a solenoid, mounted perpendicular to the incident beam line (represented by a magnetic field B in Figure 1-1), which guided negatrons and positrons away from the beam target towards arrays of 198 one-mm thick silicon (Si) detectors. The purpose of each array, oriented along the axis of the solenoid, was to determine the angle of emission from the collision, time-of-flight, and energy of the particles. Each Si array was surrounded by a cylindrical array of 24 sodium iodide (NaI) scintillator segments, forming a "barrel" of detectors. A positron is identified when it stops in the Si array in coincidence with the detection of two 0.511-MeV γ-rays in two opposing elements of the NaI barrel. The particular experiment that inspired PICAP was the observation of the β^+ decay of manganese-54 (^{54}Mn), during which the positron detection efficiency of the APEX was determined to be 2%, reported in Wuosmaa et al. [1998].

Conceived in 2007, the PICAP system operates in a manner similar to the Si and NaI array portions of the APEX, but with a simpler and smaller design, optimized for moderate-energy positron and electron detection [Connell et al., 2008]. PICAP is intended to be the base design of a low-mass, low-power, and low-cost space-flight instrument. As part of a suite of instruments on a satellite, for example, a PICAP-type instrument could be a suitable option for deep-space missions beyond Earth's magnetosphere, where particles with these energies are primarily accessible, but where resources such as power and mass are severely limited.

In this chapter, the motivation behind a PICAP-type instrument and its scientific impact are

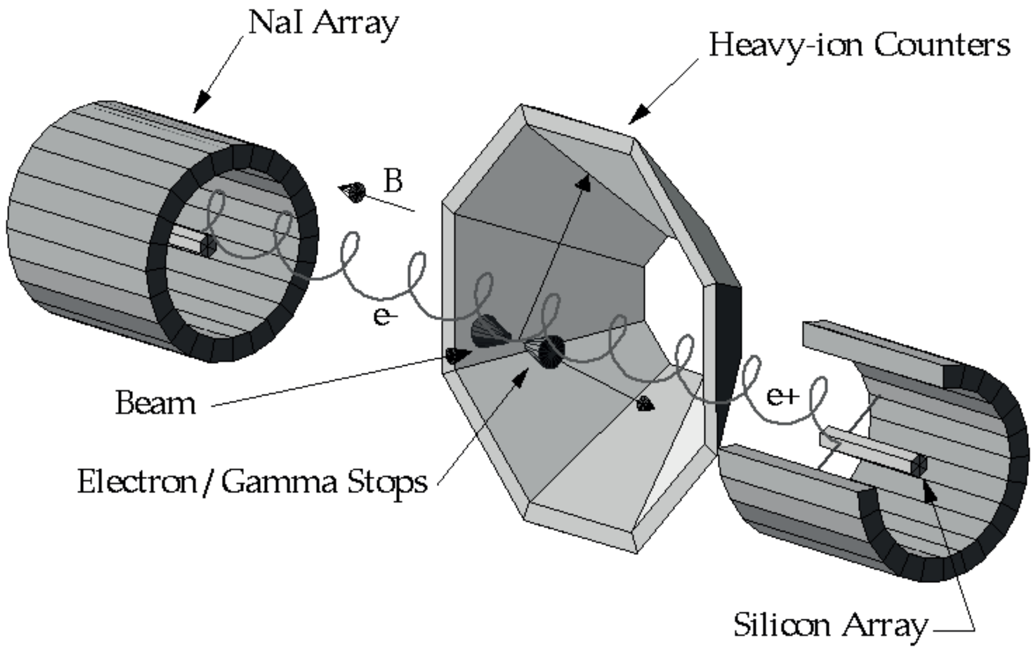

Figure 1-1: Schematic drawing of the ATLAS Positron EXperiment (APEX) from [Ahmad et al., 1996]. APEX was an inspiration for the PICAP system, particularly the toroidal array of NaI used for detecting annihilation radiation from positrons stopping in the Si array.

discussed. We also present a partial history of positron measurements that have been reported, and the instruments that were used to obtain them, with emphasis on simiarities to PICAP's particle detection techniques. Finally, the goals of this disseration are briefly presented, outlining the characterization of the PICAP system, evolving from a theoretical computer model, to its proof-of-concept as a working prototype instrument.

1.2 Scientific Motivation

Galactic cosmic rays (GCRs) are energetic charged particles, mainly nuclei of hydrogen (i.e. protons) and heavier atoms, originating from outside of the Solar System. The exact source of cosmic rays is unclear, though whatever the source, the particles propagate through the interstellar medium (ISM) for millions of years before arriving at the Solar System [Simpson, 1983]. Positrons are mainly secondary products of cosmic ray proton interactions with the ISM and studying them furthers understanding of the propagation history of cosmic rays. To be detected by instruments within the Solar System, they must pass into and through the Heliosphere, where, subject to the outward flow of the Solar wind plasma and the complex Solar magnetic field, GCRs undergo spatial and temporal variations in their intensity and energy. This is known as cosmic ray modulation [Potgieter, 2013].

The general structure of the Solar wind plasma and magnetic fields that fill the Heliosphere, first presented by Parker [1965], guides interplanetary charged particle motion. Theories emerged with models predicting that charged particle drifts have an overall effect on Solar modulation (notably in [Jokipii et al., 1977]). In particular, predictions were made on how cosmic ray flux time-intensity profiles vary between Solar magnetic cycles, characterized by the orientation and reversal of the Sun's magnetic field direction [Jokipii and Levy, 1977]. Charge-sign effects were investigated since models predicted opposite drift patterns for positively and negatively charged particles. To date, such charge-sign effects have been studied by comparing electrons with protons (or heavier ions such as helium). While simultaneous observations of electrons and positive ions supported general predictions, the sharpness of the peaks in their time-intensity profiles differed [Clem et al., 2000]. Due to the difference in electron and proton mass, it is not possible to simultaneously match their energy, rigidity and velocity. Thus, it is uncertain if the difference between the modulation of positive and negative particles should be attributed to charge-sign effects, modulation effects that depend on the particle velocities, or some transient phenomena. Additionally, prior electron measurements did not distinguish between negatrons and positrons, both counting as electrons and confusing the issue since the exact positron fraction was unknown [Connell et al., 2008].

PICAP would be able to compare negatrons and positrons, with identical rigidity, energy, and velocity. Because a PICAP instrument could be built for space-flight, fluxes could also be measured continuously over long periods, allowing for the study of short- and long-term variations in charge-sign dependence of Solar modulation [Connell et al., 2008]. Such extended measurements are needed to study 11- or 22-year effects over Solar cycles.

During Solar particle events (SPEs), charged particles originating from the Sun are energized at sites, such as flares, or at shocks often driven by a coronal mass ejection. Models have been developed to predict the energy spectra and time-intensity profile of particles produced via the acceleration of a lower energy seed population through various processes [Reames, 1999; Cane and Erickson, 2003]. Validation of these acceleration models require several input parameters based on observational data, such as accurate measurement of different particle populations. The parameters required as input for modeling particle production in SPEs (e.g, hydrogen density, magnetic field, temperature) also effect positron production, as they are only created as secondary particles from high-energy interactions at acceleration sites during SPEs. Measuring the positron flux would help to constrain such models.

High-energy interactions at SPE sites create unstable isotopes [Share and Murphy, 1995], including nuclides which decay via β^+ emission. They also lead to π^+ production, which decay to positrons. Positron production has been identified via observations of the 0.511-MeV annihilation spectral line, first reported for the flare on 4 August 1972 [Chupp et al., 1973] and observed since [Yoshimori et al., 2001]. The strength of the line depends on the number of positrons created, less any that escape. The number of positrons created depends on the production of isotopes and pions resulting from the energization processes that occur during an SPE. The line results from the formation and annihilation of positronium between a positron and negatron [Ramaty et al., 1983].

Observing the strength of the 0.511-MeV annihilation line is insufficient to fully gauge positron production in SPEs. Positrons originating from β^+ emitting isotopes have an energy of $\sim$few MeV, which are likely to form positronium with the ambient material in the Sun [Ramaty et al., 1983]. If produced sufficiently deep in the Solar atmosphere, they would likely not escape and contribute to the 0.511-MeV annihilation line [Murphy et al., 1987]. However, positrons emitted from π^+ decay start with energies ranging 10's to 100's of MeV, of which some may escape the Solar atmosphere into interplanetary space. These have yet to be conclusively identified.

Escaping positrons would have an energy of at least ~few MeV, which is in the energy range of positrons a PICAP instrument is designed to detect. Alongside the 0.511-MeV positronium annihilation line, measurement of escaped positrons (or even a negative result) would provide more complete insight on charged particle acceleration, production and escape during an SPE, and further constrain prediction models [Connell et al., 2008].

1.3 History Of Positron Measurements In Space

In 1969, low- to moderate-energy positron measurements were reported from observations made with instruments aboard the OGO-3 and OGO-5 satellites, launched in 1966 and 1968, respectively. The instrument on the OGO-3 featured a central scintillation detector where the positrons stopped and annihilated [Cline and Hones, 1970]. The stopping detector, labeled "C" in Figure 1-2, was flanked by two CsI γ-ray scintillation detectors ("A" and "B"). A coincidence of a 0.511-MeV signal in both γ detectors, combined with a signal of a particle stopping in the central detector, indicated the detection of a positron. It was concluded that the observations from the OGO-3 instrument indicated the detection of positrons with energies of ~0.5 to few MeV. The authors suggested that these positrons were of cosmic-ray origin but could not definitively explain the intensity of observations.

The instrument on OGO-5 consisted again of a central detector for stopping charged particles but also included a penetrating dE/dx scintillation detector at the top of the stack for particle identification, particularly for separation of electrons and protons (see Figure 1-3; [Cline and Porreca, 1970]). Positrons were distinguished from negatrons with a 0.511-MeV signal in just a single γ-ray detector, instead of the two featured on the OGO-3 instrument. Positrons of energies 2–9.5 MeV were observed, also deemed to be of cosmic-ray origin, from which the positron fraction was measured to be 1.8 ± 0.2 %.

The PICAP design shares elements from both OGO-bourne instruments; however, where PICAP

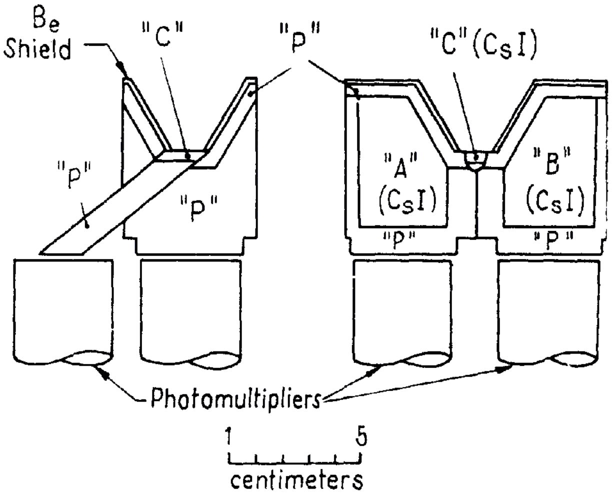

Figure 1-2: A schematic of the detector aboard the OGO-3 satellite [Cline and Hones, 1970]. Positrons stop in "C" and produce 0.511-MeV annihilation radiation to be detected in "A" and "B." "p" is an anticoincidence shield.

is different is that it uses multiple dE/dx detectors and four γ-ray detectors for the annihilation radiaton.

Positrons were further explored with two nearly identical Electron/Isotope Spectrometers (EIS) on the IMP-7 and IMP-8 satellites, launched in 1972 and 1973, respectively, mainly for observations of low-energy (0.2–2 MeV) Solar-flare negatrons [Hurford et al., 1973; Mewaldt et al., 1975]. EIS consisted of a stack of eleven silicon solid-state disc detectors (called D0–D10), surrounded by an anticoincidence shield of scintillator (Figure 1-4). D0, D1, D3, and D4 were annular, which served as a collimator in a narrow geometry mode. Conversely, in the wide geometry mode, events that triggered D0 without penetrating D10 (the bottom detector) and the anticoincidence shield were analyzed. Particles are identified with dE/dx vs. E' techniques, in a manner similar to that mentioned for the OGO-5 instrument. Positrons were identified by a trigger in D0 in coincidence with one 0.511-MeV signal in another detector. Positron detection in EIS was low compared to other instruments, because the 0.511-MeV signal from the γ-rays was being measured by silicon solid-state detectors that, as explained later, have a low γ-ray scattering cross-section, due to silicon's low atomic charge z. Additionally, only a single 0.511-MeV signal was required. PICAP

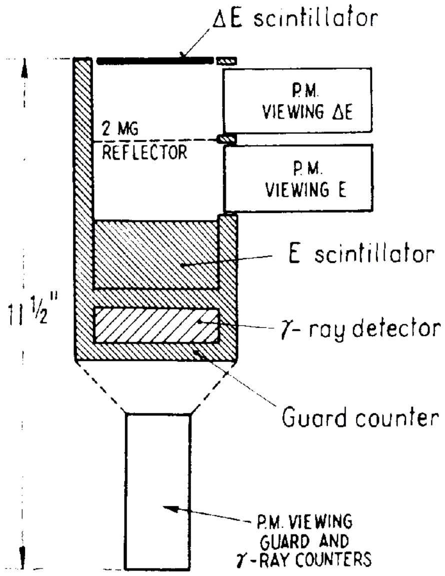

Figure 1-3: A cross-sectional schematic of the detector aboard the OGO-5 satellite. δE and E are plastic scintillation detectors, under which is a CsI γ-ray detector (referred to as “C”) and enclosed in a guard counter, similar to an anticoincidence shield (referred to as “p”) [Cline and Porreca, 1970].

requires the detection of both 0.511-MeV γ-rays in its most stringent mode.

Positrons with energies on the order of a few hundred keV were reported as possibly detected for the solar flare on 3 June 1982 with the MPAe instrument aboard the Helios-1 spacecraft [Kirsch et al., 1985]. MPAe was designed to measure ions, electrons, and positrons by separating them with an inhomogeneous magnetic field and directing them towards different solid-state detectors, each accompanied by an anticoincidence detector. The positron channels were disturbed by other particles that were penetrating the instrument’s shielding and could not be eliminated with anticoincidence; therefore, positrons could only be separated from the background before the main arrival of flare protons. This point was taken to have occurred some few hundred seconds after the start of nuclear interaction and production of positron emitters during the observation interval. From the detection of positrons by the instrument on Helios-1 at 0.57 AU, the flux was extrapolated to 1 AU with the conclusion that $\leq 10\%$ of positrons generated in the photosphere escape into space. The positron energy range for MPAe was 152–546 keV, which is well below PICAP’s intended range of

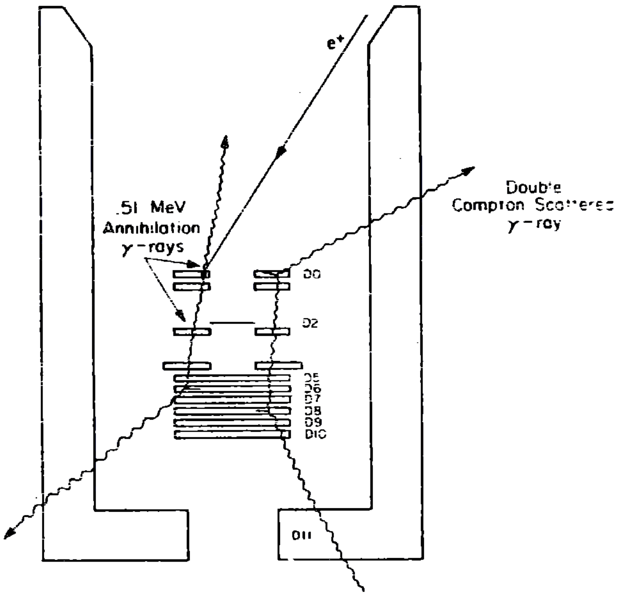

Figure 1-4: A cross-sectional schematic of the EIS Spectrometers flown on IMP-7 and IMP-8. The diagram illustrates the detection of a positron stopping in the top annular detector (D0) and the subsequent Compton scatter of one of the annilhilation photons in one of several other detectors in the stack. [Hurford et al., 1973; Mewaldt et al., 1975]

operation.

Presently, ongoing positron measurements in space are made with magnetic spectrometers, which track the trajectory and curvature of a particle for identification. Examples of such instruments in space are the Payload for Antimatter Matter Exploration and Light-nuclei Astrophysics (PAMELA), launched in June 2006 on the Resurs DK1 satellite and, more recently, the Alpha Magnetic Spectrometer (AMS-02), installed in May 2011 on the International Space Station. PAMELA's particular focus is on antiparticles, with design goals of measuring positrons ranging from 50 MeV to 270 GeV as well as the combined negatron and positron spectrum up to 2 TeV [Picozza et al., 2007]. To date, measurements for positrons with energies greater than several hundred MeV have been reported from PAMELA [Galper et al., 2017], related to observing charge-sign Solar modulation effects of cosmic rays [Adriani et al., 2016]. AMS-02 has measured the cosmic-ray positron fraction in the energy range of 0.5 to 350 GeV [Aguilar et al., 2013], further adding to observations made with PAMELA.

While both are highly advanced and capable, PAMELA and AMS-02 are extremely massive (430 kg and 6,800 kg, respectively) and require significant amounts of power (335 W and up to 2,500 W, respectively) [Picozza et al., 2007; Kounine, 2012], making them impractical to take beyond near-Earth orbit into deep space. These and similar instruments, compared in Figure 1-5 from an AMS Collaboration press release in 2013 [AMS, 2013], also measure the positron fraction at higher energy regimes, while PICAP is aimed at a rarely explored lower energy range.

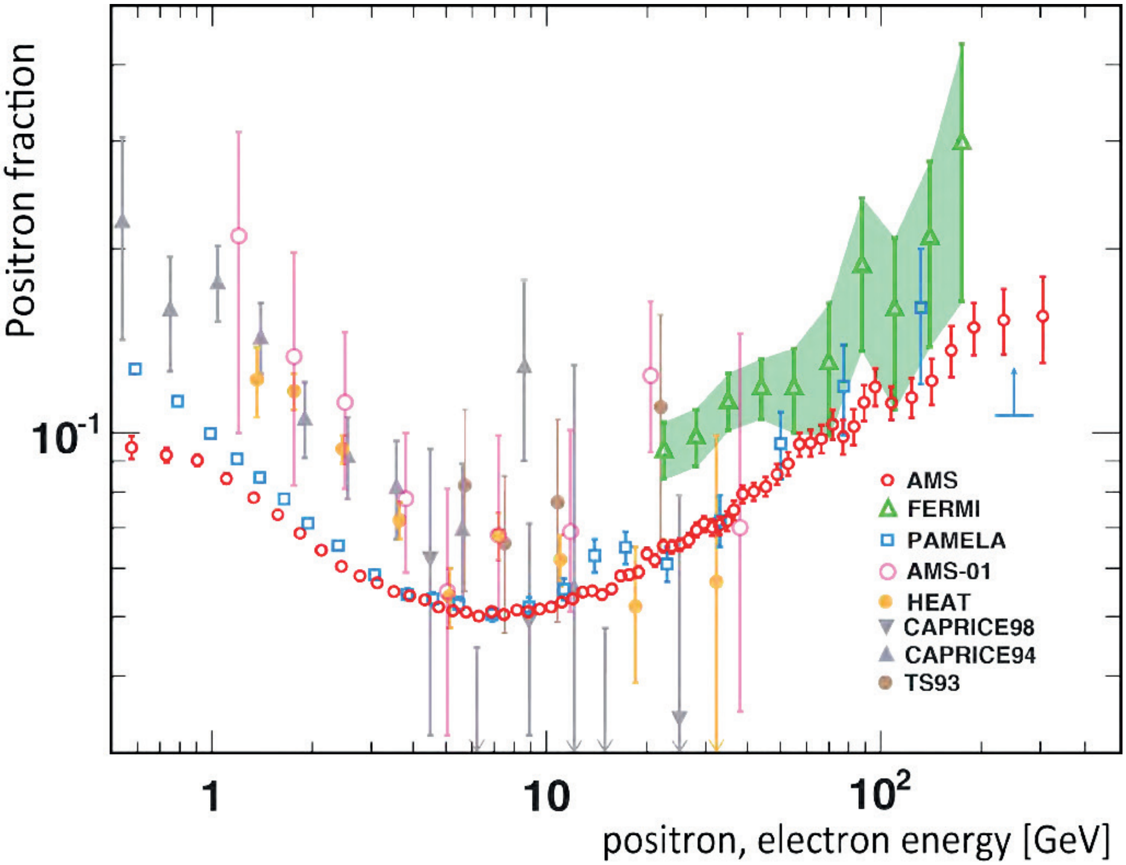

Figure 1-5: From a 2013 press release [AMS, 2013], a comparison of early AMS-02 results with published measurements of earlier experiments. The positron fraction is the ratio of the positron flux to the total combine flux of positrons and negatrons. Measurements shown range from 500 MeV to 250 GeV. PICAP is directed at positrons measurements well below this energy regime (few MeV).

The positrons measurements described in this section have primarily been made in space. Galactic cosmic rays have also been measured on balloon-borne experiments over shorter periods of time, compared to a space instrument, and at higher energies (≥ 1 GeV) [Daugherty et al., 1975]. During such experiments, positrons have been measured simultaneously with cosmic ray electrons at high energies. Moderate energy electrons in the inner Heliosphere are primarily Jovian (i.e. originating from Jupiter's magnetosphere), however, cosmic ray electrons with energies of a few MeV have possibly been measured in the outer Heliosphere [Lopate, 1991], where models have suggested non-Jovian electrons to dominate by as much 4 to 1 [Ferreira et al., 2001]. Cosmic ray positrons must exist at similar energies and could be measured with a PICAP instrument taken into deep space.

1.4 Purpose And Goals

The purpose of this work is to determine the viability of PICAP as an instrument concept and detector scheme for the measurement of moderate energy positrons in space. Historically, these positrons have seldom been observed, as there has been a lack of instruments dedicated to measuring them. Studying these positrons have implications on the study of GCRs and SPEs, which requires sending an instrument into deep-space beyond Earth's magnetosphere. A viable PICAP instrument must be capable of detecting and measuring positrons in space at a suitable rate, while rejecting a background of more abundant particle species, mainly protons. Such an instrument must also adhere to design constraints required for deep-space instruments, minimizing mass, power consumption, and complexity, while still being capable of meeting the scientific goals.

At the start of the project, a baseline design and preliminary modeling results had previously been reported [Connell et al., 2008]. Modeling efforts were continued with Monte-Carlo software to refine the design and determine the expected electron and positron response of a baseline instrument. The response is quantified as a "detection efficiency" or probability that a particle is identified, based on particular criteria. This model provided the basis of the design of a ground-based laboratory prototype.

The process of the prototype design and assembly introduced inevitable deviations and complexity from the idealized baseline design. These changes and their implications are detailed. Once fully assembled, the prototype instrument was connected to an arrangement of laboratory electronics to determine suitable operating parameters, verify functionality, and collect data for each detector. With initial laboratory testing and calibration of the detectors, we introduced basic methods for interpreting the readout of the detector data, required for analysis of testing at particle accelerator facilties.

After undergoing initial laboratory testing and calibration, the prototype instrument was exposed to proton beams with energies up to 215 MeV at the Francis H. Burr Proton Therapy Center at Massachusetts General Hospital on 1 June 2013. While PICAP is designed to identify positrons and electrons, it must be able to do so in the presence of a significant proton background. The test would demonstrate PICAP's ability to reject protons from identification.

The final testing for the prototype instrument involved exposure to electrons and positrons at the Idaho Accelerator Center at Idaho State University on 9–10 December of 2013. The purpose of this accelerator test was to determine the electron and positron response of the prototype instrument, with the intention of validating the baseline expectation set by Monte-Carlo modeling. To the best of our knowledge, this was the only facility in the United States that could provide both electrons and positrons in our moderate energy interval ($\sim$few to 10 MeV). Experimental challenges arose with the accelerator in terms of beam temporal structure and background. This prevented the accurate measurement of positrons in an event-by-event manner, as PICAP was designed to do.

The circumstances related to these challenges are discussed, including a statistical analysis developed to interpret the data from this particular experiment. When applied to the Monte-Carlo simulation data, the results of the statistical analysis agree qualitatively and quantitatively, effectively validating the modeling process.

This dissertation concludes with a discussion of PICAP's expected performance in space, as related to the science goals that were previously mentioned. We also consider the advancement of the NASA Technical Readiness Level (TRL) of PICAP, which is an assessment of a technology's maturity towards being proven for space-flight missions, beyond proof-of-concept (Level 3). There is a discussion of potential future work with the PICAP design and how simple alterations in the design can affect instrument performance, in regards to raising the TRL.

Chapter 2

Underlying Radiation and Detector Physics

2.1 Overview

Positron Identification by Coincident Annihilation Photons (PICAP) is a detector scheme designed for measurements of both negatrons and positrons, using a combination of particle identification techniques. The first technique is referred to as dE/dx vs. E'. dE/dx refers to the average energy loss, or linear stopping power, of a charged particle as it passes through matter. The incident particle deposits energy as it penetrates a "stack" of detectors and then loses the rest of its residual energy, stopping in some target, at some depth in the stack. The relationship between the energies the particle deposits penetrating the detectors and the energy it deposits in the stopping detector is unique to its charge, mass, and incident kinetic energy. The second technique involved in PICAP is the coincident detection of two 0.511-MeV γ-ray photons, indicating the annihilation, and therefore, detection, of a stopping positron.

Radiation detection occurs as a result of excitation from energy deposited in some detector material. The ways in which energy is transferred or lost from radiation to a detector depends on the source, which may be particle or electromagnetic, and the absorbing matter. The nature of how a detector converts this energy into a signal that can be measured depends on the type of detector. This chapter discusses energy deposition in matter due to energy loss of charged particles and absorption of gamma-ray (γ-ray) photons, how solid-state detectors and scintillation detectors work to measure the energy deposition, and the types of energy loss distributions expected, as they are relevant to PICAP.

2.2 Energy Loss of Protons In Matter; The Bethe-Bloch Formula

Charged particles passing through matter mainly undergo inelastic collisions with atomic negatrons of the material, as well as elastic scattering from atomic nuclei of the material. As a result, particles will lose energy and deviate from their incident trajectory. The inelastic collisions are largely responsible for energy loss of the incident particle [Leo, 1994]. Elastic scattering from nuclei does not occur as frequently, since the cross-section is smaller. If the nuclei are more massive than the incident particle, an elastic collision yields little energy transfer.

Atomic collisions result in small fractional losses of a particle's energy, but they occur so frequently over the course of passage through dense material that the total energy loss from this process may be significant, especially if the material is sufficiently thick. Such collisions also happen frequently enough that the large-scale energy loss does not vary beyond normal statistical fluctuations [Leo, 1994]. The result of many collisions in a material can be quantified by an average energy loss per unit path length, or dE/dx (also known as linear stopping power).

While PICAP was designed to identify and measure energetic electrons (and more specifically, positrons), to do so effectively requires that it is capable of discriminating protons from negatrons and positrons. There are no methods of directly determining charge built into PICAP. As protons and positrons have identical charge, their principal difference is mass. Because protons are nearly 2000 times more massive than electrons, their interactions with atomic negatrons and nuclei in matter must be treated differently.

Due to their greater mass, we assume that heavy charged particles (i.e. particles that are more massive than electrons, including protons and muons) lose energy with little deviation in their path. Only a small fraction of the particles undergo hard scatters. As previously mentioned, elastic collisions with nuclei result in little energy transfer, and any scattering of the incident particle is usually limited to small angles. Overall, heavy charged particles traverse matter, maintaining an approximately straight-line trajectory, while losing energy almost exclusively to atomic negatrons.

In 1915, Niels Bohr derived an energy loss formula for a heavy charged particle in matter [Jackson, 1999]. The calculation considered the approach of the incident particle towards atomic negatrons, which are assumed to be free and initially at rest. The incident particle exerts a Coulomb force on each atomic negatron it encounters. Energy is gained by the atomic negatron and lost by the incident particle in each collision. Because the mass of a heavy charged particle is much greater than that of a negatron , Bohr assumed that all incident particles do not deviate from their initial trajectories.

Although Bohr's formula was sufficient for estimating the energy loss of considerably slower alpha particles and heavy nuclei, it overestimated the energy loss of fast alpha particles, muons, and, most importantly, protons, because it ignored quantum effects [Jackson, 1999]. In 1930, Hans Bethe correctly derived the following formula:

$$-\frac{dE}{dx} = 2\pi r_{\mathrm{e}}^2 m_{\mathrm{e}} c^2 \left(N_{\mathrm{a}} \frac{Z}{A} \right) \frac{z^2}{\beta^2} \left[\ln \left(\frac{2 m_{\mathrm{e}} c^2 \gamma^2 \beta^2 W_{\mathrm{max}}}{I^2} \right) - 2\beta^2 \right] \tag{2.1}$$

Equation 2.1 is commonly referred to as the Bethe-Bloch formula [Leo, 1994]. The negative sign indicates energy loss, so that dE/dx is positive quantity by convention. z is the charge of the incident particle and $\beta = v/c$ is its velocity relative to the speed of light. γ is the Lorentz factor, where $\gamma = 1/\sqrt{1-\beta^2}$. $m_{\mathrm{e}}c^2$ is the negatron rest energy, 0.511 MeV, and r_{e} is the classical negatron radius, $\frac{e^2}{m_{\mathrm{e}}c^2} = 2.817 \times 10^{-13}$ cm. The quantity $N_{\mathrm{a}}\frac{Z}{A}$ is related to the number density of negatrons in the absorbing material, where N_{a} is Avogadro's number, and Z and A are the atomic number and mass number of the absorbing material, respectively.

The quantity I is known as the mean excitation potential of the absorbing matter. Theoretically, it is the product of the reduced Planck's constant and the average orbital frequency $\hbar\langle\omega\rangle$, weighted by quantum mechanical oscillator strengths of the atomic levels [Leo, 1994; Jackson, 1999]. Due to the large number of electronic excitation states and the complicated probabilities to transfer to these states, purely theoretical calculation of I is extremely difficult and prone to large uncertainty. Instead, semi-empirical formulas describing the relationship between I and Z were fitted to measurements of dE/dx for different materials. The relationship between I and Z is irregular for different ranges of Z, so it would be ideal to refer to a table of mean excitation potentials, rather than rely on a formula [Leo, 1994].

The Bethe-Bloch formula may be further simplified for incident heavy ions. W_{max} is the maximum energy that can transferred in a single collision, given by

$$W_{\mathrm{max}} = \frac{2m_{\mathrm{e}}c^2\gamma^2\beta^2}{1 + 2\frac{m_{\mathrm{e}}}{M}\sqrt{1+\gamma^2\beta^2} + \frac{m_{\mathrm{e}}}{M}} \tag{2.2}$$

If we take $M \gg m_{\mathrm{e}}$, then $W_{\mathrm{max}} \simeq 2m_{\mathrm{e}}c^2\gamma^2\beta^2$. Additionally, we can evaluate the coefficient:

$$2\pi r_{\mathrm{e}}^2 m_{\mathrm{e}}c^2 \left(N_{\mathrm{a}}\frac{Z}{A}\right) = \left(0.1535\ \frac{\mathrm{MeV}}{\mathrm{g/cm^2}}\right)\left(\frac{Z}{A}\right) \tag{2.3}$$

Combining this coefficient with the simplification of W_{max} gives us the following Bethe-Bloch formula for heavy charged particles:

$$\begin{aligned} -\frac{dE}{dx} &= \left(0.1535\ \frac{\mathrm{MeV}}{\mathrm{g/cm^2}}\right)\left(\frac{2Z}{A}\right)\frac{z^2}{\beta^2}\left[\ln\left(\frac{2m_{\mathrm{e}}c^2}{I}\frac{\beta^2}{(1-\beta^2)}\right) - \beta^2\right] && (2.4)\\ &= z^2\left(\frac{Z}{A}\right)f(\beta, I) && (2.5)\end{aligned}$$

All the constants have been folded into a function of the particle velocity and mean excitation potential of the absorbing medium, $f(\beta, I)$. Note that the units of dE/dx are typically in $\frac{\mathrm{MeV}}{\mathrm{g/cm^2}}$

as expressed here, where x is the areal mass density, or "grammage," that the incident particle encounters in its path. This is equal to the product of the thickness and mass per unit volume (density) of the material. We have also largely omitted higher-order corrections to the Bethe-Bloch formula, known as the density and shell corrections [Leo, 1994], which adjust dE/dx for incident particles at higher and lower velocities, respectively.

If we assume that $Z/A \approx 1/2$ and that I varies little for similar Z, then the energy loss largely depends on the charge and velocity of the incident heavy particle. Furthermore, if we take $z = 1$ for protons (and singly charged heavy particles), we see how dE/dx depends on the kinetic energy of protons. Generally, energy loss decreases with increased velocity, proportional to $1/\beta^2$. The energy dependence reaches a minimum when the proton becomes sufficiently relativisitic (corresponding to "minimum ionizing"). As the incident particle energy (thus velocity) increases even more, becoming extremely relativistic, dE/dx slowly increases (known as the relativistic rise) [Leo, 1994] (e.g. Figure 2-1). This minimum is reached when $\gamma\beta \approx 3$ or $v \approx 0.95c$ [Jackson, 1999]. Protons with energies exceeding 2000 MeV reach minimum ionizing and exhibit effects of the relativistic rise; however, as will be shown later in this work, protons with energies one order of magnitude lower in energy penetrate an entire PICAP detector stack. These and higher energy protons would, therefore, be rejected from positron identification, through the use of PICAP's anticoincidence system as will be described later.

As an incident particle loses energy, its velocity decreases which, as a result, increases the rate of energy loss per unit path length. While its detectors do not measure dE/dx directly, but rather the average energy deposition of the penetrating particle, PICAP was designed for a certain range of electron energies. Protons are notably slower (due to their greater mass) and lose energy more rapidly than electrons with comparable energies. If a detector is sufficiently thin, such that dE/dx can be taken as approximately constant, the energy loss rate can be estimated with the energy deposition, mass density, and thickness of the detector.

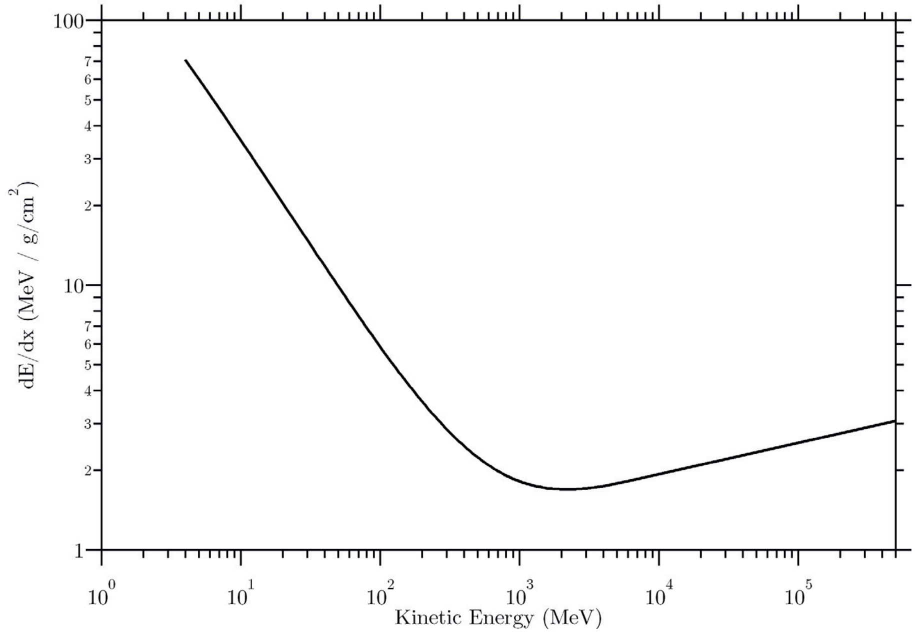

Figure 2-1: Generated plot of dE/dx as a function of the relativistic kinectic energy for protons in silicon, based on Equation 2.4 (note that some higher-order corrections have been omitted for simplicity). Protons reach minimum ionizing at around 2000 MeV, where dE/dx gradually increases with increasing velocity. This is the "relativistic rise."

2.3 Energy Loss of Negatrons and Positrons in Matter

Negatrons and positrons must be treated differently since they are prone to both energy loss and scattering from collisions with atomic negatrons and nuclei. They will tend to change direction randomly in the absorbing matter.

The Bethe-Bloch formula also applies to collisional energy loss of electrons with changes based on two aspects, when compared to the heavy particle case. Electrons are significantly less massive and the assumption that incident particles travel undeflected is no longer valid. In addition to being less massive, incident electrons are also identical in mass to atomic negatrons; therefore, they are indistinguishable and energy is distributed equally among the colliding particles [Leo, 1994].

$$-\frac{dE}{dx} = 2\pi r_{\mathrm{e}}^2 m_{\mathrm{e}} c^2 \left(N_{\mathrm{a}} \frac{Z}{A}\right) \frac{1}{\beta^2} \left[\ln \frac{\tau^2(\tau+2)}{2(I/m_{\mathrm{e}}c^2)^2} + F(\tau) + \ldots\right] \tag{2.6}$$

Note that the coefficient of the formula is identical to that of the formula for proton energy loss.

Correctional terms have been omitted. τ is $T_\mathrm{e}/m_\mathrm{e}c^2$, the kinetic energy of the incident particle in units of $m_\mathrm{e}c^2$. The function $F(t)$ is different for negatrons and positrons and is given, respectively, by:

$$F(t) = \quad 1-\beta^2+\frac{\frac{\tau^2}{8}-(2\tau+1)\ln 2}{(\tau+1)^2} \qquad \text{(for negatrons)} \tag{2.7}$$

$$F(t) = \quad 2\ln 2-\frac{\beta^2}{12}\left(23+\frac{14}{\tau+2}+\frac{10}{(\tau+2)^2}+\frac{4}{(\tau+2)^3}\right) \qquad \text{(for positrons)} \tag{2.8}$$

There are two different formulae because negatrons and positrons are oppositely charged. A derivation of Formula 2.6 is beyond the scope of this work; however, it is an example of the increased complexity that arises when negatrons and positrons are considered.

In addition to collisional energy loss, negatrons and positrons may lose significant energy via bremsstrahlung, which is the emission of radiation from acceleration ("braking") of a particle by the electric field of a nucleus. This is strongly depend on the Z of the absorber material, which determines a critical energy above which energy loss is dominated by radiation instead of collisions [Leo, 1994].

2.4 Energy Loss Distribution

The Bethe-Bloch formula can be used to predict the mean energy loss by a charged particle passing through some thickness of material; however, the collisions and scattering that contribute to the overall energy loss are statistical processes, which are accompanied by fluctuations. Identical particles with identical energies will not deposit identical amounts of energy into matter but rather a distribution of energies about the mean energy loss (dE/dx). Particle detectors, such as those in PICAP, ultimately measure these energy loss distributions for different particle species over a range of incident energies. The nature of the distributions depend on the thickness of the absorber or detector.

In a thick absorber, the number of collisions is large. Assuming that any change in velocity due to collisions is small or negliglible, the energy loss distribution will be a Gaussian in the limit that there are an infinite number of collisions (according to the Central Limit Theorem) [Leo, 1994]. The peak of the distribution would be located approximately at the energy loss calculated with the proper dE/dx formula integrated over the thickness of the absorber. When a particle loses enough energy to slow down considerally or even stop, then this case must be treated separately, since the assumption of negligible changes in velocity becomes invalid.

In the case of thin absorbers, the number of collisions drastically decreases with the possibility that the energy loss in any single collision is significantly different than the assumed mean energy loss in the thick absorber case, making the distribution more difficult to calculate. The energy loss distribution is asymmetric about the peak with a high-energy tail (see Figure 2-2). This high-energy tail shifts the mean energy loss higher, while the peak of the distribution represents the "most probable energy loss." The upper limit of the distribution is the maximum amount of energy that can be transferred in any collision, "$\mathrm{W}_{\mathrm{max}}$" in Figure 2-2. While for protons, this is exclusively collisional, electrons also have the rare chance at losing large amounts of energy due to bremsstrahlung [Leo, 1994]. This is typical of energy deposition distributions for certain thin detectors of the PICAP.

A few theories attempt to predict the energy loss distributions in thin absorbers, each using the ratio between the mean total energy loss and the maximum energy transfer ($\kappa = \Delta/W_{\mathrm{max}}$) as a parameter. These include Landau's theory for very thin absorbers ($\kappa \leq 0.01$) and Symon's and Vavilov's theories for intermediate values of κ, which could be as high as around 10 (although the Gaussian limit is already being approached at $\kappa = 1$). Later in this work, using a modified Gaussian approximation of the most probable energy loss was deemed sufficient for determining the energy distribution of different PICAP detectors.

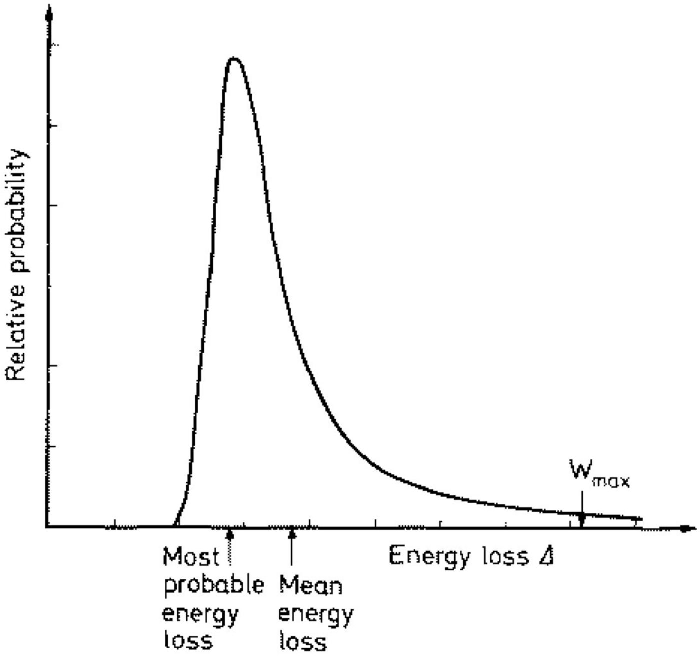

Figure 2-2: A typical asymmetric energy loss (expressed as Δ here) distribution in a thin absorber [Leo, 1994]. The peak represents the most probable energy loss, while the high-energy tail skews the mean energy loss to be greater than the most probable energy loss. This is typical of the type of distribution resulting from PICAP's thin detectors.

2.5 Negatron-Positron Annihilation

As the name of the detector scheme states, PICAP's main purpose is to identify positrons by detecting annihilation photons coincidentally. Positrons that stop in an absorbing material will annihilate with ambient negatrons of that material to produce two photons, each with energy equal to the rest mass of an electron, 0.511 MeV, by conservation of mass and energy. Momentum conservation requires the photons produced be emitted in opposite directions.

$$\mathrm{e}^- + \mathrm{e}^+ \rightarrow \gamma + \gamma$$

In certain cases where the relative velocities between a negatron and positron is small, such as in positronium, electron-positron annihilation results in the emission of three γ-ray photons; however, the cross-section of for three-photon annihilation was found to be 370 times smaller than the cross-section for two-photon annihilation [Ore and Powell, 1949]. In the context of PICAP this case is ignored.

2.6 Photon Absorption

PICAP's effectiveness depends on its ability to detect 0.511-MeV γ-ray photons; however, photons are electrically neutral, so they do not undergo the same type of collisional energy loss that protons and electrons do. The three most common processes that occur to photons traversing matter are the photoelectric effect, Compton scattering, and pair production [Leo, 1994].

The photoelectric effect occurs when the absorption of a photon results in the ejection of a negatron from an atom, known as a photoelectron. For the absorption of γ-rays, the cross-section for the photoelectric effect goes as Z^4 or Z^5 [Leo, 1994]. Rather than being absorbed, Compton scattering of photons by atomic negatrons may also happen. A photon, such as a γ-ray, emerges with decreased energy, which is transferred to the atomic negatron causing it to recoil. The scattering cross-section is proportional to Z. Finally, passage of photons in matter can result in pair production, which is the conversion of a photon, for example, into a negatron and positron pair, usually in the presence of a nucleus. This requires that the incident photon has an energy of at least 1.022 MeV (twice the mass of m_{e} [Leo, 1994]). The total pair production cross-section goes approximately as Z^2; however, this process is negligable in PICAP as 0.511-MeV γ-rays resulting from negatron-positron annihilation are too low in energy to pair produce.

If there were a beam of photons passing through a layer of matter, it does not suffer a decrease in energy but rather an attenuation in intensity. Photons are removed by absorption via the photoelectric effect and pair production or scattering by the Compton effect. The attenuation of the intensity of such a beam due to all of these processes is:

$$\frac{I}{I_0} = \exp\left(-\mu x\right) \tag{2.9}$$

$\mu = \sigma N$ is the total absorption coefficient of the material, which depends on the number density of atoms N and the total cross-section per atom of photon interaction σ. The ratio, I/I_0, can be considered as the probability that a photon passes through matter of thickness x.

γ-rays that pass through matter and do not interact go undetected. They are more penetrative in matter than charged particles, because cross-sections of photon interaction processes are significantly smaller compared to cross-sections for inelastic electron collisions [Leo, 1994]. The overall cross-section σ is the sum of the cross-sections for the photoelectric effect, Compton scattering, and pair production, each with varied increasing dependance on Z. An ideal γ-ray detector is made of a high-density, high-Z material.

With an understanding of how radiation imparts energy in matter, we will briefly discuss how different types of PICAP detectors measure this energy.

2.7 Solid-State Detectors

In a crystalline solid, the arrangement of atoms or molecules in a periodic lattice causes the overlapping of atomic negatron wavefunctions, leading to the formation of numerous discrete but closely spaced outer energy levels. The energy levels are closely spaced enough, such that they can considered as continua of energy bands. Electronic energy band structure features a highest energy band, known as the conduction band, where negatrons freely move, and a lower energy band, known as the valence band, where negatrons are bound to the lattice atom or molecule. A forbidden energy gap (or band gap) devoid of allowed energy levels may separate the two bands, whose size depends on lattice spacing and determines key properties of the material [Leo, 1994].

Insulators have a large energy gap, such that thermal energy is not sufficient to free negatrons from the valence band to the conduction band. Conductors have overlapping valence and conduction bands without an energy gap separating them, allowing for excited negatrons to easily move freely in the conduction band. Semiconductors fall in between and have energy gaps that are small enough for a few negatrons to be freed from the valence band to the conduction band by thermal energy [Leo, 1994].

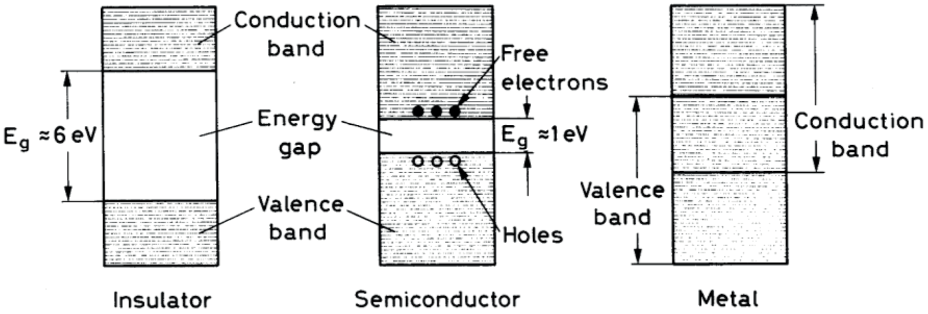

Figure 2-3: An illustration [Leo, 1994] demonstrating the difference between the energy band structures of insulators, semiconductors, and conductors. The semiconductor's narrower forbidden energy gap allows for the creation of negatron-hole pairs when a valence negatron is excited into the conduction band by thermal energy.

When a valence negatron is excited into the conduction band, it vacates a "hole," a virual particle of positive charge. The hole can be filled by a nearby valence negatron, effectively "moving" the hole, while negatrons are free to move in the conduction band; therefore, negatrons and holes are the charge carriers for any current formed. The presence of impurities, in the form of recombination and trapping centers, create additional levels within forbidden energy gaps that can be occupied by once free negatrons and hinder charge collection [Leo, 1994].

Solid-state detectors (SSDs, also known as semiconductor detectors) are widely constructed with doped semiconductors, in which small concentrations of impurity atoms are strategically introduced to form energy levels in the forbidden gap very close to either the valence or conduction bands. Semiconductors with impurity atoms introduced to create an excess of negatrons are known as "n-type." Conversely, those in which impurity atoms are introduced to create an excess of holes are known as "p-type" [Leo, 1994]. When a p-type and n-type semiconductor are juxtaposed, creating a p-n junction, excess holes and negatrons diffuse across the boundary, causing a separation of charge, and diffusion halts due to the electric field gradient created. The electric field gradient creates a region of potential difference across the junction where their are no mobile charge carriers, known as the depletion zone. A diode is a classic example of using a p-n junction.

Charged particles passing through a depletion zone of an SSD deposit energy and create pairs of negatrons and holes that are swept from the depletion zone by the electric field, resulting in a current, or charge pulse, which is collected with electrical leads. By itself, the depletion zone is narrow and has a low particle detection efficiency and significant noise in the signal [Leo, 1994]. The operation of an SSD requires a reversed bias to be applied that increases the width of the depletion zone, which increases the effective volume for particle detection. An SSD can be considered as a sort of reversed-biased diode.

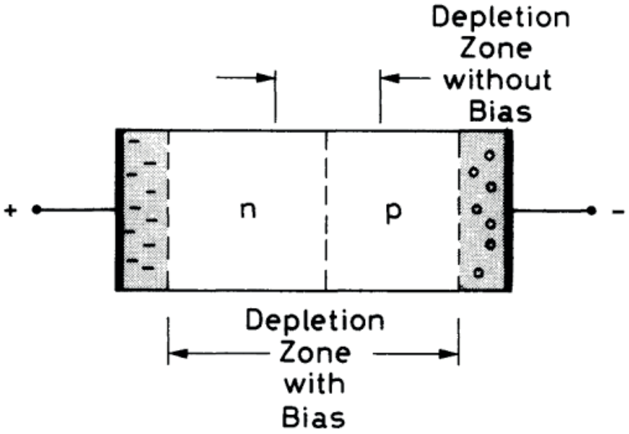

Figure 2-4: An illustration [Leo, 1994] of the depletion zone of a p-n junction. The introduction of a reverse bias voltage widens the depletion zone, increasing the effective volume for radiation detection. In fully depleted SSDs, the depletion zone can be extended to nearly the entire thickness of the detector.

Notable semiconductor materials used for SSDs are silicon and germanium; however, for charged particle detection, such as in PICAP, silicon is most widely used. We know thermal energy can create negatron-hole pairs, which can then be swept from the depletion zone and contribute to detector noise. Germanium must be cooled, while silicon can be used at room temperature and is less susceptible to noise [Leo, 1994]. Silicon also has a lower atomic number ($Z = 14$ vs. $Z = 32$ for germanium) and density, making it less sensitive to photons. Conversely, germanium detectors are preferred for γ-ray detection. The main disadvantages of silicon detectors, as compared to germanium, are that they are sensitive to visible light and more sensitive to surface contaminants, which could be present in the environment or deposited by contact.

The specific types of silicon detector used in PICAP are known as a surface barrier detectors, which are unique in that depletion zones are formed from the junction of either n-type or p-type silicon with a thin layer of metal to serve as the p-type or n-type side, respectively, creating a thin barrier that acts like a p-n junction. These are known as Schottky barriers, which are simpler to manufacture than standard p-n junctions [Leo, 1994]. Thin surface barrier detectors can be biased so that the depletion zone extends to nearly the entire thickness of the detector, making them especially useful for measuring the dE/dx of penetrating particles (Section 2.2). The output signal of an SSD is an electric current due to negatron-hole pairs leaving the depletion zone. All but one of the SSDs in PICAP are fully depleted, to be detailed later in this work.

2.8 Scintillation Detectors

From their introduction into nuclear physics in the early 1900s, scintillation detectors were praised for their ability to detect radiation, including energetic particles, when compared to their gas ionization chamber counterparts in terms of reliability and convenience. Scintillation detectors are fast, in that they recover quickly to their initial states between excitations. Depending on the scintillator material, different types of particles (such as electrons versus protons) can be identified by analyzing the temporal shape of the light pulse [Leo, 1994].

Scintillation detectors yield a signal, via flashes of light (or *scintillation*), whose intensity, to first order, increases linearly with the amount of energy absorbed [Leo, 1994]. Scintillation photons are transmitted to light detectors, such as a photomultiplier tube (PMT), via a light guide and/or photosensitive surface in contact with the detector, and converted to a measurable current. Out of necessity, scintillation detectors must be nearly transparent to the particular frequencies of light they emit. Scintillation could be in the form of fluorescence, phosphorescence, or a combination of both. Two classes of scintillation detectors are used for PICAP: inorganic crystals and organic plastics.

Inorganic scintillators are comprised primarily of ionic crystals, most commonly of alkali metals and halogens, known as alkali halides. Examples include, sodium iodide (NaI) and cesium iodide (CsI). Similar to semiconductor materials, the crystal lattice structure of inorganic scintillators have an electronic band structure. Interactions between ions in the lattice perturb and broaden the energy levels into the valence and conduction bands, separated by forbidden energy gaps. Scintillation occurs when negatrons transition between conduction and valence bands across the this gap [Leo, 1994].

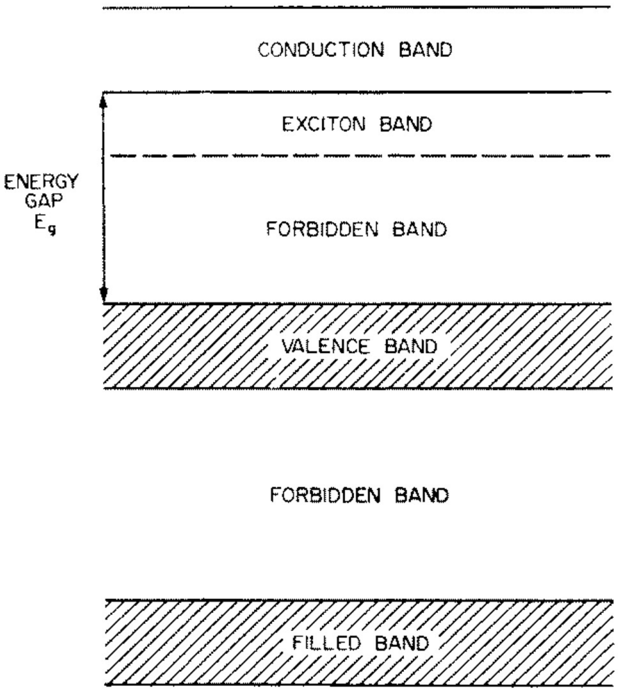

Figure 2-5: A diagram of the electronic band structure, resulting from the lattice structure of an inorganic crystal scintillator [Birks, 1964]. Note the existence of an exciton band below the conduction band, which accommodates bound negatron-hole pairs, known as excitons. Scintillation occurs when a free negatron from the conduction band falls to a free hole in the valence band or when a exciton pair recombines.

Excitation by radiation similarly creates pairs of free negatrons in the conduction band and free holes of positive charge allowed to “move” accordingly in the valence band. In contrast to a semiconductor, another scenario arises in that a negatron removed from the valence band may remain bound to its corresponding hole. The bound pair is known as an exciton, which moves together, with the negatron being in a band of lower energies in the conduction band, known as the exciton band (see Figure 2-5). In a pure crystal, emission of light occurs through the transition of the recombination of a free negatron with a free hole or an exciton pair; however, it is also common to introduce impurities to inorganic scintillators called activators.

The introduction of activator impurities to purposely create intermediate energy levels within the forbidden gap between the valence and conduction bands is not unlike the process of semiconductor doping for use in an SSD; however, rather than the creation of a depletion zone, free negatrons and exciton negatrons are encouraged to transition to the created energy levels and then transition to the ground state, resulting in fluorescence. The activator not only increases the crystal's ability to scintillate, but increases the wavelength of emitted light, corresponding to energies below the energy absorbed. This improves transparency (and reduces self- and re-absorption) of the emitted light through the scintillator and increases compatibility with a PMT that is optimized for a certain wavelength of light.

Inorganic crystals are denser and have higher Z than plastic scintillators. Because of their high-Z nuclei, electrons are susceptible to large-angle scattering and backscattering out of inorganic scintillators. The same high-Z nuclei and high density give inorganic scintillators a greater cross-section for γ-ray interaction (Section 2.6) and detection in PICAP.

Organic scintillators are comprised exclusively of hydrocarbon compounds, arranged in hydrocarbon chains, resulting in the formation of π molecular orbitals [Birks, 1964]. In an organic scintillator, the outermost valence negatrons of the molecule occupy these orbitals and are free to be excited to orbital states of higher energy, which could be a spin singlet or spin triplet state. Each energy is further divided into sub-levels due to molecular vibrations (shown in Figure 2-6).

A charged particle or photon interaction excites valence negatrons from the ground state, typically denoted as S_0, to an excited singlet state (S_1, S_2,..., etc.) from which it falls almost immediately to the first excited state S_1, if not there already; however, these transitions do not result in fluorescence (this is "internal degradation" in Figure 2-6). Fluorescence only occurs for transitions from S_1 to S_0 and any of its vibrational sub-levels. A disadvantage presents itself when from S_1, a small number of negatrons may transition from the singlet system of states to the first excited triplet state T_1 (there is no ground triplet state). Negatrons will tend to stay in this state longer than in S_1 and can either be elevated to higher triplet states or de-excited to the ground state via interactions with another molecule in the triplet state [Birks, 1964; Leo, 1994]. The result here is delayed emission of light, phosphorescence, which may add to the signal decay time of the scintillator. Phosphorescence, however, is primarily associated with either impurities or activator elements introduced to inorganic scintillators and is not prominent effect in organic materials.

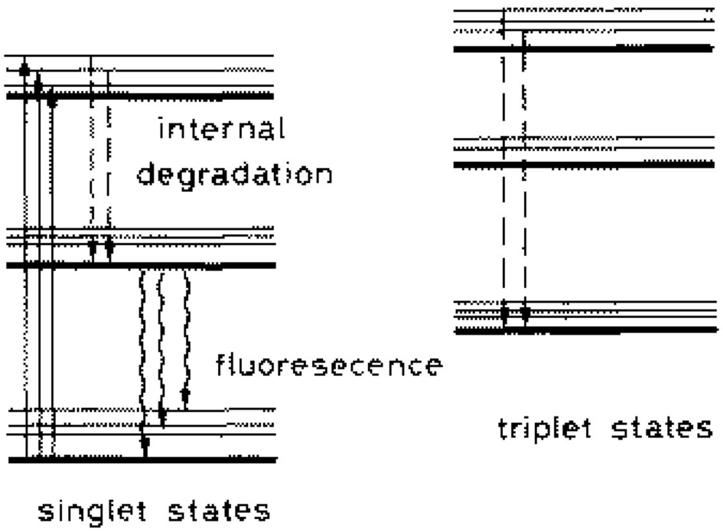

Figure 2-6: A diagram of negatron energy levels in an organic scintillator molecule [Leo, 1994], separated by spin singlet states and spin triplet states, oriented vertically (up is increasing energy). Emission of light only occurs when negatrons de-excite from the first excited singlet state S_1 to any one of the sub-levels of the ground state S_0.

Low-Z, low-density scintillators are less likely to scatter γ-rays, allowing them to escape the detector and are less likely to scatter electrons through large angles or backscatter them, making organic scintillators more suitable for detecting electrons. In organic scintillators, valence negatrons transition to the sub-levels of S_0 from S_1 emitting light with energy lower than that which is required to excite them from S_0 to S_1 [Leo, 1994]. This makes them transparent to their own emitted light.

Scintillation in an organic material depends only on the arrangement of the π molecular orbitals, from how the compounds are linked, rather than an electronic band structure as seen with semiconductor materials and inorganic scintillators. Because of this, they may take on any form, whether it be a pure crystal, a liquid, or a polymer plastic. Each form has its advantages and disadvantages. Pure organic crystals are durable, with anthracene having the highest light output of all organic scintillators; however, their performance is heavily dependent on their orientation with respect to the radiation source and they are difficult to machine [Leo, 1994]. An organic liquid is a solution of scintillator in a solvent. It takes on the shape of its container, and any energy is absorbed and quickly reemitted through the solvent. While other substances can be easily added to the liquid to adjust for a certain detection task, this reduces the emission of light and increases sensitivity to impurities, to which liquids scinitillators are particularly susceptible [Leo, 1994]. Additionally, it is generally inadvisable to use liquids in space application if at all possible.

The compromise between pure crystal and liquid is the organic plastic (polymer) scintillator. They are similar to liquids, except the solute is dissolved in a solid solvent. They can be machined or cast to any shape for any purpose, while still remaining durable, less prone to the effects of impurities, and relatively inexpensive [Leo, 1994]. They are the most frequently used type of organic scintillator and are featured on the PICAP prototype instrument. While different forms present different degrees of practicality, impurities could lead to significant decreases in light emission as well as inconsistencies in performance between otherwise chemically identical organic scintillators. The plastic option presents the least amount of risk in this regard. Certain impurities, called waveshifters, may also be introduced, which change the wavelength of emitted light to improve scintillator efficiency and prevent reabsorption of emitted light. Waveshifters act similarly to activator impurities introduced to inorganic crystal scintillators.

Chapter 3

From Model To Prototype

3.1 Overview

Charged particles undergo energy loss upon penetration and subsequent interaction with matter. Particle detection techniques exploit properties of certain materials to effectively convert this energy loss into a measurable signal. The Positron Identification by Coincident Annihilation Photons (PICAP) system was introduced as an instrument concept for detecting moderate energy (∼2–10 MeV) positrons [Connell et al., 2008]. A general history of observations of such positrons was presented in the first chapter (Section 1.3). A goal of this work is to show how PICAP applies established detector techniques and science in a straight-forward manner to detect positrons. PICAP is essentially a scheme of different types of detectors strategically oriented and configured for this purpose. A design for an instrument was devised based on this scheme. Different detector types, such as those that have been discussed, were considered and chosen based on their advantages and disadvantages. Experimentally demonstrating an instrument concept requires testing a real, working prototype. Other real-world complications, such as availability and feasibility of obtaining and machining different detector components as well as the monetary budget figured heavily into the design and assembly of the prototype.

Before the design was finalized, we established a baseline for the performance of a PICAP-type instrument. Our design was adapted to a computer-based model, which served as the primary geometry for simulations, using the EGS4 Monte Carlo code system [Nelson et al., 1985]. During these simulations, single charged particle (negatron and positron) events were repeatedly generated, based on several user-defined parameters, to obtain a large random sample of how the particles interact with the provided geometry (i.e. the energy loss in each component in the computer model we defined, based on the instrument design). The results of the simulations defined the baseline instrument response when exposed to negatrons and positrons. The prototype instrument was used to validate the simulations.

Modeling results from simulations were previously presented, when the a design concept was originally proposed in Connell et al. [2008]; however, known differences between the dimensions of detectors in this original model and the dimensions of detectors that we had planned to use in the prototype instrument prompted the updated design concept and the necessity for collecting new simulation data. This updated model reflected these differences (detailed later in this chapter) and included few other modifications, meant to optimize the instrument size and performance. The modeling results presented in this chapter, therefore, come from newly run simulations for the specific purposes of this work, as opposed to those previously done for the originally proposal. The updated model ultimately informed the design of the prototype instrument.

Most of the silicon solid-state detectors (SSDs) used in the prototype were readily available and concurrently tested while drawings for other parts of the prototype were being developed from our baseline design and finalized for parts procurement and machining by outside manufacturers. The build process also had to account for additional structural and electrical elements, necessitating iterative changes in the finalization of the as-built design. This chapter details the evolution of the PICAP system from a concept to a working prototype instrument. The prototype also underwent initial laboratory tests and detector calibration. Data analysis methods sufficient for the interpretation of PICAP data, as well as results of preliminary testing, are presented.

3.2 The Origin Of The PICAP Design

Science goals were motivated in the introductory chapter, accompanied by examples of previous positron measurements made with past spacecraft instruments, some of which were not originally designed for positron detection and mostly not aimed at the moderate energy regime of several MeV. PICAP is a concept for a deep-space instrument, and therefore, design constraints would follow those pertaining to spaceflight. This generally requires minimization of instrument mass, power usage, size, and telemetry and necessitates simplicity in instrument design. As this work is mainly a proof-of-concept project, we did not ultimately aim to produce a refined, flight-ready instrument; however, such constraints were considered in designing a ground-based prototype that functions as intended and could potentially be adapted to a flight-ready design.

The primary purpose of the PICAP system is to detect and identify positrons and electrons, among several other populations of particle species with varied energy spectra. We can generalize this as a population of negatrons, positrons, and protons. Charged particle species exhibit a unique relationship between their energy loss when traversing matter versus their total incident energy. We refer to charged particle identification using this relationship as dE/dx vs. E' technique, where the energy loss that a particle undergoes penetrating some system of detectors along its trajectory (dE/dx) is measured against the loss of its remaining (or residual) energy (E') when it comes to rest in another detector. Different types of charged particles at similar energies will lose different amounts of energy as dE/dx.

Considering one particle type at a time, PICAP must first be generally able to discriminate protons from electrons. At comparable energies, protons move significantly slower due to their greater mass. We recall (sections 2.2 and 2.3) how the dE/dx energy loss in matter increases with the magnitude of the incident particle's charge but decreases with its velocity. Protons, as well as heavier particles, would be rejected based on their significantly larger dE/dx energy deposition. In order to effectively exclude certain particles from consideration with this technique, the design requires at least two or more similar detectors capable of measuring energy loss by penetrating radiation. While one detector would be sufficient in measuring dE/dx, redundant measurements ensure the suppression and rejection of the predominant proton background in space. Silicon SSDs are suitable for this application and can be made very thin so that the energy loss during particle penetration (dE/dx) is small compared to the total incident energy. SSDs also have very good energy resolution (typically 10s of keV, compared to the few MeV of dE/dx energy losses). The active area of SSD disks effectively determines the aperture of the instrument design. This defines the instrument's central axis and the trajectory of particles for measurement and identification. This configuration of SSDs is similar to that of the APEX instrument [Ahmad et al., 1996], which is the original inspiration for PICAP, introduced in the first chapter (Figure 1-1). The initial SSD array makes up the top of a cylindrical detector "stack."

For positrons to be identified as positrons, they have to slow to a stop and annihilate with an ambient negatron in the stopping material. This process emits the two 0.511-MeV gamma (γ) ray photons that must also be detected. After penetrating the initial array of SSDs, particles slow down as they lose energy, depositing their residual energy in a larger detector that follows in this stack. The detector must be considerably thicker to stop particles of varying energies and sufficiently wide to accommodate particles whose trajectory spreads from the SSD stack. An organic plastic scintillation detector was chosen for the stopping region. In practice, plastic scintillators are simple to machine and have reasonable energy resolution (typically $\sim$100 keV as compared to the few MeV of residual energy loss), making them suitable for measuring the energy deposition of particles, whether residually after stopping or from passing through. Assuming protons have already been rejected from consideration by the thin silicon SSDs, negatrons and positrons in similar energy ranges will stop in this plastic scintillator. Most importantly, low-Z plastic scintillators are relatively transparent to 0.511-MeV photons, allowing pairs emitted via negatron-positron annihilation to be detected by surrounding γ-ray detectors.

If not already apparent, negatrons and positrons are expected to exhibit almost identical responses in the initial thin SSD array and stopping detector of the stack. There is no charge-sign dependence in dE/dx to first order. A small, second-order charge-sign dependence ($\lesssim$1%) is only expected when the particle velocity is low (i.e. comparable to the ambient negatrons in the material) [Barkas et al., 1963]. Negatrons and positrons that penetrate the SSDs and stop in the central plastic would be identified simply as "electrons," hence, the adoption of this naming convention from the beginning of this work to collectively describe both positrons and negatrons, $e^{\pm}$. This is conventional in this field of study.

In order to detect the two 0.511-MeV photons, the stopping region of the stack is surrounded by inorganic crystal scintillation detectors. Inorganic crystals are denser and have higher-Z nuclei, making them more capable of stopping and absorbing these γ-rays for detection. The use of multiple inorganic crystal scintillation detectors reflects the fact that the pair of annihilation photons are emitted in opposite directions. PICAP identifies positrons by simultaneously detecting *exactly* two 0.511-MeV signals, each one in a different detector; therefore; the design must feature at least two different crystal scintillators. The APEX detector stack is surrounded by 24 equal toroidal segments of NaI (sodium iodide) [Ahmad et al., 1996]. PICAP's γ ray detectors consists of four toroidal segments of crystal scintillator. Requiring two coincident 0.511-MeV signals suppresses false identification from the background or, for example, a scattered particle that may randomly produce a single 1.022-MeV signal.

Identification of particles via the dE/dx vs. E' technique is contigent on particles stopping in the plastic scintillator, after having penetrated the SSD array of the stack. To complete the design requires some sort of anticoincidence shield, which is a detector enclosing the stack to detect particles that are out of the geometry. If particles significantly scatter within the instrument, this implies deviation from expected path, and this shield would also identify these events. In the case that particles are energetic enough to penetrate the entire stack, another SSD is used at the bottom of the stack, acting as part of the anticoincidence shield. While another plastic scintillator could be used at the bottom of the stack, it would have to be significantly thicker than an SSD to be structurely sound and produce sufficient light, which adds unwanted bulk to the instrument.

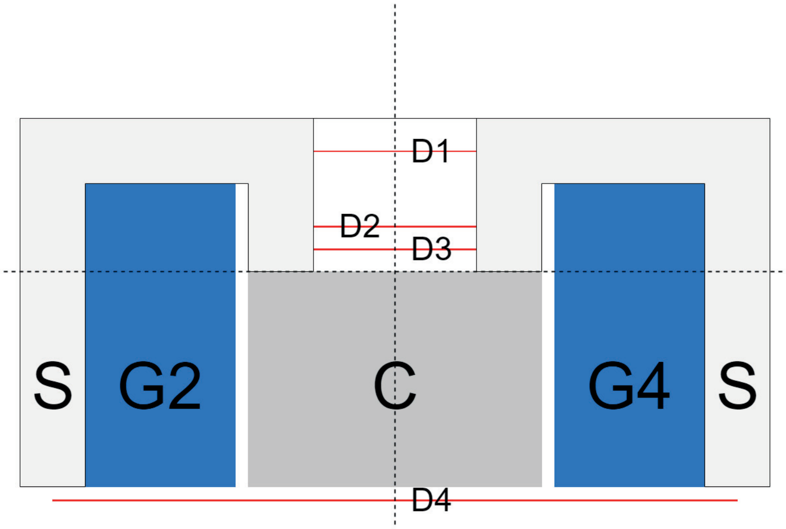

Figure 3-1: The original proposed design of a PICAP-type instrument [Connell et al., 2008] as a cylindrical cross-section. It features different detector types: D1–D3 are thin silicon SSDs, C is a central plastic scintillation detector, and G1–G4 (two of four of these detectors are visible from this view) are inorganic crystal scintillation detectors. D4 is an additional SSD and S is plastic scintillator. Together, D4 and S act as an anticoincidence shield.

This particle discrimination and identification process governs the types and physical configuration of detectors chosen for the design of the overall instrument. Similar techiniques have been historically used in electron measurements in this energy range, such as those discussed in the first chapter, and are typical methods which inform the PICAP system. The techniques were combined to devise a baseline model for the PICAP system [Connell et al., 2008], shown in Figure 3-1. Each detector or group of detectors serve a uniquely specific role. This original baseline design was then modified and refined and eventually adapted to a complete design of the prototype instrument.

3.3 Theoretical Baseline Model

The initial design considerations discussed in the previous section explain how different detectors or group of detectors provide particle identification, specifically proton discrimination and positron identification. A baseline design for the PICAP detector scheme was devised using these techniques, and we want to determine the expected performance of an instrument of this design. This was achieved with Monte Carlo computer modeling, simulating the idealized response to energetic negatrons and positrons of each detector in the geometric layout.

The original dimensions and elements of the PICAP design concept (Figure 3-2) were initially proposed in the oft cited earlier work by Connell et al. [2008]. Detector thicknesses and dimensions were chosen for the energy range of particles for which PICAP is intended, ∼2–10 MeV, at a certain effective area, or *geometrical factor*. Early EGS4 simulation results were presented based on this geometry. For this work, an updated version of the design was adopted based on knowledge of some of the detectors that we had planned to use in the prototype instrument prior to its assembly. Alterations to the original model were meant to optimize the instrument size and performance. The newer "detector stack" is shown in Figure 3-2 (left).

At the top of the stack are a series of SSDs for dE/dx measurements. In the PICAP system, this consists of three silicon SSDs, which we denoted D1, D2 and D3. All three detectors are disks with an active radius of 1.25 cm. D1 is the thinnest, with a thickness of 50 μm, while D2 and D3 both have a thickness of 1000 μm. The SSDs allow for particles of interest to penetrate, depositing a well-resolved dE/dx signal unique to the mass, energy, and trajectory of the particle, allowing for identification. Multiple SSDs make the dE/dx measurement redundant (over D1, D2, and D3) aiding in the identification of particles, especially in rejecting the more abundant proton background. As shown later in this work in Chapter 5, measurements required over multiple SSDs were also useful in rejecting events where multiple particles might be simultaneously penetrating the stack.

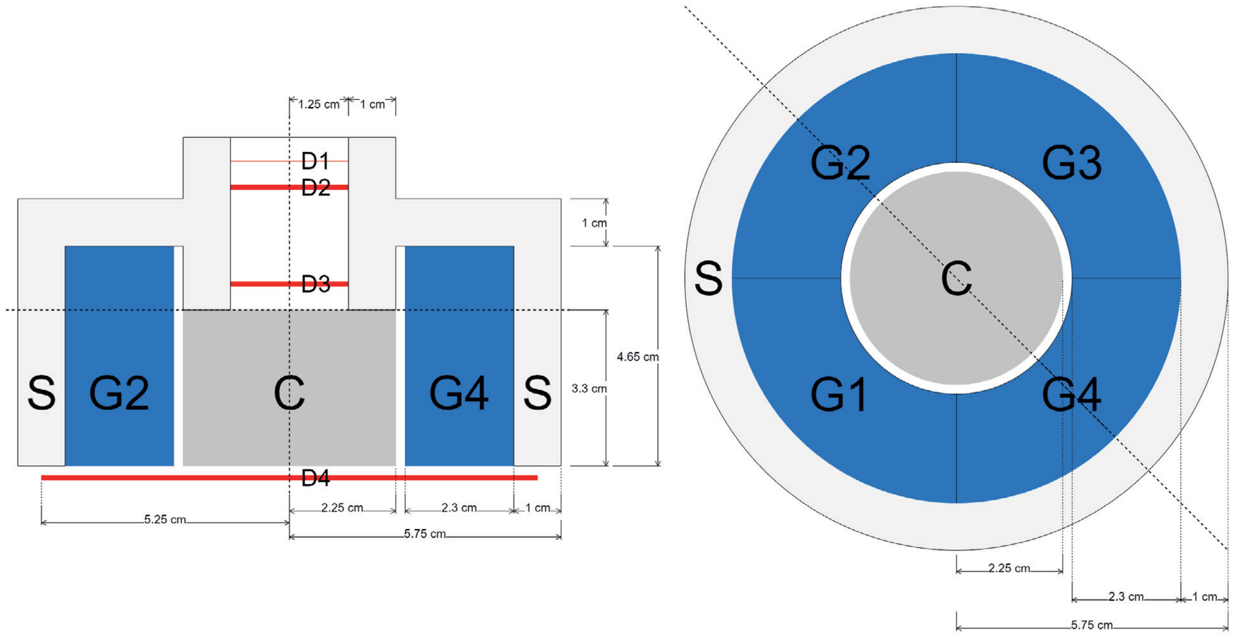

Figure 3-2: Model of the PICAP detector scheme, modified from the original design concept (Figure 3-1), used as the basis of the geometry for new Monte Carlo/EGS4 simulations. The dotted lines in each point of view represents where the cross-sections were taken relative to each figure. D1–D4 (red) were defined as Si. G1–G4 are four toroidal segments of CsI. The plastic center detector C (gray) and the surrounding anti-coincidence shield S (white) were define as nylon.

Following the first three Si detectors is a cylindrical plastic scintillation detector, denoted C (for "center" or "central"), where particles of interest will stop and deposit their residual energy, after having penetrated and deposited energy in D1, D2, and D3. The height/thickness of C defines the range, or stopping distance, of incident particles. Adjusting the height of C thus changes the maximum stopping energy. Particles of energies below the energy range of interest will not reach the C detector, and therefore, not satisfy the minimum energy requirement for identification. Particles of energies above the effective energy range will completely penetrate the C detector. Here, C is a cylinder with a radius of 2.25 cm and height of 3.3 cm; the density of the plastic is $\sim$1 g cm^{-3}. Note that C could be made taller to increase the efficiency of electron detection and increase the energy reach of particles accepted; however, introducing a larger C would increase the dimensions and mass, a consideration for an eventual flight instrument design. The prototype design is intended to demonstrate the smallest telescope capable of meeting the science goals. If additional resources are available, a more capable version is easily implemented.

Detection of the annihilation photons originating from the C plastic scintillation detector is accomplished using denser, higher Z, inorganic crystal scintillators. Surrounding C in the design are four equally segmented toroidal CsI (cesium iodide) detectors, denoted G1 through G4. Each piece has a thickness of 2.3 cm (where the inner radius is 2.5 cm and outer radius is 4.8 cm; refer to the top-down cross-section in Figure 3-2) and height of 4.65 cm. A requirement unique to positron identification is detection of 0.511-MeV γ-ray annihilation photons in two (and exactly two) of the four segments. Four crystal scintillation detectors was deemed to be sufficient, compared to the 24 toroidal detectors present in the much larger APEX instrument. This was based on a trade-off between photon directionality and complexity of design and required power usage in space instrumentation.

Lastly, the stack is enclosed by an anticoincidence shield to reject particles that do not enter the 1.25-cm aperture at the top of the instrument. The "shield," which we denoted as S, is an irregularly shaped plastic scintillation detector (of material similar to C), surrounding the main detector elements. The shield also detects particles (e.g. electrons) that drastically scatter outward from within the stack. To account for particles that do not stop in C (or those that enter the stack in the reverse direction), a fourth SSD, called D4, is located at the bottom of the stack. D4 is also 1000 μm thick but has a radius of 5.25 cm in the design. D4 effectively works as part of the anticoincidence shield S, with lower mass than the scintillator.

We acknowledged that this design and the dimensions of its elements varied slightly from the original design proposed in Connell et al. [2008] (Figure 3-1), most notably the thicknesses, positioning, and separation of D1–D3 (Table 3.1) and the overall form of the anticoincidence shield S. The radii of the detectors remained the same.

The SSD thicknesses were chosen based on the1000-μm detectors that we were planning to use for the prototype instrument. Introducing thicker SSDs should only increase the minimum energy

	Thickness (μm)		Position Above C Detector (cm)	
PICAP Design	Original Model	Updated Model	Original Model	Updated Model
aperture	10	10	2.35	3.65
D1	50	50	1.85	3.15
D2	200	1000	0.70	2.65
D3	200	1000	0.35	0.50

Table 3.1: Differences in SSD thickness and vertical position of each SSD (relative to the top of the C scintillation detector) between the original PICAP model and the updated baseline model.

required for electrons to penetrate the SSD stack and reach the C detector by approximately 0.5 MeV [Berger et al., 2017]. 1000-μm detectors are still thin enough for dE/dx measurements of moderate-energy negatrons and positrons. On average, electrons in this energy range would only lose $\lesssim$1 MeV penetrating D1–D3.

The spacing between D2 and D3 was increased, where D2 is located closer to D1, having previously been placed closer to D3. The was done to ensure coincidence in geometry. By placing D2 and D3 apart from each other, we confirm the trajectory for particles of interest as passing through the center of the detector stack. The increased spacing and vertical position of D1–D3 above the C detector should only affect the effective area or geometrical factor of the instrument, which is the proportionality relating the particle counting rate to the intensity of radiation being measured, assuming the distribution of radiation is isotropic [Sullivan, 1971]. For a cylindrically symmetric particle instrument with two circular detectors with radii R_1 and R_2 separated by l, the geometrical factor is

$$G = \frac{\pi^2}{2}\left[R_1^2 + R_2^2 + l^2 - \left\{(R_1^2 + R_2^2 + l^2)^2 - 4R_1^2R_2^2\right\}^{\frac{1}{2}}\right] \tag{3.1}$$

The geometrical factor of the original PICAP design is 2.88 cm^2 sr, defined by the radius of the central aperture of the instrument and the distance between the opening and the C detector. The increased separation between the opening and the C detector reduces the geometrical factor by almost a factor of 2 (1.95 cm^2 sr); however, this only affects the particle rate of the instrument, limited geometrically by the anticoincidence. When PICAP's performance and response is evaluated, we were only concerned with particles within the geometry established by the detector stack.

The model is a idealized representation of how a PICAP-type instrument and its detectors would be configured. Before proceeding to developing an actual prototype for testing, we modeled the PICAP's response to energetic negatrons and positrons with computer simulations. The results of the simulations provide us with a general expectation of the response of the PICAP detector scheme, absent of complications introduced in real-world prototype.

3.4 Simulating Instrument Electron Response

Prior to designing and building a prototype, a computer model version of the PICAP detector scheme outlined in the previous section was modeled using Monte Carlo simulations based on the EGS4 (Electron Gamma Shower) code system. EGS4 simulates negatron, positron, and γ-ray trajectories, interactions, and energy losses in a geometry set by user-defined parameters.

All of the input parameters for an EGS4 simulation are defined in a "control deck." The simulation geometry (Figure 3-2) was based on the design of the PICAP detector scheme model. The cylindrical symmetry of the design was exploited and each region, including both detector elements as well as empty space, is defined in the control deck by an inner/outer radius and upper/lower height with respect to the central axis of the stack. This is straightforward, since most of the detectors are cylindrical or toroidal, with the exception of the irregularly shaped anticoincidence shield. S, also cylindrically symmetric though irregular, was defined by specifying the coordinates of the vertices of the detector's cross-section and rotating it 360°.

Also defined for each simulation run's control deck are the total number of particles, the particles' charge (-1 for negatrons, 1 for positrons), energy in MeV, and incident trajectory and source. Each run effectively simulates the exposure of the instrument to a monoenergetic beam of normal incidence with respect to the top of the detector stack. The radius of the beam was set to be one cm, which is slightly smaller than the aperture of the design. This was repeated for negatrons and positrons of energies ranging from 0.5 to 16 MeV in 0.5-MeV increments. The results of the simulations are a cumulative set of trials each with 3×10^6 particles, where each trial is a simulation at one particle energy. The output for each trial is a data set containing the energy deposition by each particle event in each defined region of the simulation geometry (i.e. each detector of the instrument). Each simulation trial can be summarized with a set of histograms showing energy loss distributions in each detector (e.g. Figure 3-3).

In general, only particles that stop in the central plastic scintillation detector C are considered for analysis. This requires that the signal in D4 is zero. A non-zero signal in D4 likely indicates that a particle had sufficient energy to completely penetrate C and would be automatically excluded. Particle discrimination requires dE/dx measurements from penetration of the initial series of SSDs in the detector stack, so those that scatter into the anticoincidence shield S are assumed to have siginificantly deviated from the intended trajectory and are also excluded. Data were collected on an event-by-event basis identified on an event-by-event basis. We quantitatively determined the baseline performance of the PICAP model under exposure of negatrons and positrons by counting the number of events that satisfying a specific set of particle identification criteria.

Identification criteria refers to the set of conditions that must be met by each detector for particle events to be properly identified. We may refer to this colloquially as "taking cuts" on the data, based on the distributions/spectra of energy loss (such as those in Figure 3-3). The percentage of particle events originating from the simulation beam that satisfy a set of identification criteria is referred to as a detection efficiency. We may think of detection efficiency as a probability (or expectation value) of identifying a certain type of particle. The purpose of running these simulations was to establish general baselines of PICAP's response to electrons, and the detection efficiency is a metric representing said baseline.

We know that the particles in the simulations are either negatrons or positrons, so we were

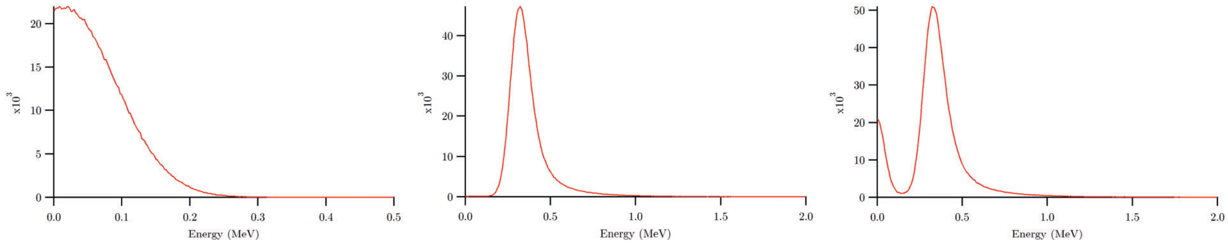

(a) D1 (b) D2 (c) D3

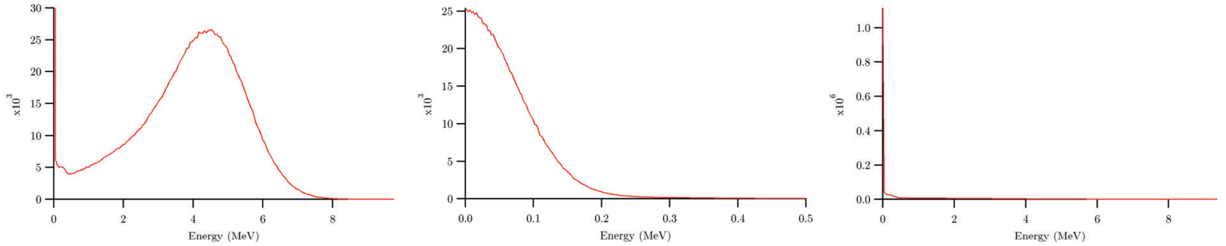

(d) C (e) D4 (f) S

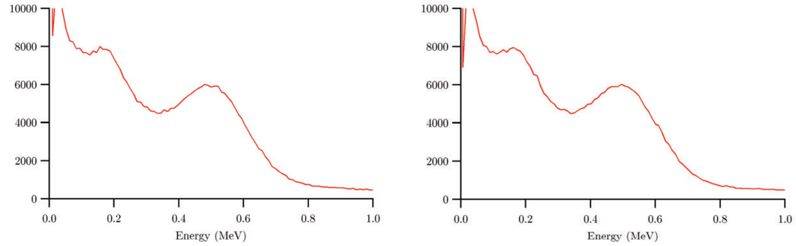

(g) G1 (h) G2

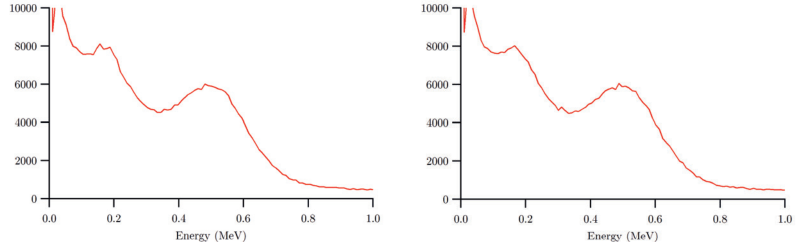

(i) G3 (j) G4

Figure 3-3: Sample of energy loss distributions in each detector for 5.5-MeV positrons (from EGS4 simulations) with Gaussian noise added to simulate detector noise and energy resolution. Energy loss is in MeV.

interested in the detection efficiency of positrons as electrons, negatrons as electrons, positrons as positrons, and negatrons as positrons. Note that of these four outcomes, only negatrons as positrons is a misidentification, expected to be zero, but needed to be modeled. The only condition that distinguishes a positron event from a negatron are the annihilation photons, so there is no method for uniquely identifying a negatron. Sets of minimal conditions were established to produce these four identification outcomes.

To be identified, both negatrons and positrons have to penetrate D1, D2, and D3, and stop in C. If ΔE is the energy loss measured in a detector, then this condition could be represented as such:

$$\Delta E(\text{D2, D3, C}) > \Delta E_{\text{min}} \; ; \; \Delta E(\text{D2, D3}) < T_p$$

At the baseline level, ΔE_{min} is 0, but in practice, this would be some minimum threshold signal that must be exceeded for it to be measured, due to detector noise and pedestal effects. Gaussian noise was introduced to the simulation data to emulate detector noise and add broadening effects.

T_p is some lower threshold for proton energy deposit in D2 and D3. Ideally, this threshold would be set at slightly below the minimum ionization energy deposit of a proton (which occurs for protons at ~2000 MeV), so as to always reject protons from identification as either electrons or positrons. In practice, more elaborate schemes for rejecting protons are often adopted, because of their ease of implementation in space instruments, but all rely on the fact that slower moving protons deposit more energy through ionization energy loss than electrons do at similar total energies. Negatrons and positrons with enough energy to completely penetrate C trigger a non-zero signal in D4 and are excluded. Particles that scatter into the anticoincidence shield S are also excluded from consideration: $\Delta E(\text{D4, S}) < \Delta E_{\text{min}}$ (0, in the simplest case).

Positron identification additionally requires detecting the two photons produced from negatron-positron annihilation. We represent this condition:

$$0.511 - \delta < \Delta E(\mathrm{G}_{i,j}) < 0.511 + \delta \ ; \ \Delta E(\mathrm{G}_m, \mathrm{G}_n) = \Delta E_{\mathrm{min}}$$

$\mathrm{G}_{i,j}$ represents one of six unique possible pairs of G crystal scintillation detectors in which two 0.511-MeV signals can be measured, while G_m, G_n represent the other two G detectors. The condition here is that a 0.511-MeV signal is measured in exactly two G detectors. Note that the annihilation photons in the simulations do not deposit exactly 0.511 MeV in each detector, due to energy resolution of the scintillator, so the criteria requires a signal within an energy threshold, ranging from $0.511 - \delta$ to $0.511 + \delta$ MeV. To remain consistent with the original paper [Connell et al., 2008], $\delta = 0.025$ MeV, and the condition is satisfied if the signal is in the range of 0.486–0.536 MeV. While higher values of δ may increase the positron detection efficiency, it also increases the probability of false positron identification.

There are no criteria that uniquely distinguish a negatron from a positron, but we know that they should register zero signal in G1–G4, due to the lack of annihilation radiation:

$$\Delta E(\mathrm{G1},\ \mathrm{G2},\ \mathrm{G3},\ \mathrm{G4}) = \Delta E_{\mathrm{min}}$$

Particles that scatter into G1–G4 would also be rejected accordingly. This condition is required of negatrons, but not unique to them, as it also applies to positron events, whose annihilation photons did not produce signals in G1–G4 (either by missing the G's or not interacting). By our nomenclature, a particle identified as a positron also qualifies as an electron. For a particle to be identified as an electron, it may satisfy either the annihilation photon condition or positrons *or* the condition there is no signal in any G detector (indicating that the particle was negatron or even a positron whose annihilation photons were not detected).

The electron and positron identification criteria were then applied to all sets of simulation data.

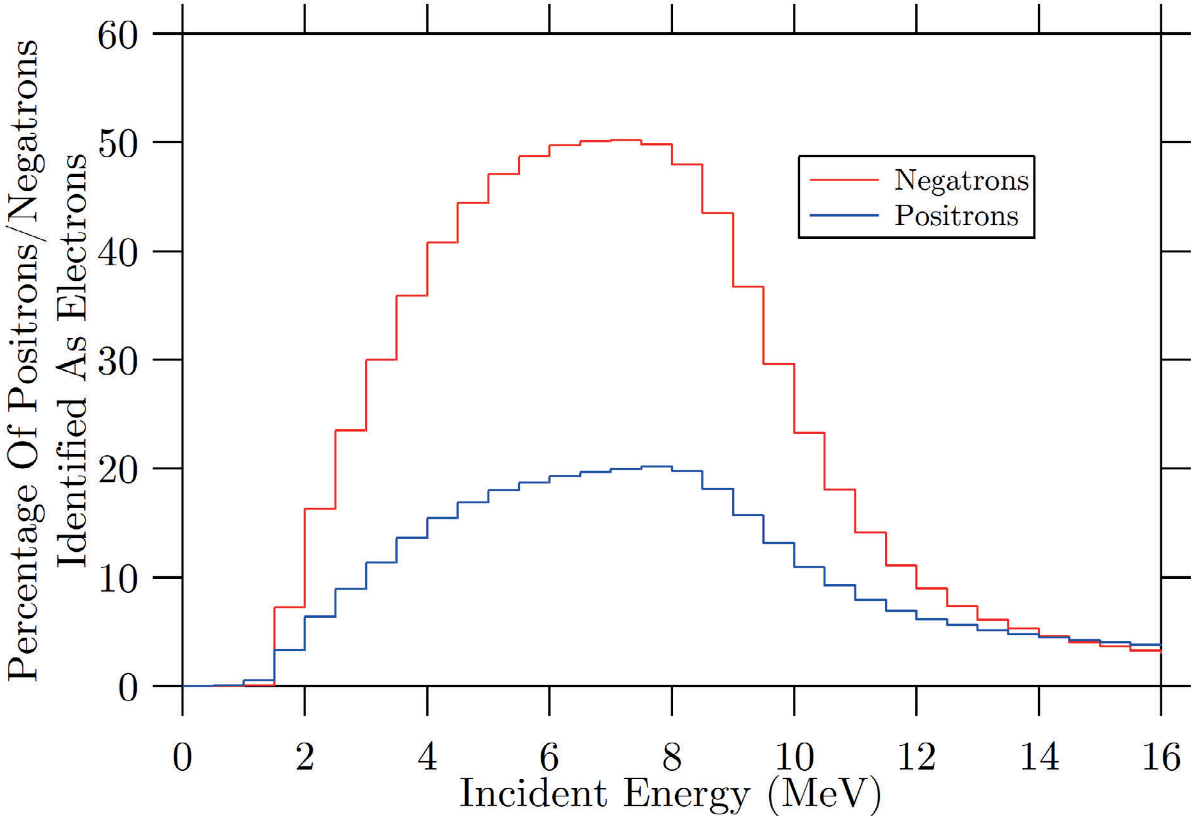

Figure 3-4: Baseline electron (i.e. negatron and postiron) detection efficiency of PICAP model for both negatrons and positrons generated from EGS4 Monte Carlo simulations.

A particle event that meets the identification criteria count towards one instance of detection. The detection efficiency is then just the sum of detections divided by the total number of particles produced by the simulation beam. The electron and positron detection efficiencies are then plotted as a function of incident energy for each particle species.

Regarding negatrons and positrons being identified as electrons, Figure 3-4 reveals a relatively flat response, specifically for particles with energies ranging from ∼4–9 MeV. The electron detection effiency peaks at approximately 50%. The steep decreases in detection effiency outside of this range are due to particles that did not reach the C detector or those that penetrate the entire stack, which begins to occur more frequently at 8.5 MeV for both negatrons and positrons. Above 14 MeV, the efficiencies for negatrons and positrons become similar, because they penetrate the stack with the same probability. The electron detection efficiency for positrons is significantly lower within the

~4–9 MeV range, only reaching a maximum of around 20%. This is expected because positrons identified as electrons include those whose annihilation photons have failed to interact with the G detectors. Along with criteria for positron detection, another condition of electron detection is zero signal in G1–G4. Therefore, if the one of two annihiliation photons interact with the G detectors, then that particle is also disqualified as an electron.

By contrast, the positron detection response (Figure 3-5) is not as flat. The positron detection efficiency increases and peaks at ~1.2% for 5.5–6 MeV positrons and then rapidly decreases at higher energies. The coincident annihilation photon detection requirement proves to be rather stringent; however, very few negatron events are misidentified as positrons. If negatrons are unlikely to be misidentified as positrons, then it is much more unlikely for protons to be masquerade as positrons. This is especially pertinent, because in space, protons at ~MeV energies outnumber negatrons by a factor of ~10, and negatrons outnumber positrons by a factor of ~10. Because proton energy loss relations are well known and their trajectories are relatively straight, proton Monte Carlo simulations were not explored. This was simply not a priority, given the time and budgetary limitations. However, proton response was revisited and directly tested in the first of two principal accelerator experiments for the PICAP laboratory prototype, which demonstrated the real-world rejection of protons (Chapter 4).

The simulation results provide a baseline for the expected response of a PICAP-type instrument, because they are based on an idealized version of the detector stack. A physical, laboratory prototype was designed and assembled for the purpose of real-world testing of the PICAP system. In transitioning from an abstract design to a prototype, additional components required for biasing and signal processing from detectors and maintaining structural support were introduced, increasing the overall complexity of the instrument. The prototype is not expected to perform as ideally as a computer model of the instrument, but the goal is validating the simulation results.

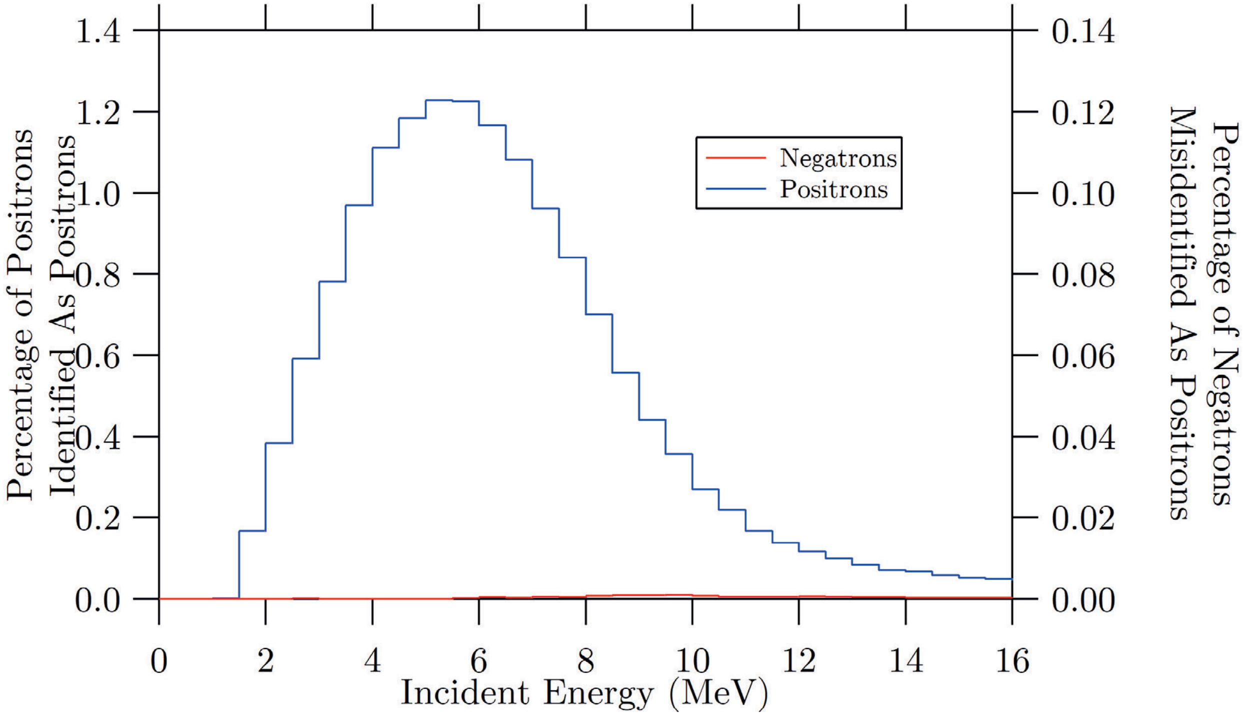

Figure 3-5: Baseline positron detection efficiency of PICAP model of positrons generated from EGS4 Monte Carlo simulations. The fraction of negatrons that were misidentified as positrons is plotted against the right axis. The scale of the right axis is intentionally ten times shorter than the scale of the left axis to the demonstrate the relative positron detection efficiencies when there are ten times as negatrons as positrons.

3.5 Measuring Instrinsic Noise of Solid-State Detector (SSD)

The silicon SSDs used in the PICAP prototype instrument for D1, D2, and D3 are fully-depleted surface barrier detectors repurposed from a previous experiment. There were multiple candidates for D1–D3. We verified functionality of each detector by determining the amount of intrinsic noise in each detector and decided on the ones best suited for the PICAP prototype based on the results. Each SSD has a certain amount of instrinsic noise, which is always present when the detector is biased. This noise level effectively sets the minimum energy deposition that must be exceeded for a signal to be measured. The noise was determined from measuring the width (standard deviation) of the residual energy loss distribution of stopping alpha particles. We tested 50-μm thick (for D1) and 1000-μm thick detectors (for D2 and D3) and chose the detectors with the lowest noise for the

PICAP prototype.

Detectors are calibrated by recording spectra with peaks (from particle energy loss) of known energy. The spectra collected are in the form of histograms binned in electronic channels. The known radiation energy allows us to assign values of energy to each channel number from which we can determine the amount of noise in MeV. For this initial SSD calibration, the candidate detectors are exposed to alpha particles from a radioactive source americium-241 (^{241}Am). The energy loss by alpha particles stopping in the detectors generates an energy loss distribution. A fitting function was applied to the distribution from which the position of its peak and width was determined.

Each SSD was tested in a small vacuum chamber, since alpha particles lose significant energy in air. Detectors were placed on a custom-made aluminum mount (Figure 3-6). An ^{241}Am source, with a gold window, was attached to an aluminum plate and slid into place on the same mount, with the window facing opposite the center of the detector. An additional plate with a small opening was placed between the source and detector to collimate a beam of alpha particles. The vacuum chamber contained fittings with pass-through connectors to apply bias voltages and carry the detector output to external electronics.

Before each calibration run, the chamber was allowed to stabilize at its minimum pressure. Bias voltages were then applied based on guidelines provided by the manufacturer (35 V for 50-μm SSDs and 100 V for 1000-μm SSDs). Liveness was verified with an oscilloscope. The detector output was then connected to a 13-bit (8192-channel) digital multichannel analyzer. We must note that this experimental arrangement was only used to measure the noise in each SSD; the testing of the prototype instrument differs almost entirely. When testing this prototype as a whole, there was no vacuum chamber, and there was a completely different set of electronics, as detailed below.

The SSD response to α-particles was treated as a Gaussian of the following form:

$$f(\Delta E) \propto \exp\left(-\frac{\left(\Delta E - \overline{\Delta E}\right)^2}{2\sigma^2}\right) \tag{3.2}$$

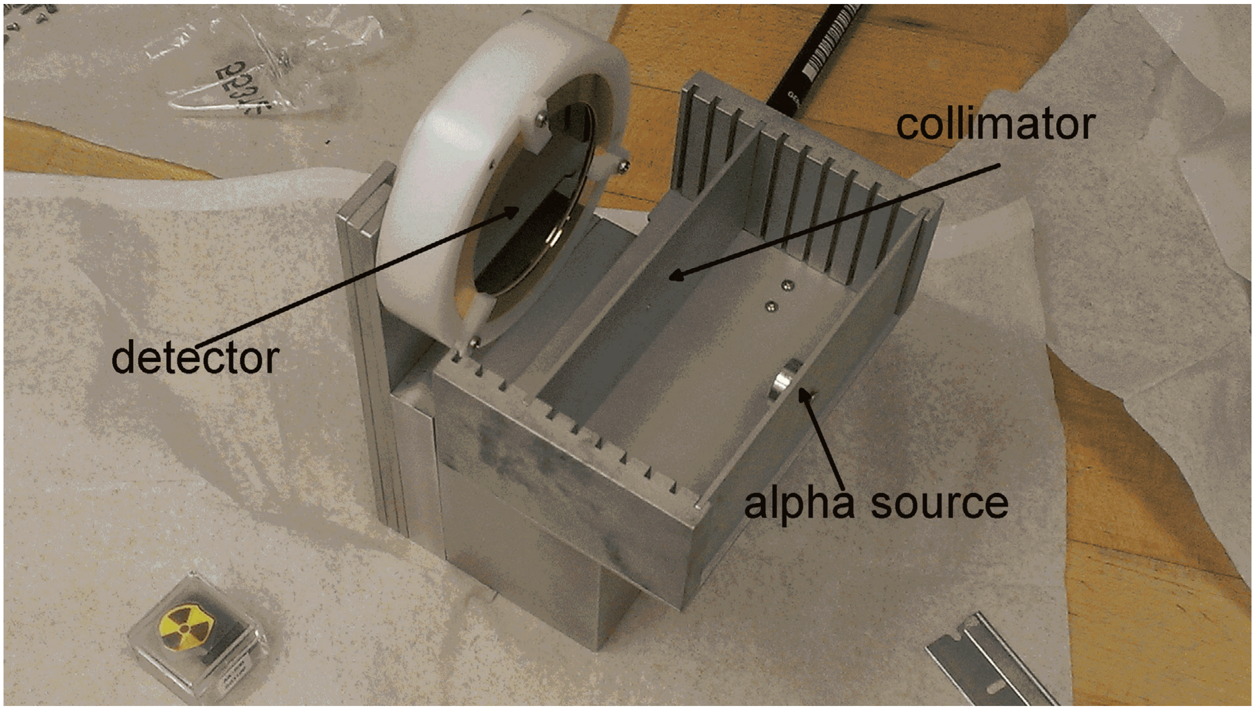

Figure 3-6: The mount for SSD calibration. A candidate for D4 attached to one end of the mount (left), and the ^{241}Am source is attached to a plate held at the other end of the mount. This mount is placed in a vacuum chamber.

The average energy loss $\overline{\Delta E}$ is the energy loss at the peak of the distribution and σ is the characteristic width (standard deviation) of the distribution about the peak, representing the total noise in the signal. Fitting the energy histograms with standard Gaussians (Figure 3-7) produces these two best-fit parameters. The conversion from channel number to energy, referred to as the conversion gain, is just the ratio of the channel number of the peak of the histogram to the known energy loss, shifted to account for pedestal (electronic offset). With the conversion gain, the σ of the distribution can be converted to an energy.

When ^{241}Am undergoes alpha decay, it emits an alpha particle with an energy of $\sim$5.4 MeV. It was previously mentioned that the radioactive source had a gold window. The window reduces the energy of emitted alpha particles to 4.454 MeV ± 0.0806 MeV. The conversion gain is calculated from dividing 4.454 MeV by the channel number of the peak of the histogram. The total noise of the peak is then the product of σ and the conversion gain. The window introduces spectral broadening

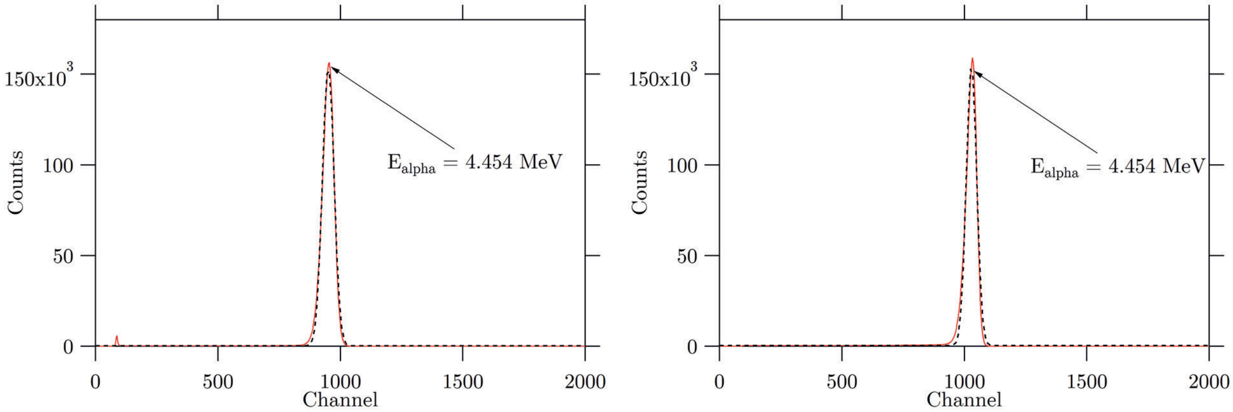

(a) D1 (b) D2

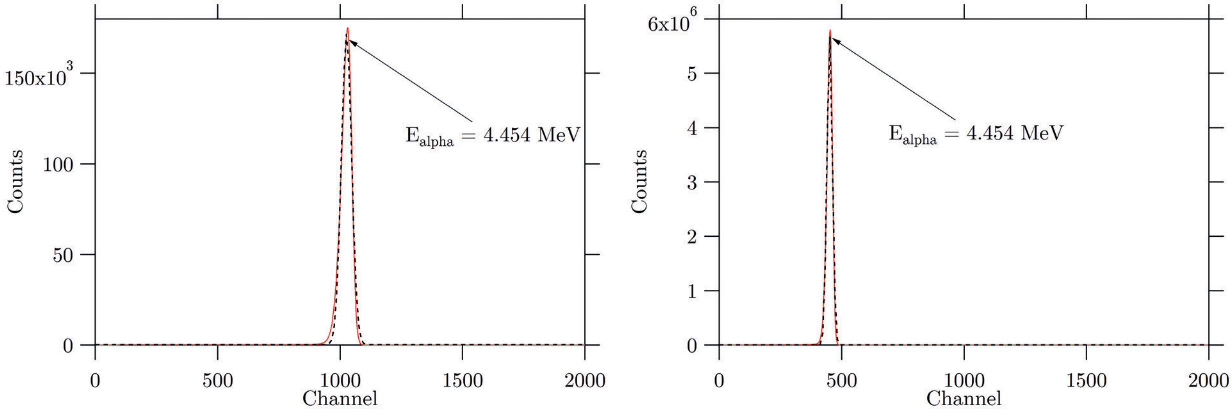

(c) D3 (d) D4

Figure 3-7: Spectra for SSDs (D1–D4) from a ^{241}Am α-emitter. Each spectral peak is fitted with a Gaussian (dotted line) to measure the intrinsic detector noise (which is the σ of the Gaussian).

that must be substracted quadratically from the total noise to obtain the detector noise:

$$\sigma^2_{\text{SSD}} = \sigma^2_{\text{total}} - \sigma^2_{\text{window}} \tag{3.3}$$

The noise in 50-μm detectors were consistently ~75 keV and the noise in 1000-μm detectors was ~45 keV. A measurable signal then ideally exceeds this noise "plateau" (σ) by a factor of two or three σ. For D2 and D3, we expect to resolve signals if they exceed ~100 keV. D1 is expected to be able to resolve signals of at least ~200 keV. We could refer to these as the minimum threshold energies that "trigger" the detectors.

The SSD for D4 was the only SSD that was procured specifically for this project. D4 is the detector at the bottom of the stack. While it is also 1000 μm thick, it was only partially depleted, so it effectively acted as a thinner SSD. When looking at their noise, silicon SSDs function like parallel-plate capacitors, so the capacitive noise increases as the thickness of the SSD decreases and the surface area of the SSD increases. As expected, the noise measured in this detector was also ~75 keV, similar to that of 50-μm detectors.

From these initial calibrations, we were also able to select the detectors to be used in the PICAP prototype. The SSD testing process occurred concurrently with the design and eventual assembly of the prototype instrument, which will be described in the next section.

The advantage of using computer simulations to determine the baseline performance of the theoretical model is complete knowledge of the particle type and charge. For PICAP to be a viable instrument concept, it must be capable of rejecting protons from positron identification. A proton will lose more energy in D1, D2, and D3 than a positron of the same energy, due to its higher mass and lower speed; therefore, upper limits can be placed on identification criteria for these detectors, using these noise measurements.

We know from the previous chapter, during the discussion of energy loss distributions in thin absorbers, the peak of the distribution represents the most probable energy loss. Considering only electrons of both charge that stopped in C, the most probable energy loss in D1, D2, and D3 was calculated from each simulation trial. According to the EGS4 simulation data, electrons in the energy interval of interest (∼2–10 MeV) typically lose 14 keV in D1 and 290 keV in D2 and D3. In other words, they would be expected to lose at least 600 keV of energy to the SSDs before eventually stopping in C. This sets the lower limit of the PICAP's effective energy range.

D1 acts as a trigger for rejecting protons. Electrons at these energies do not lose enough energy to exceed the noise of the detector, so any signal above two or three times the noise is rejected. The noise is 75 keV and any signal above 225 keV would be automatically rejected for identification. For D2 and D3, the identification criteria for electrons can be restricted to a certain range of energies. The lower limit would be two or three times above the noise, around 135 keV. We also want to impose an upper limit to the electron identification criteria for D2 and D3, to further discriminate protons from postirons. This is discussed as part of preparation of results in the next chapter.

3.6 The Prototype Instrument

In the previous sections, the PICAP detector scheme was proposed, from which a theoretical model was devised. The response of the model to energetic electrons was then simulated with EGS4 Monte Carlo simulations, with the results providing a baseline for the performance of the detector scheme. The work up to this point largely informed the next steps of designing a PICAP prototype instrument based on the model, assembling it, and testing it for functionality.

Extensive work with the creation of the prototype was done by University of New Hampshire mechanical engineering student Brendan Bickford. Under our scientific guidance, supervision and physical assistance, Bickford created design drawings, ordered and machined parts, assembled the instrument, and performed various structural analyses. Bickford's work was the basis of his senior engineering design project and detailed in his thesis [Bickford, 2012]. The design for the prototype was primarily based on the theoretical model, whose performance was established with EGS4 Monte

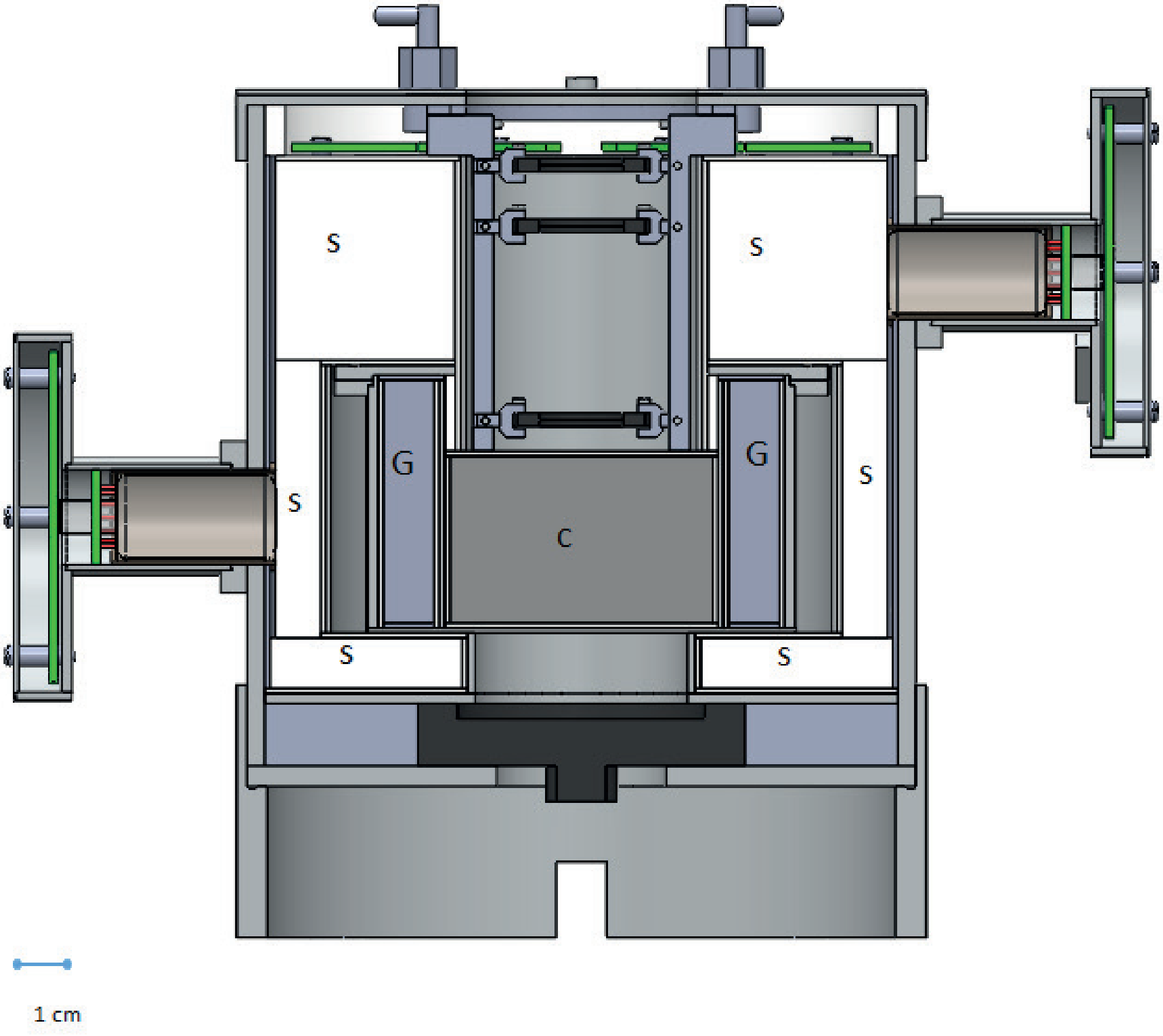

Figure 3-8: Rendered drawing of the cross-section of the PICAP prototype instrument. D1–D4 are in dark grey from top to bottom. PMT circuit boards are colored green. The two PMTs protruding from the sides are connected the anticoincidence shield S. PMTs for the G detectors are vertically mounted through cavities machined in S and are not visible in this cut-through.

Carlo simulations. In the simulations, the detectors were idealized geometric figures (e.g. perfect cylinders) of specific material floating unsupported in vacuum. Dimensions and positioning of each element could be varied, and the differences in overall performance could be observed with relative ease.

In designing a physical prototype from an idealized concept, additional components are required. Besides the detectors and detector materials, features were introduced for electrical bias and signal transport. Structural components were needed to securely hold components in place and shield the interior from external influences, effectively creating a Faraday cage. Choices of detector parts and materials often differed from their counterparts in the theoretical model and were based upon readily available inventory and performance considerations. We consider the potential impact of key differences between the prototype and the model.

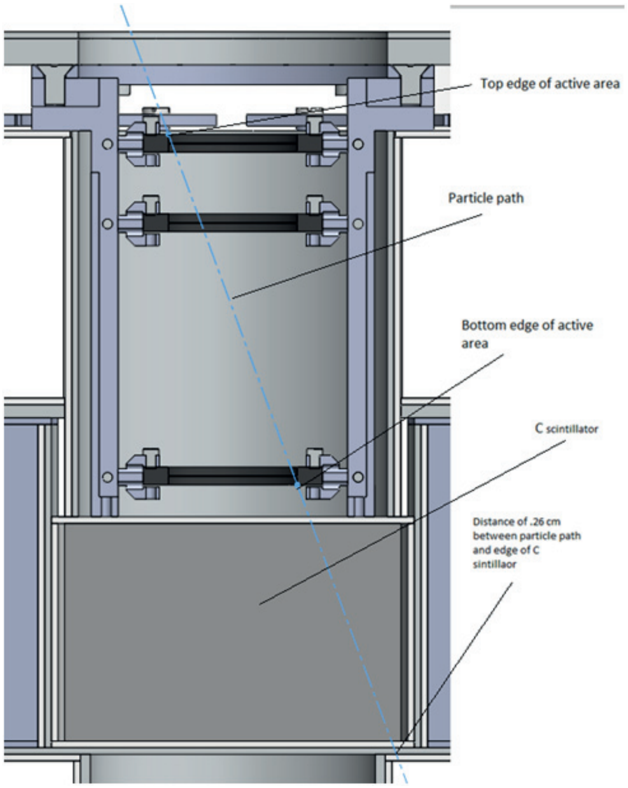

Figure 3-9: Illustration of the extent of particle geometry through the SSD column and the C scintillation detector.

At the time of prototype assembly, readily available inventory included silicon SSDs, to be reused from a previous experiment. The active surface area of the detectors used for D1, D2, and D3 was 300 mm^2, which gives them an effective radius of 0.977 cm, compared to 1.25 cm in the model. The SSDs are held in place by clips attached to plastic supports which also house the wiring for the detectors' electrical leads. This column of SSDs also differs from the model, as the spacing between detectors is increased by approximately a factor of two, to accomodate extra structural components of the prototype.

D4 was situated at the bottom of the detector stack. The SSD used for D4 (also 1000-μm thick) has an active area was 2000 mm^2 which corresponds to a radius of 2.65 cm, which is noteably smaller than the 5.25-cm radius of the D4 detector in the model. This was a compromise based on detector availabity, noise, and cost.

Below the set of SSDs, is the C detector, machined from a plastic polyvinyltouelene (PVT) scintillator. C was originally modeled as a nylon cylinder 3.3 cm in height with a radius of 2.25 cm. Nylon was the available material in the simulation code that most closely resembled plastic scintillator. To account for particles whose trajectory penetrates one edge of D1 through the opposite edge of D3 (see Figure 3-9), C was machined to be wider with a radius of 2.55 cm, which could improve particle detection efficiency by 19%.

Each scintillation detector was enclosed in a layer of polytetrafluoroethylene (known commercially as Teflon™). Most of the Teflon is held in place by compression against the internal aluminum structure or a neighboring detector. Combined with the opaque metal structure, the high index of reflectivity of white Teflon aids in light collection and makes it useful to optically isolate different detectors of the instrument. Each detector is attached to a photomultiplier tube (PMT) which converts light into a measurable charge pulse. The PMTs are optically coupled to the scintillator with optical grease or RTV silicone adhesive. The PMT for C protrudes from the side, reducing available space for the G1–G4 detectors (see Figure 3-10).

The decision was made to use a different inorganic crystal scintillator, bismuth germanate

($Bi_4Ge_3O_{12}$, or more simply, BGO), instead of CsI for G1 through G4. Compared to CsI, BGO has a greater density (7.13 g cm^{-3} vs 4.51 g cm^{-3}) and the bismuth has a higher Z than cesium (83 vs. 55). BGO is a superior scintillation material for absorbing γ-ray photons, particularly the annihilation photons that PICAP was designed to detect. BGO does have a lower light yield, compared to CsI, so it has a worse energy resolution; however, BGO is not hygroscopic. CsI is slightly hygroscopic, so energy resolution was sacrificed for practical considerations, as BGO does not require special protection from moisture in the air.

The original PICAP concept design uses four equal toroidal segments of CsI for the detectors G1–G4. Each detector is 2.3 cm thick (inner and outer radius is 2.45 cm and 4.75 cm, respectively) and 4.65 cm tall. We recall that the absorption probability of photons I/I_0 in a certain material of thickness x is

$$\frac{I}{I_0} = \exp\left(-\mu x\right) = \exp\left(-\sigma \rho x\right) \tag{3.4}$$

μ is the total absorption coefficient, or the inverse of the mean free path of the photon. We then take σ to be the total photon attenuation cross-section in units of $\mathrm{cm}^2\ \mathrm{g}^{-1}$ and ρ to be the mass density of the material. For CsI, $\sigma = 0.09082\ \mathrm{cm}^2\ \mathrm{g}^{-1}$ and for BGO, $\sigma = 0.1270\ \mathrm{cm}^2\ \mathrm{g}^{-1}$ for 0.511-MeV photons [Berger et al., 2010]. By equating the absorption probabilities, we found that one cm of BGO is 98% as effective at absorbing 0.511-MeV photons as the 2.3 cm of CsI from the original design.

The total mass of the four CsI detectors from the model would be 1.1 kg. By substituting BGO for G1–G4, the volume occupied by these detectors was reduced over 50% and the mass decreased by over 30%. Since the instrument has to accommodate a horizontally-oriented PMT for the central plastic scintillator C, G1–G4 only span 290° (72.06° per detector) about the axis of the instrument (Figure 3-10), resulting in a total mass of less than 600 g of BGO. Choosing BGO also reduced the size of the anticoincidence detector S surrounding the other detector elements and the overall size the aluminum housing and structure of the instrument, further reducing the total mass, useful

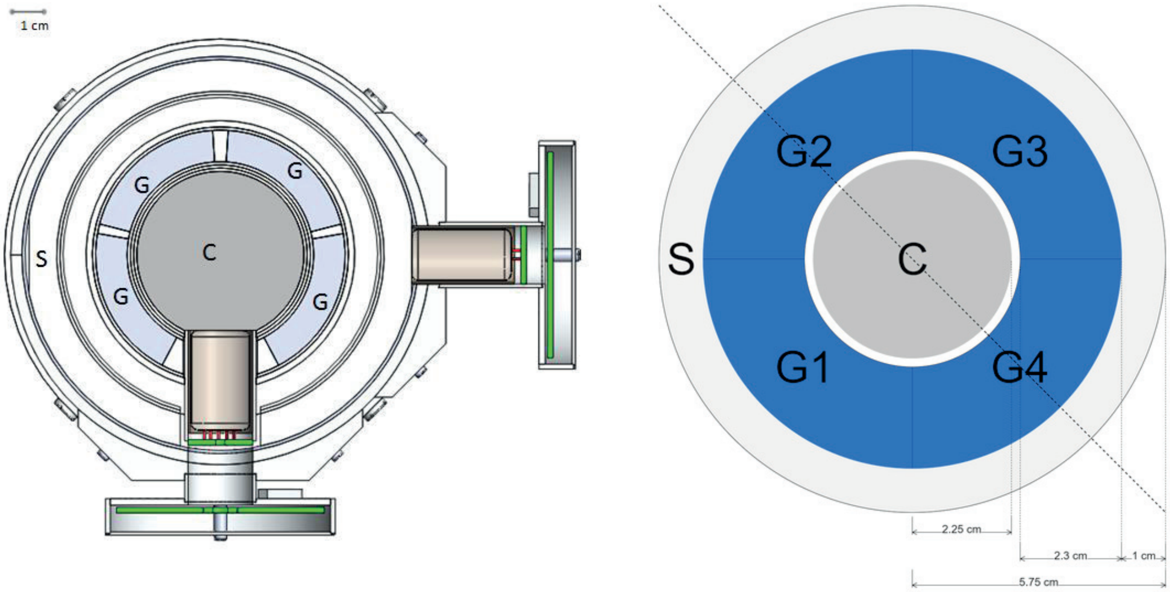

Figure 3-10: Side-by-side comparison of top-down cross-section of the G1–G4 detectors in the prototype and the theoretical model. The images are close to scale with each; however, the reduction in G detector thickness is clearly depicted as well as the need to accomade the PMT for the C detector.

toward the design of a space instrument.

A PMT is attached at the top of each G detector. The anticoincidence shield S is a combination of three parts (top, center, and bottom; refer back to Figure 3-8) also machined out of PVT scintillator. Cavities were machined into of the top part of S to accomodate the PMTs for G1–G4. S is relatively irregular in shape and is meant to serve only as a detector for rejecting particles that enter the stack from anywhere but the aperture, as well as those that scatter to the sides from within.

	Radius (cm)		Position Above C Detector (cm)	
	Model	Prototype	Model	Prototype
aperture	1.25	2.34	3.65	7.20
D1	1.25	0.98	3.15	5.50
D2	1.25	0.98	2.65	4.40
D3	1.25	0.98	0.50	0.60
C	2.25	2.55	—	—

Table 3.2: Differences in detector radii and vertical position (relative to the top of the C scintillation detector) between the PICAP model and the prototype instrument.

Figure 3-9 illustrates the straight-line trajectory of a particle considered to be within the geometry of the detector scheme and would not be rejected based on anticoincidence if it were stopping in C. The decrease in SSD size as well as the increase in spacing between detectors is not expected to change the detection efficiency of the prototype, when compared to the model. Detection efficiency is based on analysis and identification of only particles that satisfy the trigger requirements, mainly D2 and D3. Changing the SSD size does not alter the trigger requirements. However; from Equation 3.1, these changes (summarized in Table 3.2) reduce the geometrical factor from 1.48 cm^2 sr to 0.504 cm^2, which reduced the particle counting rate approximately by a factor of 3.

The reduced geometrical factor narrows the range of trajectories that particles of interest can have. These particle trajectories do not see most of the surrounding structural and passive elements introduced in the the prototype. A particle penetrating D2 and D3 will only encounter an additional 0.1-mm layer of Teflon before stopping in C. Similar to when considering the increase in thickness of D2 and D3, an extra layer of material will should only slightly increase the minimum particle energy that can be identified. The average energy loss of electrons in Teflon is comparable to the energy loss in the Si SSDs [Berger et al., 2017]. The energy loss to the Teflon would be less than 10% of the residual energy loss of a particle stopped in C.

Layer	Total Attenuation Coefficient (cm^2/g)	Density (g/cm^3)	Thickness (cm)	Relative 0.511-MeV Photon Intensity After Penetration of Layer
additional PVT	0.0935	1.032	0.3	97%
Teflon	0.0828	2.200	0.1	95%
Al	0.0831	2.700	0.1	93%
Al	0.0831	2.700	0.1	91%
Teflon	0.0828	2.200	0.1	90%

Table 3.3: The attenuation of 0.511-MeV photons emitted outwards from the C detector towards the G detectors. Compared to the theoretical model, there was additional material introduced in the prototype that an annihilation photon would encounter after emission, in order in the table from top to bottom. The right-most column shows the successive photon intensity, relative to annihilation photon emission in the model, as a result of each additional layer of material, when read top-to-bottom.

The differences between the PICAP model and prototype that potentially have the greatest impact on instrument performance is attenuation of 0.511-MeV annihilation photons by surrounding material between C and the G detectors (Table 3.3). Compared to our theoretical model, an annilhilation photon originating from the center of the C detector in the prototype would encounter the additional 0.3 cm of PVT, a 0.1-cm layer of Teflon, a 0.1-cm layer of aluminum, followed by another 0.1-cm layer of aluminum, and another 0.1-cm layer of Teflon before reaching a G detector. This reduces the probability that an annihilation photon reaches a G detector to 90%, compared to the Monte Carlo simulation.

The 0.3-cm increase in the radius of C is estimated to increase the effective area of C by 19%. Because electrons tend to scatter randomly, this would increase the probability of a negatron or positron stopping in C (and, subsequently, the detection efficiency) by 19%. Cumulatively the addition layers of material attenuate the intensity of annihilation radiation, such that probability of an annihilation photon reaching a G detector in the prototype is 90% of what the probability would be if the photon were unimpeded. Recall that in order to accommodate the PMT for the C scintillator, G1–G4 only surround 80% of C, where each detector spans an angle of ~70°. Taking that the BGO G detectors are 98% as effective as the 2.3-cm thick CsI detectors, the relative positron probability is

$$1.19 \times (0.9 \times 0.98 \times 0.8)^2 = 0.60 \tag{3.5}$$

The quantity is parentheses is squared to reflect that two annihilation photons but be detected. We would expect that the prototype instrument to perform 60% as well in identifying positrons when compared to the model. The response of the prototype should differ from the model by no more than a factor of 2. This also informed us that we would not have to take into account any special requirements, such as prolonged data collection time, when planning prototype testing. For example, if the impact of differences in components used were to result in a reduction of performance to 10% compared to the model, then we would have to accommodate accordingly and plan for more accelerator time.

The model provided us with a base level of expectation as to how the detector scheme works and the detection efficiencies and rates with an intended scientific application. It is not the exact schematic of a space-flight instrument, but rather the representation of the PICAP concept. The prototype instrument itself is an alternate representation of this idea, which we may alone use in evaluating PICAP's viability as an instrument. Together, the model and the prototype provided us with some reasonable expectation of the data we can collect at accelerator facilities, in order to test the PICAP concept's ability to measure positrons. Real-world data and results are the ultimate goal, and the model lends support to them. The next sections detail the steps taken to verify the prototype's functionality and prepare for accelerator testing.

3.7 Laboratory Electronics and Data Acqusition

The original PICAP concept estimated an instrument the size of approximately 6 cm in width and height with a mass of 4 kg. Fully assembled by January 2013, the total dimensions of the prototype are 17 cm in height and 12 cm in width. The total mass is 3.3 kg. While this number is lower than the mass budgeted in the original concept paper [Connell et al., 2008], it does not include electronics required for a fully functional space instrument. Operation of our ground-based prototype requires several racks of laboratory electronics.

The prototype instrument was designed to accommodate thin, custom cables extending from its exterior to be connected to series of modular laboratory electronics. For the scintillation detectors, their respective PMTs were outfitted with custom circuit boards for bias and to provide signal out to preamplifiers. For the SSDs, cables are directly attached via metal leads to the detector and held in place by each detector's plastic mounting clips or, in the case of D4, via an integral coaxial connector. All connections between the prototype's detectors and exterior electronics are made with the custom cables fitted with BNC connectors.

The modular electronics used are based on the NIM (Nuclear Instrument Module) standard. Each detector's output cable is connected to a series of NIM electronics organized in and powered by NIM bins (see Figure 3-11), starting with an Ortec 142 preamplifier which is then connected to an Ortec 590A amplifier. One of the amplifier's two output signals is a logic signal that triggers when the input signal exceeds a lower discriminator level that is manually set. The overall instrument logic required for a desired event is set by requiring the coincidence of one or more logic signals using an Ortec 418A universal coincidence module. The amplifier's other output is the amplified pulse signal, each sent through its own delay amplifier, an Ortec 427A.

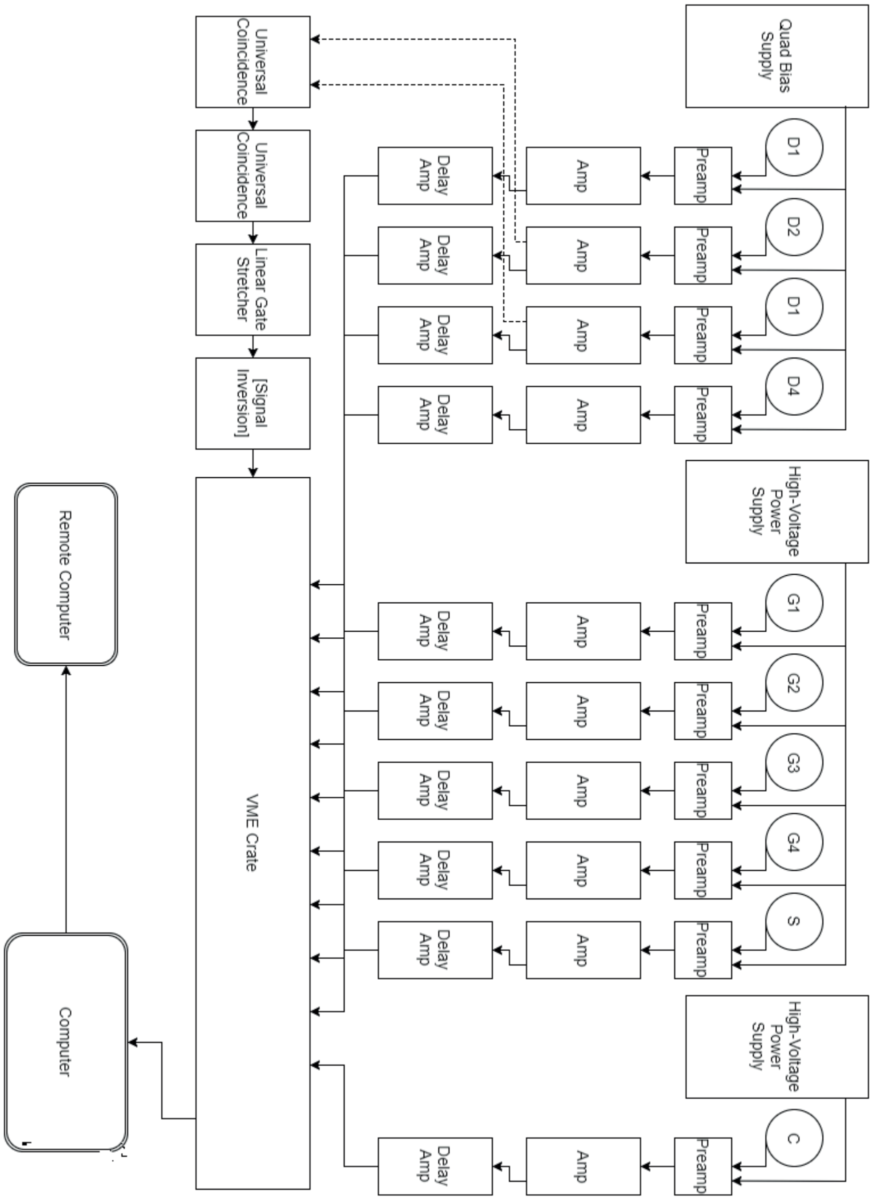

Figure 3-11: A system-level schematic of PICAP's electronics, from detector to data acquistion system.

After the NIM electronics, the signals are converted by a data acquisition system based on the VMEbus (Versa Module Europa) interface, which is a standard of computer-based modules organized in a VME crate. The main module in the VME crate provides an analog-to-digital converter (ADC) interface in 12-bit (4096-channel) resolution for the detector outputs of the NIM analog electronics. When the coincidence requirements are met in the NIM universal coincidence module, a logic signal is sent to the VME crate, triggering a conversion of the final processed signals from each delay amplifier. Since the coincidence requires a finite time, the delay amplifiers delay each signal so they arrive at the VME crate at the same time that the concidence requirement is met.

The data acquisition program, graphical user interface, and operating procedures were updated and improved for the VME crate by University of New Hampshire student Samuel Galletta in 2012 under our guidance and knowledge of the electronics arrangement and have been used extensively since then. The program was capable of displaying periodically updated energy histograms for each detector channel. Each time the coincidence requirements are triggered, the VME crate processes the data from each detector through its ADC channels, where each line of data represents one event. This is similar to the output of the EGS4 Monte Carlo simulations where each line of data is simply the energy deposition in each detector.

3.8 Initial Laboratory Testing: Establishing Liveness, Light-Tightness, and Cross-Talk

The fully assembled prototype was required to meet a set of basic requirements related to external interference. The aluminum housing of the parts of the instrument is already expected to serve as a Faraday cage, isolating the SSDs and PMTs. One requirement addressed is “light-tightness,” or the shielding of the interior of the instrument from ambient light. Both the PMTs and SSDs are light-sensitive. In addition to reducing the effects of outside light, we verified the minimal presence of “cross-talk” between scintillation detectors to ensure that they did interact with each other and were, therefore, sufficiently optically isolated from each other. Lastly, the prototype was required to have purge fittings installed in order to vent the interior with nitrogen gas. Purging protects the surfaces of the SSDs from airborne contaminants.

Before any further testing, the “live-ness” of each detector was established. This was the simple test that each detector channel produces a signal. With the prototype fully assembled and wired, each detector is individually biased. While a PMT’s gain increases with voltage applied, providing a means of adjustment, an SSD is operated at a single voltage for full depletion. Signals were viewed using an oscilloscope. Each detector, and consequently the signal-processing electronics in between, was shown to be active by observing the increase and decrease in activity on the oscilloscope while a ^{137}Cs γ-ray source was repeatedly brought close to and moved away from the instrument.

Similarly, apparent increases in the signals of several detector channels were observed when the laboratory lights were turned on, as opposed to when the laboratory was dark. This was evidence that the instrument was not entirely light-tight. Ideally, there should be no difference between detector signals in dark or lit rooms. Problematic areas on the exterior were identified by pointing a flashlight at different parts of the instrument in a dark laboratory and noting where the presence of the light caused a spike in activity on the oscilloscope. The major sources of light leaking into the instrument were openings for detector cables and edges and surfaces along where different machined parts were attached (either with screws or epoxy) were not perfectly flush against each other. The detector that suffered the most contamination from ambient light was the anticoincidence shield S, not surprising considering it is the outermost detector. Areas deemed to be contributing to light leaks were covered with black vinyl electrical tape (specifically Scotch® Super 33+™).

The amount of cross-talk was examined primarily between scintillation detectors since SSDs are not as sensitive to photons. This was done by allowing G1–G4 to trigger on a ^{137}Cs γ-ray source. In the absence of cross-talk, γ-rays from the source triggering one G detector ideally should not cause a signal of significant energy to be measured in one or more other detectors, even if they are physically adjacent. Scatterplots comparing the signals of different G detectors were generated to show that there was no correlation or entirely random correlation of signals between different G detectors.

Even though the scintillation detectors G1–G4 and C are closely arranged in the stack, they are optically isolated from each other by Teflon and aluminum. Aluminum is opaque, while the Teflon has reflective properties acting as a guide for each scintillator's emitted light to be collected by each scintillator's respective PMT. The G detectors produce more light than C, increasing the potential for them to contaminate the C detector.

3.9 Calibration of BGO Detectors (G1–G4)

The scintillation detectors labeled G1–G4 are four toroidal segments of bismuth germanate (BGO) whose role is to detect 0.511-MeV γ-ray photons. Ideally, this requires that each detector's electronics channel is properly adjusted to measure signals, such that the center of resulting energy spectral peaks correspond to 0.511 MeV. Part of the requirement for the identification of a positron are single 0.511-MeV signals in two different G detectors; however, both photons from a positron annihilation may deposit in the same G detector. This case is geometrically less probable, but we wanted to have the capability of detecting 1.022-MeV signals.

The VME crate processes each detector output signals into one of 4,096 ADC channels that ultimately yield an energy spectrum over the course of a data collection run. The goal was then to set the overall gain in each channel, so that channel number 1365 or 1366 (of 4096, or approximately one-third of the maximum measurable energy) corresponds to an energy of 0.511 MeV, and consequently, channel 2730 or 2731 corresponds to an energy of 1.022 MeV. The target conversion gain for the electronics for each G detector is, therefore, around 3.74×10^{-4} MeV per channel. The maximum energy of a signal that can be measured in each G detector, before the electronics are saturated, would be 1.533 MeV.

As was with the initial tests to show that the detectors were functioning (the "live-ness" test), a ^{137}Cs photon source was used for calibration. The ^{137}Cs gamma spectrum has a 0.662-MeV photopeak. A source of 0.511-MeV photons, such as sodium-22 (^{22}Na), of sufficient strength was not simply available at the time of initial calibration. With the target conversion of 0.374 keV per channel, this corresponds to approximately channel number of 1770.

To obtain calibration data for any one G detector, the coincidence module requirements were set so that the VME crate collects data on a trigger of that particular detector. The trigger level is set by manually adjusting the lower level discriminator to ensure that the signal exceeds the pedestal of the electronics. With the aperture of the instrument oriented upright, the ^{137}Cs source placed above the aperture to ensure uniform distribution of γ-rays across all G detectors. Initially, amplifier gain settings were adjusted based on the live histogram display from the data acquisition software such that the peak would be located close to the desired channel. Each data collection interval was typically around five minutes.

After processing the raw data files, energy spectral histograms are produced (Figure 3-12) for each detector. Each histogram was then fitted to a modified Gaussian normal distribution curve of the form:

$$f(x) = y_0 + A \exp\left(\frac{(x - x_0)^2}{2\sigma^2}\right) + B \exp\left(-C(x - x_0)\right) \tag{3.6}$$

x_0 is the location of the peak and σ is the standard deviation, which is a measure of the characteristic width of the peak and its energy spread or resolution.

One calibration point against a standard source with spectral peaks of known energy is typically not considered adequate; however, a measurement of the pedestal with a pulser was made to determine the channel number corresponding to a zero signal. With the measurement of the electronic pedestal (which was taken to be ~150 channels), we were able to reasonably estimate the conversion gain of each detector.

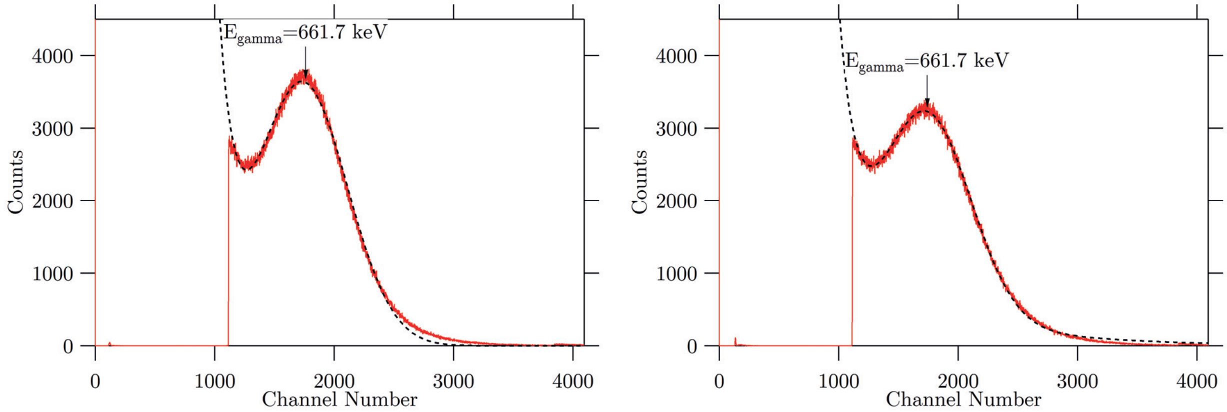

(a) G1, peak channel 1735, σ=376

(b) G2, peak channel 1753, σ=361

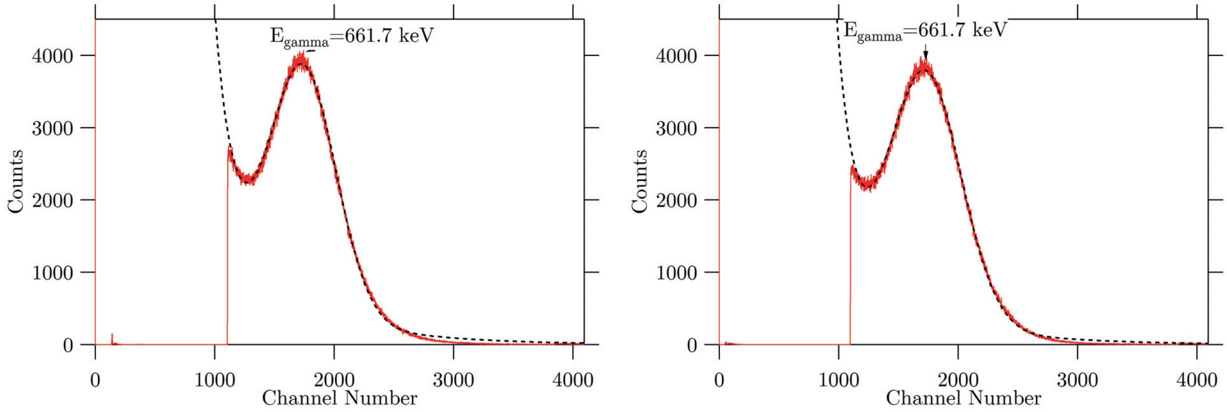

(c) G3, peak channel 1743, σ=274

(d) G4, peak channel 1731, σ=297

Figure 3-12: Gamma calibration spectra for G1–G4 with a ^{137}Cs source. Each spectral peak, with an energy of 0.662 MeV, is fitted with modified Gaussian peak (dotted line). The width(σ) of each peak ranges from 15–20% of the measured energy.

This process was not meant to obtain an exact calibration of the each detector. The purpose was to establish that the electronics were adjusted properly for 0.511-MeV photon detection in each of these detectors. The calibration process was repeated at the conclusions of the proton and electron experiments with ^{22}Na sources that were provided on-site. These calibrations carried greater importance, because they were performed closer to the time of their respective accelerator tests and are a more accurate reflection of the respective experimental setup. These data are discussed in Chapters 4 and 5, respectively.

3.10 Detector Calibration With Atmospheric Muons

C is the plastic scintillation detector central to the stack, where electrons in the energy range of interest are expected to stop after having penetrated the first three SSDs D1–D3. Due to the low sensitivity of plastic scintillators and silicon SSDs to γ-ray photons, calibration with gamma sources is not as suitable for these detectors as they are for G1–G4, which are specifically crystal γ-ray detectors.

We are not able to calibrate with an alpha source, such as ^{241}Am, as there was no practical way to place the entire assembly and wire electronics under vacuum or orient the source in close enough proximity to each detector (i.e. inside the detector stack). Readily available higher energy beta sources do not exist (else, there would be little need for particle accelerator trips). The alternate method of calibration is with atmospheric muons.

Atmospheric muons are charged particles created as secondaries by cosmic ray interactions in Earth's atmospheric. They are highly relativistic and are considered to be minimally ionizing particles. We can take advantage of D1–D4 and C being aligned along the axis of the prototype instrument and calibrate all four detectors with muons that penetrate the stack. The following muon calibration process was performed at least once prior to each particle accelerator experiment to ensure consistency of the electronic response.

Calibration requires knowledge of energy losses of muons in each detector. These values were calculated based on stopping power and range table data for muons. We used an index of tables (found in Groom et al. [2001]) that list the mass density ρ and average energy loss at minimum ionizing $\langle dE/dx_{\min}\rangle$ in several elements, compounds, and mixtures. The product of ρ and $\langle dE/dx_{\min}\rangle$ is the average linear muon stopping power per unit length, but we know the respective thicknesses of our detectors. The expected muon energy loss E_μ is just the product of ρ, $\langle dE/dx_{\min}\rangle$, and detector thickness Δx (refer to Table 3.4).

Table 3.4: Calculated expected energy loss of atmospheric muons in detectors along axis of PICAP detector stack

Detector(s)	Material	Δx (m)	ρ (g/cm^3)	$\langle dE/dx_{\min}\rangle$	E_μ (MeV)
D1	Si	0.0050	2.329	1.664	0.019
D2, D3, and D4	Si	0.1000	2.329	1.664	0.388
C	PVT	3.3000	1.032	1.956	6.661

Note that the intrinsic noise was determined in each SSD, so a measurable signal must exceed this noise. A muon measurement of 20 keV falls well below D1's intrinsic noise level of 75 keV and cannot be measured. D2, D3, and D4 are all 1000-μm thick and should each measure a total average energy loss of 0.388 MeV from an atmospheric muon. This is well above the 45-keV noise in D2 and D3, as well as the 75 keV of noise in D4.

To perform a muon calibration, the prototype instrument is oriented with the aperture facing up towards the sky. The universal coincidence module is set to allow the VME crate to record signals from the instrument on simultaneous triggers of D2 and D3. This coincidence requirement is the standard condition for particle accelerator testing and ensures that the trigger occurs for a particle penetrating D2, D3 and, presumably, C. The duration of data collection is typically over the course of a day or overnight, due to a modest rate of muons passing through the aperture of the instrument.

The conclusion of the calibration run yields the energy loss spectra for C and D2–D4 (Figure 3-13). The majority of events from the simultaneous trigger requirement of D2 and D3 appeared to be accidentals. In order to clean up the data, we limit our scope of analysis by selecting a subset of events whose energy loss falls within a range of channels around the apparent muon peak in C. Each resultant histogram is fitted to a Gaussian. The peak of each Gaussian corresponds to the energies in Table 3.4.

Combined again with a pedestal measurement of ∼150 channels, the calibration gives us an approximation of the energy per histogram channel. Multiply this number by the total number of channels (4096) gives us the maximum energy that can be measured with the detector before it saturates. The muon peak for C is located at channel 2364, so the conversion gain of the detector was ∼2.9 keV per channel, with the detector capable of measuring signals up to around 12 MeV.

We notice that for D4 (see Figure 3.4 again), there were two prominent peaks visible when examining the raw data; however, the subset of data containing the C muon energy loss peak does not include either of these peaks from D4. Most of the events fall in a region between the two original peaks. This suggests that this region represents some kind of detector or electronics noise that signals were unable to exceed, or D4 was not functioning properly. This was perhaps the first instance of the unreliability of this detector.

Muon calibration is particularly useful because there were few other methods available to us for calibrating D2 and D3. The muon calibration provided us with at least one calibration point and helped to estabish relatively equal gain setting for D2 and D3. Furthermore, the EGS4 Monte Carlo simulations showed that electrons of both charges lose ∼0.3 MeV in D2 and D3 which is similar to the 0.388 MeV energy loss by muons. Adjusting the electronics for muon testing helps to prepare D2 and D3 for electron detection.

Muon exposure yielded a low rate of data over the duration of a run, typically on the order of a day or two. Due to the transparency of the plastic scintillator (PVT) in C toγ-ray photons, obtaining precise calibrations with photopeaks from gamma sources is not practical; however, we were able to measure Compton edge, which is the maximum amount of energy deposited from the

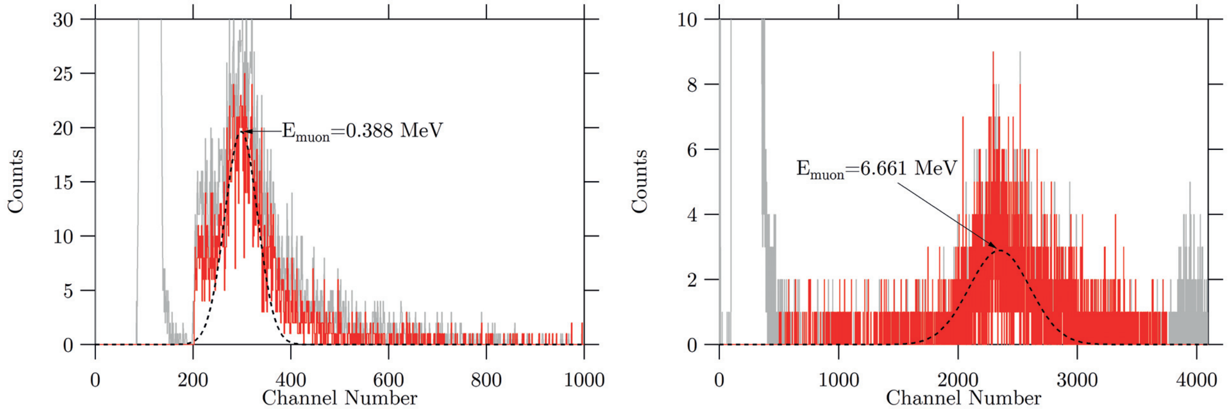

(a) D2, peak channel 298, σ=34

(b) C, peak channel 2347, σ=254

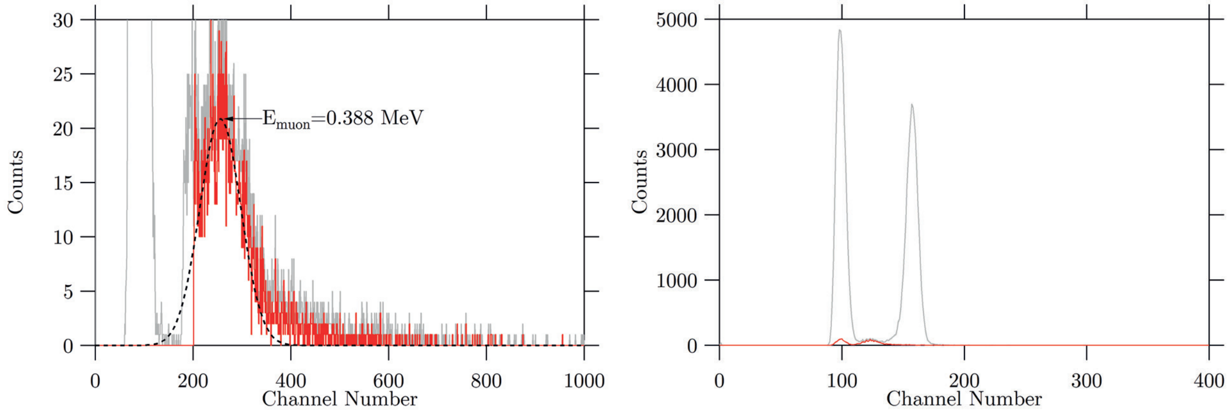

(c) D3, peak channel 256, σ=42

(d) D4

Figure 3-13: Initial muon calibration histograms of C, D2, D3, and D4. The raw data is colored grey. Plots shown in red represent the subset of events within the muon energy loss peak in C. In the case of D4, this subset notably does not include the second peak (in grey), indicating that it does not correspond to muons and was likely a background peak.

Compton scattering of γ-rays in the detector. The additional Compton edge measurements were used to validate the muon calibration process, which validates the initial of calibrations of D2 and D3 as well. Measurements were made with ^{137}Cs as well as a ^{60}Co source that was available at the time for a limited use. ^{137}Cs emits γ-rays with energy of 0.662 MeV. The energy of the Compton edge, E_{Compton} is calculated using the following formula:

$$E_{\text{Compton}} = E_\gamma \left(1 - \frac{1}{1 + \frac{2E_\gamma}{m_e c^2}} \right) \tag{3.7}$$

E_γ is the γ-ray photon energy. The Compton edge of ^{137}Cs is located at 0.477 MeV. ^{60}Co emits photons with energies of 1.173 MeV and 1.332 MeV, which correspond to Compton edges of 0.963 MeV and 1.118 MeV, respectively.

To measure the Compton edge location, a Gaussian was fitted to the local maximum in the spectra (Figure 3-14). The Compton edge is then located at the channel where the spectra is half of the value of that local maximum, which is approximated by where the Gaussian fit reaches its full-width half-maximum.

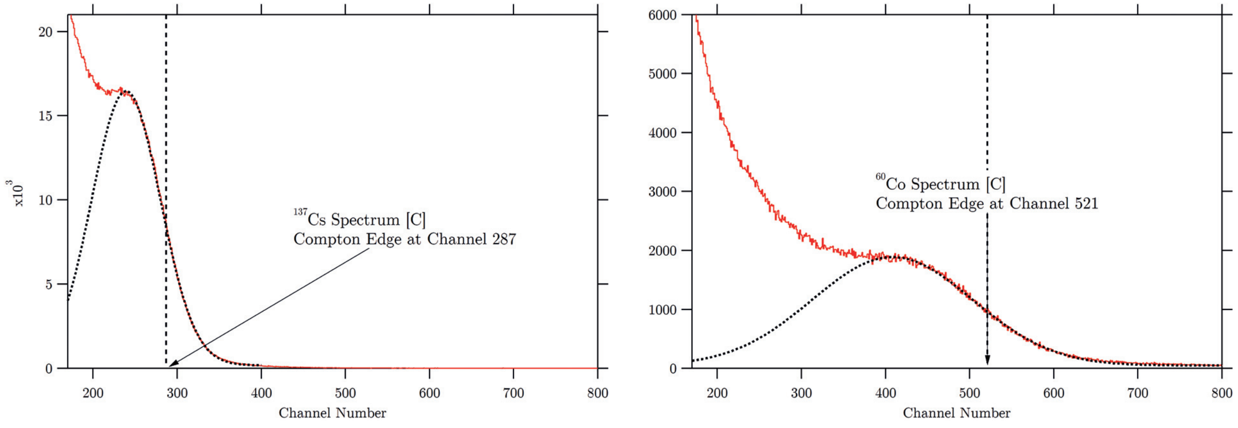

(a) measured = 0.512 MeV, actual = 0.477 MeV

(b) measured = 1.194 MeV, actual = 0.963, 1.118 MeV

Figure 3-14: Spectra for C using ^{137}Cs and ^{60}Co gamma sources, including measured and calculated Compton edge measurements. Compton edge measurements were used to verify the conversion gain of C by muon calibration. The measured value is based on muon calibration. Note that ^{60}Co has two Compton edges, each corresponding to one of its principal photopeaks.

After we measured the location of the Compton edge, we converted to an energy using the muon calibration of the C detector. The Compton edge of ^{137}Cs was measured to be 0.512 MeV, compared to 0.477 MeV. The Compton edge for the ^{60}Co spectrum was measured to be 1.194 MeV, which lies closer to the calculated value of 1.118. The measured values fall within 10% of the expected values, validating the calibration of C, D2, and D3. This level of accuracy was acceptable, as these calibrations were never originally meant to be highly precise.

The purpose of the calibrations were to check that the detectors and accompanying electronics were functioning the way that we expected that they should. We were also gauging the appropriate electronics settings, particularly amplifier gains and PMT bias voltages, such that the detectors can measure signals at the energies we intended to measure, without saturating the data acquistion system during planned accelerator experiments. These calibrations informed future similar calibrations that were performed immediately before and after each accelerator experiment to more accurately reflect the conditions at the respective time. The calibrations would be used to establish particle identification criteria in the form of signal thresholds/cuts applied to the data output of each detector per event.

CHAPTER 4

PROTON EXPERIMENT AT BURR PROTON BEAM THERAPY CENTER

4.1 Purpose

PICAP proton accelerator testing was conducted on 1 June 2013 at the Francis H. Burr Proton Beam Therapy Center at Massachusetts General Hospital (MGH) in Boston, Massachusetts. It was the first of two particle accelerator runs scheduled for the PICAP prototype. The goal of the experiment was to demonstrate PICAP's ability to discriminate protons from positrons and electrons (where "electrons" collectively refers to both negatrons and positrons). While the instrument was designed specifically for positron identification (a few MeV or greater), protons are significantly more abundant than negatrons (by a factor of ∼10 or more in interplanetary space), which are in turn more abundant than positrons (by another factor of ∼10 or so); therefore, the ability to reject protons is especially important in the viability of the PICAP detector scheme.

Protons will travel at a lower velocity and lose more energy in matter ($dE/dx \sim 1/v^2$), because they are more massive than positrons at similar energies. PICAP then distinguishes electrons from heavier particles with redundant dE/dx measurements in its initial sequence of solid-state detectors (SSDs) D1–D3 at the top of the stack. If the prototype effectively rejects protons from identification, then it would presumeably be able to do so with other heavier ions. Ions with a higher nuclear charge would also be excluded, because they also lose more energy in matter (which goes as $\sim Z^2$).

This current PICAP design was based on positron energies ranging from around 2–10 MeV. The proton beam energies selected for this run are generally an order of magnitude above this energy range. We did not expect that notably higher energy protons could potentially masquerade as electrons in the 2–10 MeV energy range. Having calculated the expected energy loss in different detectors in the stack for protons and electrons, this is unlikely and we expected to confirm this experimentally. Furthermore, a minimum ionizing proton (~2000 MeV) penetrates the PICAP stack with ease and would trigger D4 and/or S and be rejected from identificaton, and beyond minimum ionizing, dE/dx increases.

The main objectives of the experiment are to determine whether, and at what level, protons can be mistakenly identified as positrons and electrons. This is done by applying the electron and negatron identification criteria to the proton beam data. Experimental preparation and arrangement, detector calibrations, and the final identification totals are presented.

4.2 Range Analyses: Proton Energy Loss In PICAP

An important tool for preparing and understanding the results from this experiment is a computer program, written by the principal investigator, James Connell, capable of doing range analysis of charged ions through a user-defined stack of matter. The range analysis program is based on heavy charged particle range tables by Barkas and Berger [1964]. The energy loss of protons through matter was discussed in a previous chapter of this work, based on the theory of Bethe and Bloche. Recall that energy loss of heavy, singly charged particles is largely dependent on their incident velocity, or energy. Range is a measure of how far a particle is projected to travel before losing all of its energy. The aforementioned tables are semi-empirical databases of ranges calculated for an array of incident velocities/energies in different materials.

The program, written in C and called `range_anl`, prompts for the number of layers of material, the types of material, and the areal density of each layer (in units of g/cm^2). PICAP's central detector stack is listed in Table 4.1, ignoring space and other materials (such as few thin layers of aluminum and Teflon) in between detector elements. The particle's angle of incidence (with respect to axis of the stack of layers), electric charge Z, and mass number A, must also be specified. Protons have $Z = 1$ and $A = 1$.

Table 4.1: A table of the input parameters for the central part of the PICAP detector stack. PVT was not an option in the program and was substitute with Lucite.

Detector	Material	Thickness (cm)	Areal Density (g/cm^2)
D1	silicon	0.0050	0.011645
D2	silicon	0.1000	0.2329
D3	silicon	0.1000	0.2329
C	polyvinyltoulene (PVT)	3.3000	3.4056
D4	silicon	0.1000	0.2329

The `range_anl` program takes these input parameters to perform the following useful functions to our experiment: calculating the average energy loss of a proton through material of specified thickness, calculating the mininum energy required to fully penetrate some material, and if the incident energy is not sufficient to penetrate the stack, specifying the layer in which the proton has stopped and calculating how deep it is projected to travel. For the stack defined in Table 4.1, energy loss in each detector was calculated and listed in Table A.1, located in the Appendix of this work for several pertinent proton energies (Table A.1 will extensively be referenced in this chapter).

Part of the preparations for the experiment included determining proton beam energies. Beam energies were strategically selected to reflect two main scenarios: protons reaching and stopping in the central scintillation detector C and protons that completely penetrate the entire detector stack. The logic for positron and electron identification requires that the particle stops in the central plastic scintillator C. Negatrons and positrons are partly identified by the amount of residual energy they lose in C when stopping; however, we do not expect protons stopping in C to be fast enough to mimic the behavior of a negatron or positron. When combined with the stringent requirement of coincident 0.511-MeV annihilation photon detection, we expected to be able to demonstrate PICAP's effective ability to reject protons from identification.

Assuming that the space between detector elements results in negligible energy loss and that protons travel in a near straight-line trajectory, the path a proton sees is primarily three layers of silicon (D1–D3) and a single 1-mm layer of Teflon before penetrating C. According to `range_anl`, the minimum energy required for protons to fully penetrate these layers is 68.8 MeV. When adjusted for an additional 1-mm layer of aluminum and Teflon that support the bottom of C, this number is closer to 70 MeV. This is the maximum energy a proton can have and still be able to stop in the C detector. Protons with energies upwards of 2000 MeV (at minimum ionizing) penetrate the instrument with ease and would be rejected from analysis by D4 or the anticoincidence shield S.

4.3 Experimental Arrangement And The Beam

The cyclotron at the Burr Proton Therapy Center operated at one of three beam transport energies: 101.56 MeV, 160.7 MeV, and 228.9 MeV. Specific beam energies are delivered by the accelerator facility with a series of energy absorbers or degraders, which were primarily slabs of brass and Lucite with varying thicknesses placed at the end of the beam line.

A UNH-built variable aluminum beam energy degrader was also placed between the end of the beam line and the entry aperture of the PICAP prototype instrument. The beam energy degrader consists of two adjacent aluminum wedges that are periodically raised and lowered on a motorized pulley system. The wedges are oppositely oriented and raised and lowered in opposite directions, effectively creating an aluminum target that constantly varies in thickness between 0 cm, the "open" position, and 2 cm, which could likewise, be referred to as the "closed" postion. The energy degrader created a spectrum of proton energies, as opposed to a monoenergetic beam delivered by the facility. This more realistically represents the space environment and provides data to test PICAP's ability to reject protons of any energy on an event-by-event basis.

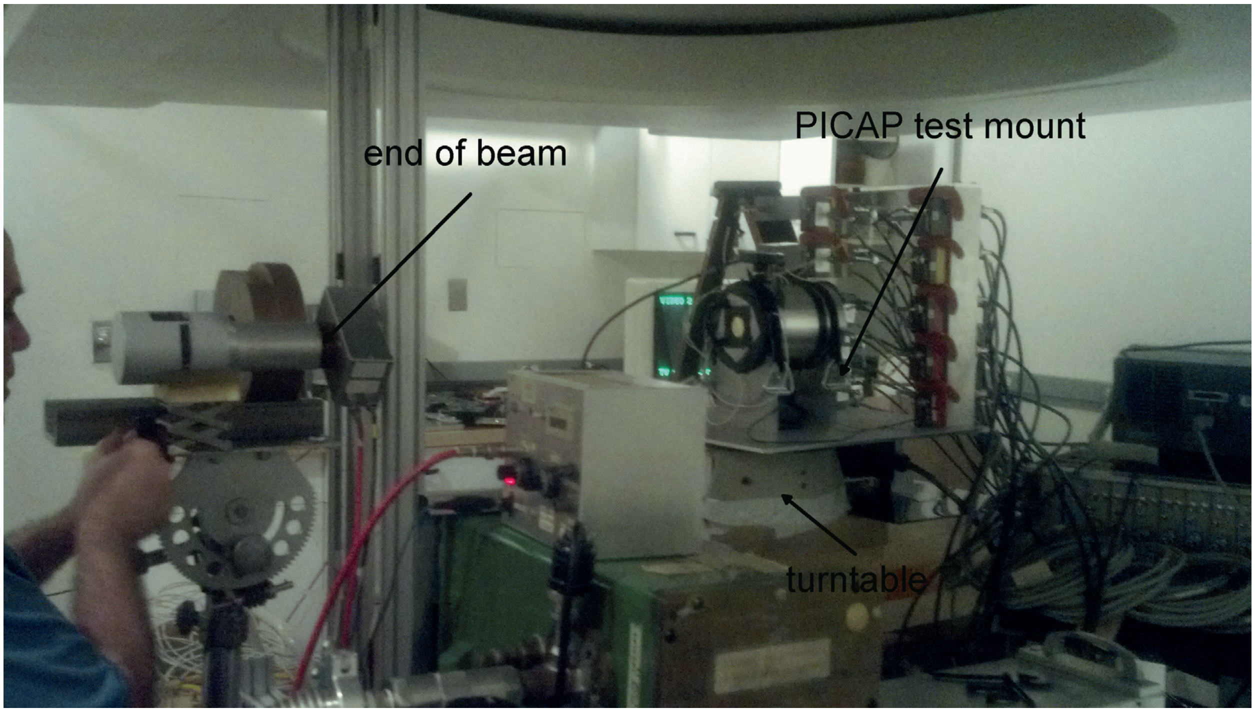

(a) prototype mount with detector preamps

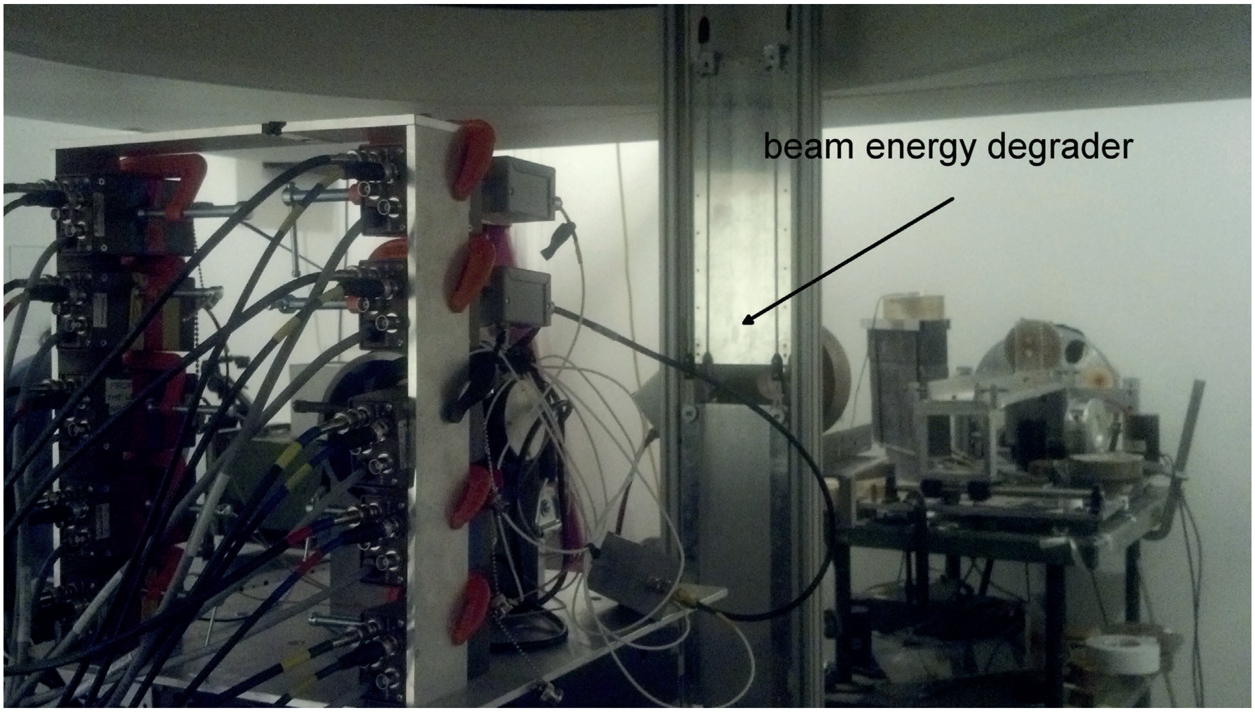

(b) beam energy degrader

Figure 4-1: The PICAP prototype instrument positioned on its mount in the experimental room at the end of the beam line, behind the aluminum beam energy degrader. The mount was fixed to rotation plate to set the angle of incidence. The beam energy degrader periodically opens and closes to vary the beam energy.

Positron and electron events are only considered for identification if they stop in the central plastic scintillation detector C. From our initial range analysis, we determined that incident protons that stop in the C detector do not exceed ~70 MeV in energy. The beam was tuned to 101.6 MeV and degraded to 69.5 MeV. Coincidentally, 2 cm of aluminum is capable of stopping 69.5-MeV protons at normal incidence, confirmed by the range analysis program, so the energy degrader turns the monoenergetic 101.6-MeV beam into a proton energy spectrum of 0–69.6 MeV at the instrument aperture. For the majority of the experiment, the beam operated at its maximum energy of 228.9 MeV (see Table 4.2 for beam energies and angles of incidence).

Table 4.2: A summary of proton beam trials for this experiment, including the nominal beam transport energy, the final beam energy, the spectrum of energies created by the energy degrader, and the angles of incidence.

Nominal Beam Energy (MeV)	Output Energy (MeV)	Beam Degraded Proton Energies (MeV)	Angles Of Incidence			
228.9	214.9	196.2–214.9	0°	12°	45°	180°
228.9	214.9	(monoenergetic)	0°	—	—	—
228.9	179.1	157.7–179.1	0°	12°	45°	180°
228.9	160.6	137.4–160.6	—	—	—	180°
228.9	145.1	120.0–145.1	0°	12°	45°	—
101.6	69.6	0–69.5	0°	12°	45°	180°
101.6	69.6	(monoenergetic)	0°	—	—	—

The prototype rested on its side on a custom aluminum mount and plate that was attached to a motorized, remotely controlled turntable. The turntable provided fine rotation control to alter the particle angle of incidence. The rotation axis is located at the top of the C scintillator closest to the instrument aperture. Besides normal incidence, we rotated the instrument to 12° and 45°, as well as reversed the orientation of the instrument (180°) with respect to the beam. 12° is the maximum angle the instrument may be rotated, such that a particle traveling in a straight-line trajectory penetrates D2 (refer to Figure 4-2) and the center of D3.

An angle of incidence of 45° represents an extreme case, yet some out-of-aperture protons are expected to penetrate both D2 and D3 at this angle due the beam having a finite width as opposed to being perfectly co-linear. At 180°, where protons enter the stack from the reverse direction, most

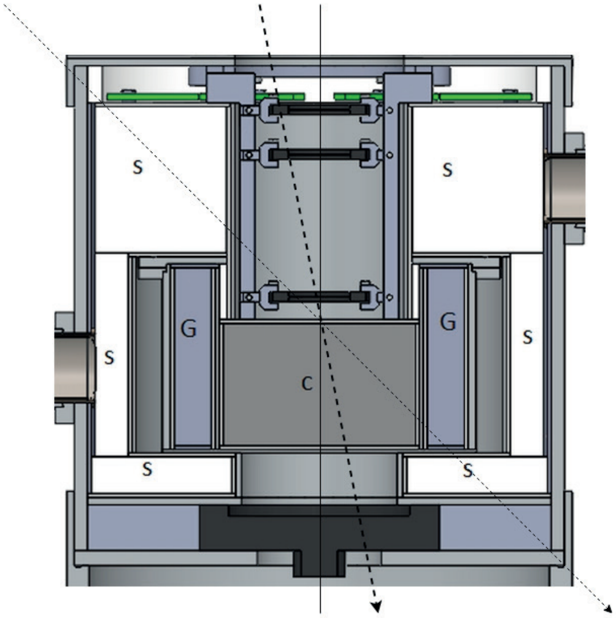

Figure 4-2: The PICAP prototype's rotation axis was centered at the top of C. The diagram illustrates the trajectories of protons incident at 12° and 45° (dotted lines). 12° is the maximum angle at which a *single* particle penetrates D2; however, with a *beam* of finite radius, some particles do penetrate both D2 and D3 at wider angles of incidence, satisfying the trigger requirement.

are expected to be rejected by D4.

We used the same arrangement of NIM rack electronics, with the equipment sdetailed in the previous chapter (Figure 3-11). To reiterate, each detector channel consists of the following chain of electronics: SSD or PMT, preamplifer, amplifer, delay amplifier, and finally, the VME crate and data acquisition computer, which was operated remotely from outside of the beam vault (so as not to expose the operators to radiation). The D2 AND D3 trigger requirement for data collection was implemented by the universal coincidence module.

Detector calibration depends on the type and material of the detector, as well as the settings of the electronics. We must note that prior to the start of testing, gain settings were manually adjusted after performing the calibrations presented in the previous chapter. On each amplifier the gain is manually set from 0.5X to 1250X with knobs for coarse and fine adjustment. An increase in amplifier gain decreases what we previously referred to as conversion gain, which is the amount of energy per unit channel. Settings adjustments were done to maximize collection of non-saturated data with protons.

The amplifier gain for C was reduced from 15.7X to 7.86X, which doubles the energy per channel and doubled the maximum energy that can be measured before the signal saturates. The amplifier gain for D3 was increased by 57% from 50X to 78.6X. We confirmed these changes in settings by calibrating with the monoenergetic beam trials (Table 4.2) and compare the results to the last muon calibration from Chapter 3. Finally, the amplifier gain was increased for D1 from 50X to 250X in an attempt to increase the signal measured; however, this proved to be futile because the signal must exceed the detector noise of 75 keV. According to the range analysis, most of the protons produced by the beam in the experiment would not register a large enough signal to trigger D1.

Several of the techniques employed in the previous chapter with simulation data, as well as preliminary laboratory calibration, were applied to the data from this proton experiment. While the goal was to demonstrate the PICAP's overall response to protons, we also wanted to be able to characterize individual components of the instrument where possible. Calibration also confirms whether instrument response remained consistent or changed in transit to the accelerator facility.

The majority of beam trials were 15 minutes, except for trials where the incidence angle was 45°, which were run for only five minutes. The beam degrader was in operation for the majority of our trials to expose the prototype to a spectrum of proton energies; however, we first took advantage of the two monoenergetic accelerator runs, set at the lower and upper limits of deliverable beam energies. In the absence of energy degradation, monoenergetic protons were expected to have relatively consistent average energy deposition in detectors along the axis of the instrument. These trials then offered reliable calibration data, relevant to the environment, compared to when the instrument was previously calibrated with muons.

4.4 Detector Calibration With Monoenergetic Protons

Two beam trials were taken without using the beam energy degrader, one at 69.5 MeV and one at 214.9 MeV. The advantage of monoenergetic beams was the energy loss expected in each detector could be calculated and used for calibration. Based on range analysis (excerpt from Table A.1), the energy losses in each detector are as follows:

Incident Proton Energy (MeV)	ΔE(D1) (MeV)	ΔE(D2) (MeV)	ΔE(D3) (MeV)	ΔE(C) (MeV)	ΔE(D4) (MeV)	Final Energy (MeV)
69.507	0.091	1.829	1.829	49.729	9.563	6.465
214.870	0.040	0.798	0.798	14.710	0.826	197.697

Table 4.3: ΔE is the energy loss in each detector. This is idealized as it ignores air and structural elements in the prototype instrument, such as thin layers of aluminum and Teflon.

As will be evident, 69.5-MeV protons could fully penetrate C but stop in the 1-mm layer of Teflon and 1-mm layer of aluminum (for structural support) under C, without triggering D4. Even though protons barely energetic enough to penetrate would not be rejected by D4 triggering, they should still be rejected based on their residual energy loss in C, which is large compared to the moderate energy range of electrons for which PICAP was designed.

The duration of each trial was 15 minutes. The energy loss histograms/spectra for D1, D2, D3, C, and D4 were produced (Figure 4-3) to include all of the events that do not saturate G1–G4 (as saturation suggests proton penetration) or the anticoincidence shield S, which occurs when a signal exceeds channel number 3840 of the 4096-channel multichannel analyzer. G1–G4 were configured to detect 0.511-MeV annihilation radiation, so saturation is likely for from anything other than a γ-ray. The raw data is shown in grey and the reduced data after removing these events is shown in red. Energy loss peaks were fitted with standard Gaussian curves.

The location of the energy loss peak of D2 is consistent with energy loss peak from muon calibration in the previous chapter (Figure 3-13). The conversion gain is estimated to be $\sim$1.3 keV per channel in both cases, calculated by taking the energy of the peak and dividing by the channel

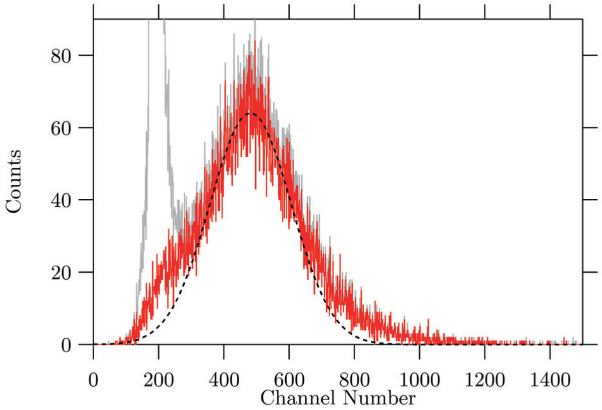

(a) D1 (91 keV), 481.3 σ=124.8

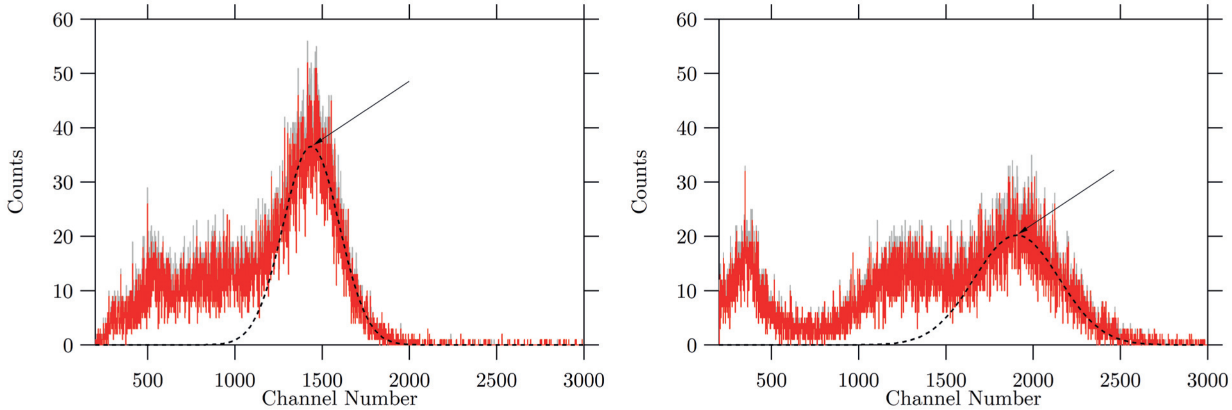

(b) D2 (1.829 MeV), 1436.7 σ=160.5

(c) D3 (1.829 MeV), 1904.8 σ=243.4

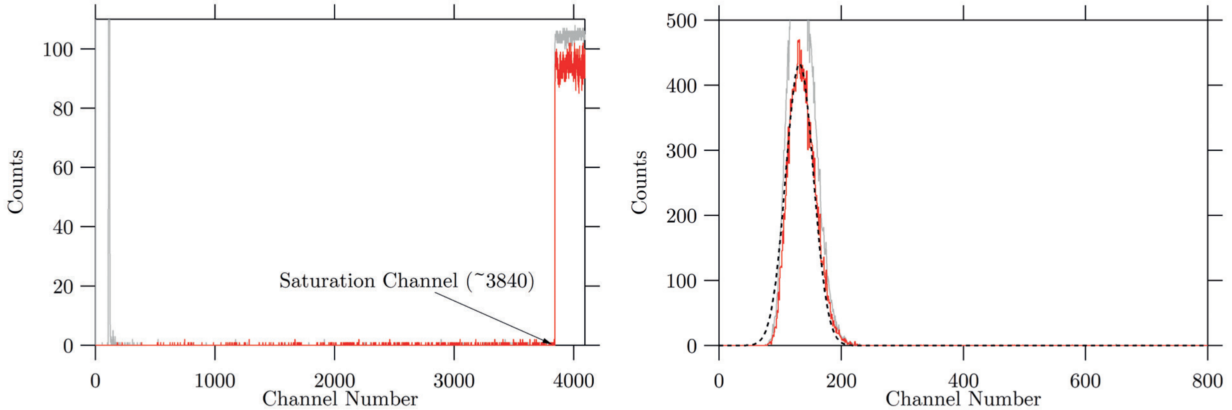

(d) C (>49.729 MeV)

(e) D4 (noise)

Figure 4-3: Proton energy loss histograms with 69.5-MeV monoenergetic beam for detector calibration. The theoretical energy deposition is given, alongside with the peak location and width of the Gaussian fits (dotted lines), in channels. The spectra strongly suggest that most of these protons stop in C without triggering D4.

number. The amplifier gain of D3 was increased by 57% so the energy per channel should decrease by 63%, when compared to the muon calibration results. Taking the same estimation with the ratio of the energy to channel number of the energy loss peak, the conversion gain decreased to 0.96 keV per channel compared to 1.5 keV per channel during the muon calibration. This decrease in energy per channel is consistent with the increase in the amplifier gain.

Recall that the intrinsic noise in D1 is 75 keV, so the energy loss of a 69.5-MeV proton of 91 keV seemed great enough to measure; however, we are unable to compare this to another calibration. The energy loss of atmospheric muons in D1 is 20 keV and the energy loss of 214.9-MeV protons is only 40 keV, which do not exceed the noise. The peak in histograms for D1 must represent noise, not being great enough to exceed the intrinsic noise of this detector. The best we were able to do was to fit a Gaussian to this noise peak and set an upper channel number limit at approximately three or four σ above this peak. An event whose signal falls below this channel number was considered to not have triggered D1.

In an idealized version of the detector stack, a 69.5-MeV should penetrate C, losing 49.7 MeV and penetrate D4, losing 9.6 MeV, pass through the stack with a final energy of 6.5 MeV. We noted that the amplification of C was changed by reducing the gain setting by 50%. This increases the maximum measurable energy from around 12 MeV to 23 MeV, yet we expect a 69.5-MeV proton to lose at least 50 MeV in C. This is confirmed by the saturated histogram from Figure 4-3, so this monoenergetic beam does not provide a calibration for C. It also appears that these protons do not reach D4, as the histogram resembled that of a noise peak from muon calibration.

In the energy-loss histograms for calibration with the 214.9-MeV monoenergetic proton beam (Figure 4-4), there is a measurable energy loss peak in C. The calibration spectra were limited to all events that penetrate the stack cleanly. This included events that did not saturate G1–G4 and S. Because we expected an energy loss of 14.7 MeV in C, C should also not saturate. There were also noticeably lower energy losses in D2 and D3 as expected, and a larger signal in D4. Upon closer inspection, before removing events involving saturation of other detectors (indicated in grey in Figure 4-4), there is a low-energy peak located below channel 200 centered at the same location in the D4 histogram as for 69.5-MeV protons. These are protons that penetrated a G detector and/or C without triggering D4, suggesting that the previous D4 calibration histogram also indicated that D4 was largely not triggered with the peak being due to noise.

An estimation of the conversion gain of C is 5.5 keV per channel, which was previously 2.8 keV per channel from muon calibration. This is consistent with reducing the amplifier gain by half. The peaks for D2 and D3 are reasonably consistent with the peaks for the 69.5-MeV proton beam. With two calibration points each, the conversion gain estimate is further refined, assuming linearity in the response. With only this one calibration point, a similar approach was taken in setting an upper channel limit that defines a trigger of D4. We know which peaks represents protons that penetrate D4 and which do not, with the trigger level seemingly located around channel 200. Estimating the conversion gain of D4 to be around 3 keV per channel, a minimum signal of 600 keV is required to produce a signal in D4, which explains why there was no signal produced by a muon, which only loses 388 keV, despite the noise being measured to be 75 keV.

With detector calibration, particle identification criteria unique to the experiment can be determined. The purpose of proton testing is to determine whether protons are identified as electrons and as positrons. First, this requires that D1 does not trigger. EGS4 simulations show that electrons lose 14 keV in D1 and would not exceed the 75-keV noise in D1. 214.9-MeV protons do not trigger D1 either, so the trigger requirement on D1 was based on a Gaussian fit of the noise peak (Figure 4-4).

To be detected, an electron also has to penetrate both D2 and D3, depositing a certain amount of energy in each. The signal must exceed the 45-keV noise intrinsic to D2 and D3, so the minimum detection trigger is set to three times the noise, which is 135 keV. Protons may be rejected by setting an upper limit for energy loss of electrons in D2 and D3, defining a detection threshold for electron

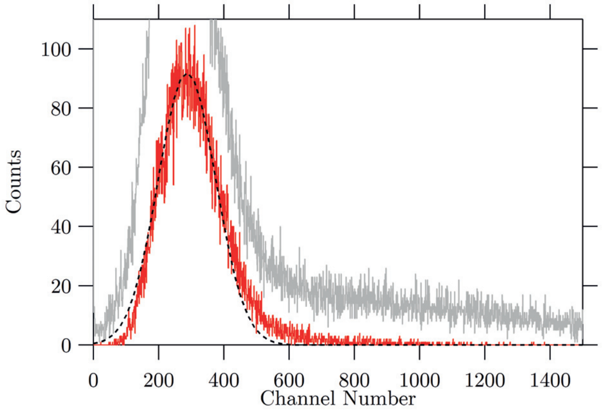

(a) D1 (40 keV; noise)

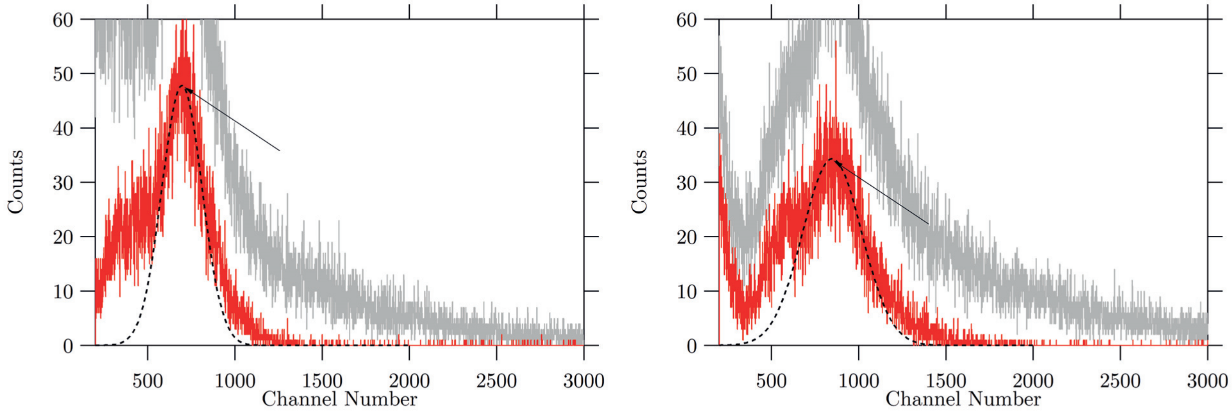

(b) D2 (0.798 MeV), 696.2 σ=114.9

(c) D3 (0.798 MeV), 847.6 σ=168.9

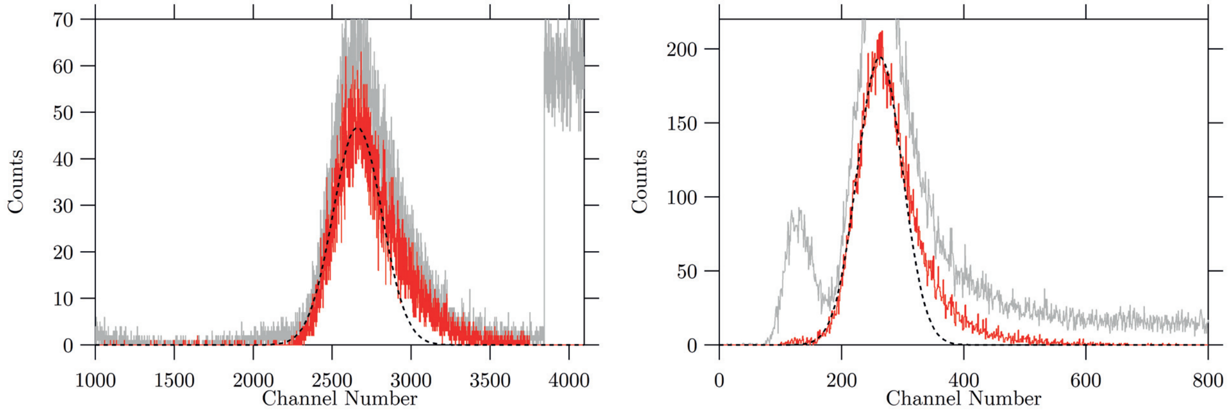

(d) C (14.7 MeV), 2659.2 σ=154.7

(e) D4 (0.826 MeV), 262.6 σ=37.0

Figure 4-4: Proton energy loss histograms with 214.9-MeV monoenergetic beam for detector calibration. The theoretical energy deposition is given, alongside the peak location and width of the Gaussian fits (dotted lines), in channels. This is the maximum energy at which the proton beam operates. Histograms in red represent all protons that cleanly penetrated the detector stack.

and positron identification.

At energies greater than 66.6 MeV, protons are expected to penetrate the entire detector stack, trigger D4, and thus be rejected for electron/positron identification. At this critical energy, the average energy loss of protons in D2 and D3 is 1.83 MeV (Table A.1). Ideally, the upper limit of the electron and positron detection threshold for D2 and D3 could be set around this 1.83-MeV signal, such that protons with energy less than 66.6 MeV, and do not penetrate the entire stack, would exceed this threshold be rejected by D2 and/or D3, while protons with energy greater than 66.6 MeV would be rejected by triggering D4. This would maximize electron and postron detection efficiency while maintaining minimal proton rejection.

Considering that according to EGS4 simulations, electrons (at MeV energies) on average lost 290 keV in D2 and D3, we conservatively opted to set the upper limit of the electron/positron detection threshold at 515 keV to ensure proton rejection, specific to this test. This value approximately lies in the middle between 290 keV and the 798 keV of energy loss by 214.9-MeV protons expected in D2 and D3.

A minimum and maximum required signal in C can also be set to further reject protons. From EGS4 simulations, electrons need to have an energy greater than 1.5 MeV to reach C, and at 8.5 MeV (and greater), electrons are more likely to penetrate C and trigger D4. The minimum energy loss in the C was set to be around $\sim$1.5 MeV. The maximum energy loss in C could be broadly set at 10 MeV.

The outlined identification criteria for D1–D3, C, and D4 are summarized with the detection thresholds and converted to corresponding channel ranges, using our calibrations, summarized in Table 4.4.

The anticoincidence shield S could not be calibrated due to its irregular shape, but a minimal requirement for particle detection is that it does not saturate, which indicates penetration by a particle. For D1 and D4, if a particle event exceeds these channel numbers, then the detector is

Table 4.4: Detection criteria for SSDs and C based on calibration with monoenergetic proton beams.

Detector	Signal Required	Channel Threshold
D1	—	<445
D2	135–515 keV	220–495
D3	135–515 keV	170–555
C	1.5–10 MeV	270–1820
D4	—	<225
S	—	<3840 (not saturated)

considered to trigger, rejecting the event from electron or positron identification. The channel range for C was based on the conversion gain approximation of 5.5 keV per channel. For D2 and D3, the channel numbers were calculated based on straight-line regression fits to the two calibration points for each detector, weighted by the width of the Gaussian fits.

Electron and positron identification criteria were determined from calibrating with monoenergetic proton beams. To complete the particle identification process, criteria for G1–G4 have to be set, based on calibration with another radioactive source.

4.5 G1–G4 Calibration

The inorganic crystal scintillation detectors G1–G4 were originally calibrated with ^{137}Cs, which is a gamma emitter of 0.662-MeV photons. The purpose of G1–G4 is to detect 0.511-MeV annihilation γ-ray photons. For on-site calibration purposes, a ^{22}Na source was provided. ^{22}Na is particularly useful because it undergoes β^+ decay, which results in emission of 0.511-MeV annihilation radiation. Additionally, ^{22}Na emits γ-rays at 1.274 MeV. Calibration at the experiment site ensures that we have the most current calibration, in case the environment (e.g. temperature) or transport of equipment alters detector or electronics characteristics.

The amplifier gain of each detector was targeted such that the 0.511-MeV signal is registered at around channel 1365, which is one-third of the VME crate's 4096-channel range. Amplifier settings were not altered from the previous calibration with ^{137}Cs, so we expected good consistency.

An identical calibration procedure applies. The coincidence module is set so that VME crate records data on a trigger of one selected G detector, with the source placed above the center of the instrument to attempt to distribute radiation evenly across all of the detectors. The spectra are not as clean at lower energies, so the peaks are again fitted to modified Gaussian curves of the form:

$$f(x) = y_0 + A \exp\left(\frac{(x - x_0)^2}{2\sigma^2}\right) + B \exp\left(-C(x - x_0)\right) \tag{4.1}$$

x_0 is the location of the peak and σ is the standard deviation, which is a measure of the characteristic width of the peak and its energy spread or resolution. The results are shown in Figure 4-5. In addition to the 0.511-MeV spectral peak, there seemed to be the appearance of a significantly broader peak which was presumed to be the 1.274-MeV gamma peak in the spectra for G1, G3, and G4. We also attempted to determine the location of these peaks mainly to check that they are consistent to the location of the 0.511-MeV peak.

We gauge the consistency of calibration by dividing the energy by the channel number of the peak's location to estimate the conversion gain for each detector. This conversion gain, the energy per channel, is multiplied by the channel number of the 1.274-MeV peak (when possible). The energies of the second peak of the spectra for G1, G3, and G4 were all calculated to be around 1.274 MeV, confirming that the location of their first peaks represents 0.511-MeV. The conversion gain of G2 was too low to record a 1.274-MeV signal (though the response seems to show a slight rise to a peak at what would be a higher channel).

The 0.511-MeV peaks were also compared to the 0.662-MeV peaks from the calibration with ^{137}Cs (Figure 3-12), the conversion gains do not match perfectly. They are reasonably consistent (within 15% at most), but for particle identification purposes, calibrations that occur close to the time of testing are preferred, as they are most representative of the experimental conditions at the time.

From these calibrations, we can determine the requirements on G1–G4 for electron and positron

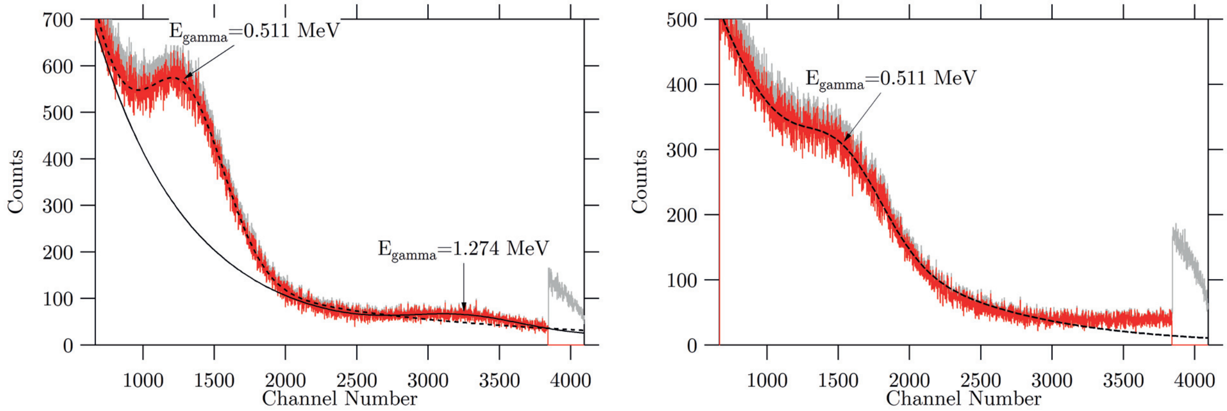

(a) G1, 0.511-MeV peak at 1269 ± 218

(b) G2, 0.511-MeV peak at 1537 ± 292

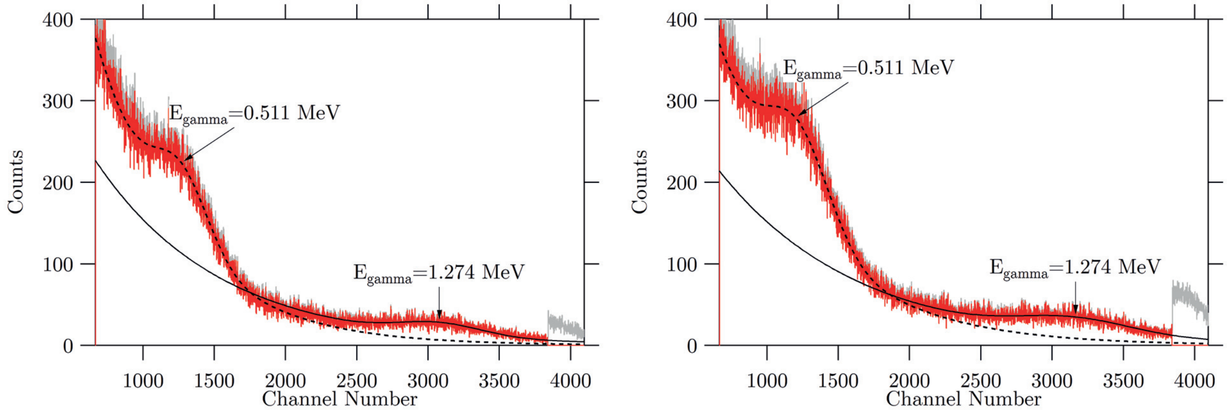

(c) G3, 0.511-MeV peak at 1266 ± 196

(d) G4, 0.511-MeV peak at 1215 ± 225

Figure 4-5: Gamma calibration spectra for G1–G4 with a ^{22}Na source. The 0.511-MeV annihilation peak is fitted with modified Gaussian peak (dotted line). The width of each peak consistently ranges from 15–20% of the value at each peak. When possible, an attempt was also made to fit what would seem to be a gamma peak at 1.274 MeV (solid line) and was only used to check if the location of the first peak was consistent with 0.511-MeV of energy.

identification. For positron identification, 0.511-MeV signals are required in exactly two G detectors, where a 0.511-MeV trigger was broadened to fall into threshold of 0.511 ± 0.100 MeV (or 0.411–0.611 MeV). The 0.1-MeV wide requirement was chosen because it was approximately 20% of 0.511-MeV which is around the characteristic energy broadening (∼one σ) of the G detectors. Note that this is significantly broader than the model response of a 25-keV threshold defined by the EGS4 Monte Carlo positron identification.

For electron identification, there is no signal in G1–G4 after stopping in C. This is not as simple as requiring the signal in each G detector to be zero, because there is energy pedestal of few hundred channels unique to each detector that the signal must exceed. When calibrating each individual detector, the VME crate only collects data on a trigger of that particular detector, so the spectra for the other three detectors should record no signal (with the exception of the unlikely case of cross-talk or accidentals). The pedestal is represented by a tall, narrow low-energy peak which can be fitted to a Gaussian. We then determined for each detector a channel number below which defines a non-trigger of that detector, at several σ past the peak. The final criteria for the G detectors are as follows:

Table 4.5: Criteria for a no signal and a 0.511-MeV signal in G1–G4 based on ^{22}Na calibration.

Detector	No Signal (<Channel Number)	0.511-MeV Signal (Channel Threshold)
G1	<375	1020–1520
G2	<465	1235–1840
G3	<285	1015–1515
G4	<235	975–1455

Each threshold is the range of channels representing the energy range of 0.411-0.611 MeV, based on respective conversion gain estimates calculated by the ratio of the peak energy of 0.511-MeV to the channel location of the peak.

The calibration of the detectors confirms the features identified in the energy loss histograms or gamma spectra. The values listed in Table 4.4 and Table 4.5 form the full set of identification criteria to be applied to the rest of the beam data. In the next section, the number of events identified as electrons and positrons are determined and tabulated.

4.6 Particle Identification And Results

Electron and positron identification is done by applying the cuts based on the criteria determined from the calibration process. Each event must satisfy a set of conditions, and the number of events that satisfy all of the conditions are counted. The results are presented in Table 4.6.

Table 4.6: Proton experiment results. The number of protons identified as electrons are counted. Positron identification was counted two different ways. The first is with two coinincident 0.511-MeV signals. The second way required either one or two 0.511-MeV signals in G detectors.

Beam Energy (MeV)	Beam Angle	No. Of Events	Identified As Electrons	Identified As Positrons	Identified As Positrons With A Single 0.511-MeV Signal
69.5 (monoenergetic)	0°	35226	2	0	0
69.5	0°	57555	4	0	0
	12°	51983	1	0	0
	45°	7793	0	0	0
	180°	9804	0	0	0
145.1	0°	132619	16	0	0
	12°	108251	3	0	0
	45°	14439	1	0	0
160.6	180°	135552	1	0	0
179.1	0°	144756	9	0	0
	12°	135274	4	5	7
	45°	12762	1	0	0
	180°	130459	1	0	1
214.9 (monoenergetic)	0°	70758	1	1	2
214.9	0°	245468	12	2	12
	12°	171347	11	2	4
	45°	15397	1	0	0
	180°	175504	8	1	7

Detection efficiency was originally calculated as a percentage of events identified out of the total incident particles in the theoretical model. The particles were emitted in a beam whose radius was smaller than the aperture, center bore of the model, and the radius of the SSDs. This ensured that the trajectory of the most of the particles followed the intended geometry of the instrument, triggering D2 and D3 before stopping in C. Experimentally, we implemented the coincidence requirement that both D2 and D3 must trigger. Each trigger was considered a particle event consistent with the geometry of the detector stack and counted under ”No. of Events” in Table 4.6 for identification. The number of events do not need to be readjusted for the total beam intensity or beam size as any particles out of geometry did not satisfy the D2 and D3 trigger requirement and/or would be already rejected by anticoincidence.

Two different positron counts were performed. Positron identification was first done by requiring the usual two coincident 0.511-MeV signals in exactly two different G detectors. Positron identification was also tested using the less stringent requirement of one 0.511-MeV signal. Of a total of over 1.6 million events, less than 0.01% of protons were misidentified as electrons and less than 0.001% of protons were misidentified as positrons.

The experiment at the Burr Proton Therapy Center’s accelerator facility verified the PICAP prototype’s basic functionality and demonstrated its ability to discriminate protons from negatrons and positrons. PICAP is ultimately expected to identify positrons. Because negatrons are identical in mass, there is a small probability that they are misidentified as positrons, as was shown in EGS4 simulations from the previous chapter.

Chapter 5

Electron Experiment at the Idaho Accelerator Center at Idaho State University

5.1 Overview

Following the successful experiment at the Burr Center, the next step was to expose the PICAP prototype to negatrons and positrons in the energy range for which the instrument was optimized. Previous Monte Carlo simulation data determined the energy range to be ∼2–10 MeV. The only option was the Idaho Accelerator Center, located at Idaho State University in Pocatello, Idaho (IAC/ISU). While a fair number of machines produce negatrons at these energies, no other facilities in the United States provide positrons at these moderate energies.

This accelerator experiment was performed on 9–10 December 2013 using the IAC's 44-MeV short-pulse electron LINAC (linear accelerator), capable of producing electrons with energies ranging from ∼2–44 MeV. The goal was to demonstrate the instrument's response to electrons of known charge sign and energy and determine whether the results were consistent with those of the EGS4 Monte Carlo simulation data.

Theoretically, the experimental procedure does not differ from the procedure during the proton accelerator experiment. Radioactive source and muon calibrations were obtained close to the time of the experiment at the accelerator site. This includes a muon calibration, primarily for the D2 and D3 solid-state detectors (SSDs) and C plastic scintillation detector, as well as calibration of the toroidal BGO crystal scintillation detectors, G1–G4, with a ^{22}Na source. The particle angles of incidence could be changed with a motorized rotation plate where the prototype is mounted at the end of the beam line in the beam vault. A trigger requirement was set for D2 and D3 for data acquisition. Where this experiment differed was in the beam structure and a number of environmental challenges.

Conditions surrounding the experiment ultimately proved to be less than ideal. The rate of particles per beam pulse was exceedingly high for the electronics. The electron beam was not well collimated. There was also the presence of a high γ-ray background in the vault when the beam was in operation. Despite shielding efforts, this contaminated the signals in G1–G4, which is problematic, since positron identification depends on the detection of 0.511-MeV photons from isolated negatron-positron annihilation events.

We attempted to analytically decouple contributions of signals due to this gamma background from those due to negatron-positron annihiliation. This required an alternate analysis approach and is detailed in the following chapter. For this chapter, the experimental arrangement and procedures are briefly described, including detector calibrations. Due to the challenges mentioned, electron and positron identification in the manner demonstrated in the proton experiment (Chapter 4) was not possible. We describe circumstances that arose from the nature of the beam operation and the methods employed to mitigate them.

5.2 Experimental Arrangement and Procedures

The 44-MeV LINAC operates at various currents depending on the electron energies requested. Beam energies were selected based on the energies at which the electron and positron detection

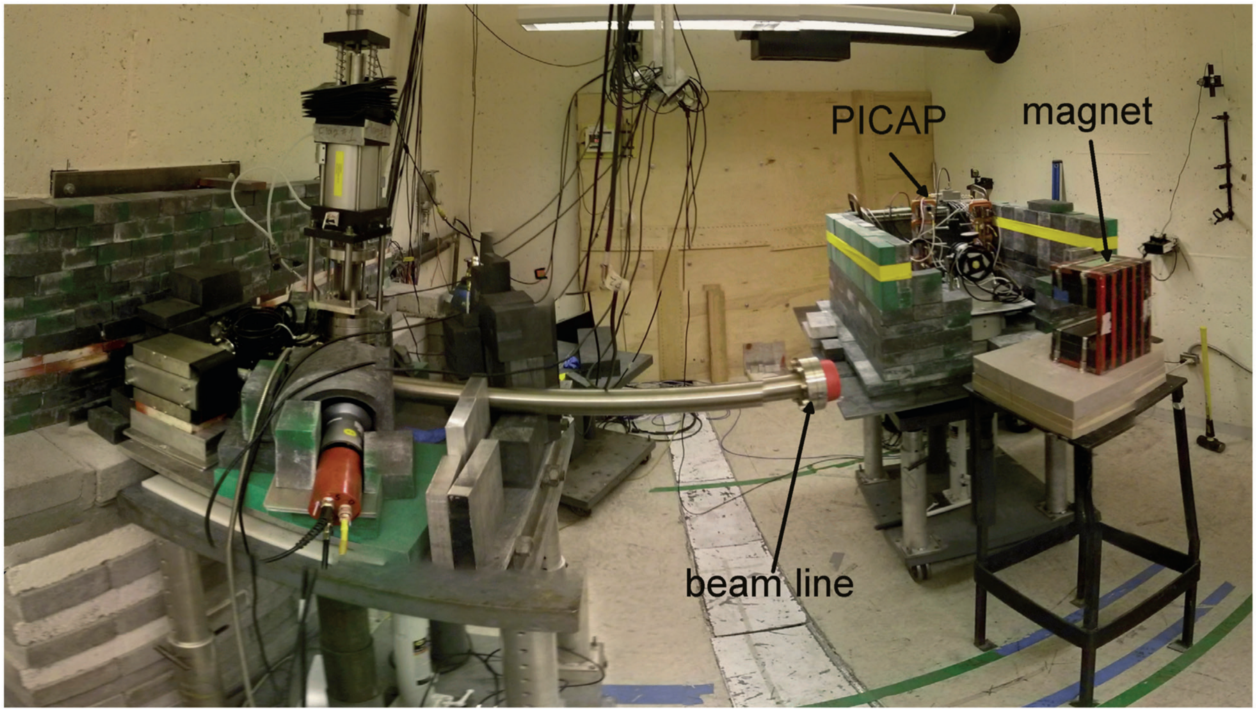

Figure 5-1: The beam vault taken with a fish-eye lens. The preamplifiers for each detector are attached to the prototype's custom aluminum mount. The mount sat atop a rotation plate. The entire setup was shielded with lead bricks to reduce gamma contamination. The permanent magnet in front of the instrument's aperture directs negatrons or positrons from the end of the beam line towards the instrument. Polarity was changed by physically rotating the magnet. The magnet stand was marked so that the physical re-alignment of the magnet did not otherwise alter the beam particle profile that entered the PICAP instrument. For perspective, the beam pipe and green lines on the floor are straight.

efficiencies were the greatest, based on EGS4 Monte Carlo simulations (see Figures 3-4 and 3-5). The aluminum beam energy degrader was not used during testing, so all beams are near monoenergetic.

The majority of beam trials were for 15 minutes. A few trials (4.5-MeV positrons and 5.4-MeV negatrons and positrons) were run approximately 20–45 minutes at a reduced beam intensity. The instrument rested on its custom aluminum mount which was attached to the turntable, where the rotation axis is about the top of the C detector (Figure 5-2).

12° is the maximum angle at which a particle traveling in a straight-line path penetrates D2 and the center of D3; however, this is a beam of particles of a finite spread. Furthermore, a magnet was placed at the end of the beam line to bend the trajectories of particles and guide them towards the aperture of the instrument, without any collimation. The magnet spread the beam of particles

Table 5.1: A summary of electron beam trials for this experiment, including the beam energy, charge sign and angles of incidence.

Beam Energy (MeV)	Negatron/Positron	Angles Of Incidence		
4.5	e^-	0°	12°	—
4.5	e^+	0°	—	—
5.4	e^-	0°	12°	35°
5.4	e^+	0°	12°	35°
5.8	e^-	0°	12°	35°
5.8	e^+	0°	12°	35°
6.8	e^-	0°	12°	35°
6.8	e^+	0°	12°	35°
8.8	e^-	0°	—	—
8.8	e^+	0°	—	—

out at the instrument.

Calibrations were primarily for D2, D3, C, and G1–G4. Amplifier gain settings were again manually adjusted for the purpose of this accelerator test. A ^{22}Na source provided 0.511-MeV annihilation photons for calibration of G1–G4. An overnight calibration with atmospheric muons was also performed on-site. The same arrangement of electronics (Figure 3-11) and data acquisition system was used, with the computer being remotedly operated.

5.3 Muon Calibration

As was the case with the initial tests of the prototype and the MGH proton experiment, the most reliable method of calibrating the C detector is by exposure to atmospheric muons. We know the amount of energy loss of muons in each detector from previous calibration (Table 3.4; Groom et al. [2001]). We ignored D1 and D4 since minimizing ionizing muons did not appear to give a measurable signal above the noise during previous calibrations. Muon data collection yields energy loss spectra for D2, D3, and C (Figure 5-3).

Each muon energy loss peak is fitted to a Gaussian curve. From calibration, an estimate of the conversion gain, or energy per histogram channel, can be calculated by taking the ratio of the peak energy and the peak channel number. For C, this is approximately 7 keV per channel. For

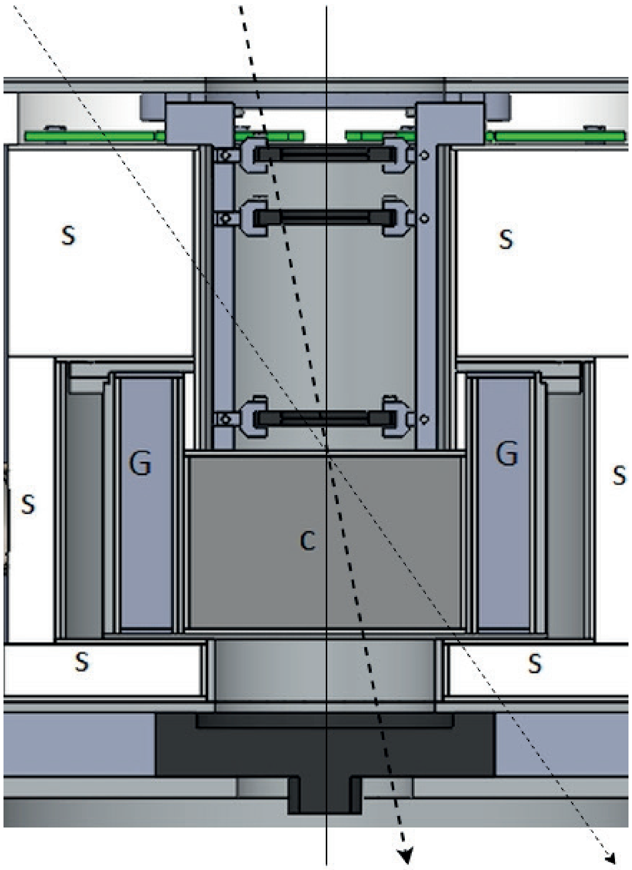

Figure 5-2: The PICAP prototype's rotation axis was centered at the top of C. The diagram illustrates electron trajectories incident at 12° and 35° (dotted lines). Assuming straight-line paths, 12° is the maximum angle at which a *single* particle penetrates D2 to the center of D3; however, the beam was not well collimated and electrons have a tendency to scatter, so they may still satisfying the trigger requirement of D2 and D3, even at more dramatic angles.

D2 and D3, the conversion gain is approximately 0.2 keV per channel. Note that these values are not the same as ones calculated for the proton experiment. Electronics settings were optimized for the detection of electrons and calibration on-site provides the most accurate metric of the settings used in the experiment.

The muon calibration was particularly important in determining electron and positron identification criteria for D2, D3, and C.

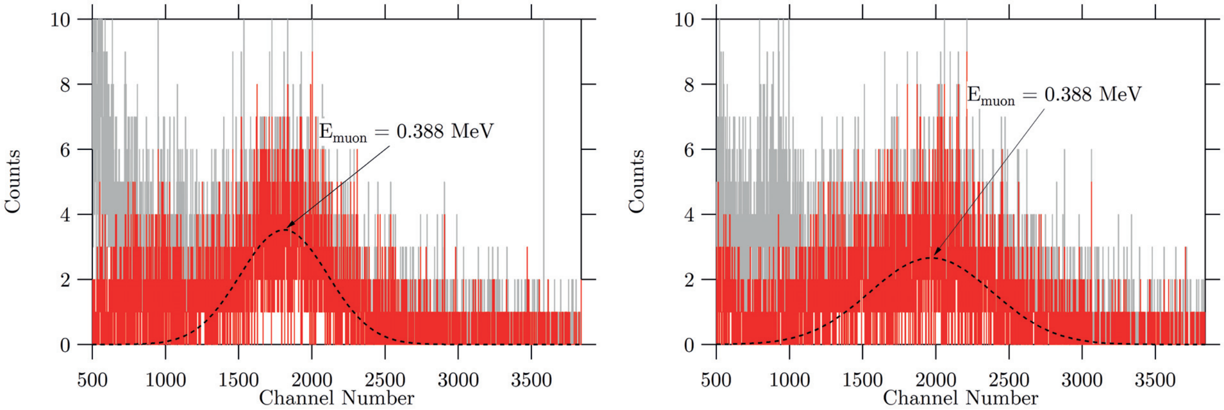

(a) D2, peak at 1809 σ=299

(b) D3, peak at 1967 σ=419

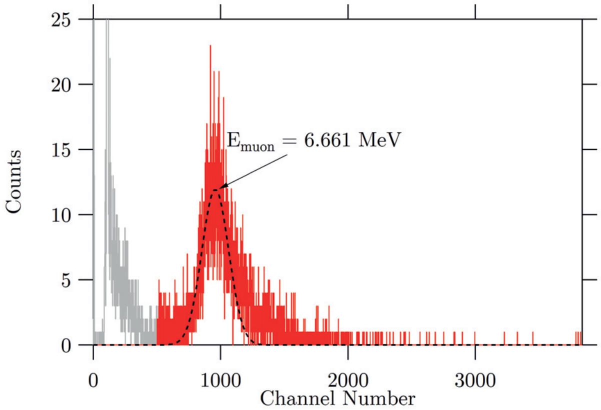

(c) C, peak at 957.5 σ=106

Figure 5-3: Muon calibration histograms of D2, D3, and C at the IAC/ISU. Raw data is colored grey. The subset of events within the muon energy loss peak in C are colored in red.

5.4 Addressing the Multi-Particle Beam Pulses

The issue of multiple electrons in C was initially recognized early on in experiment planning. The most suitable approach adopted for this accelerator run was to reduce the beam intensity for each trial. Some fraction of the electrons did not trigger D2 and D3, but some fraction of the pulses would result in events where one electron stopped in C, resulting in some usable data.

For the negatron and positron energies selected, ranging from 4–9 MeV, the 44-MeV short-pulse electron LINAC at the IAC/ISU operated at a current of ~1 A with a pulse width of tens of nanoseconds. Due to the nature of how particles were produced, the accelerator generated nanosecond pulses which often contained multiple negatrons or positrons per pulse, rather than a beam of particles being emitted one at a time. PICAP was designed for particle identification on an event-by-event basis. Our arrangement of NIM electronics are capable of processing signals with timing on the order of hundreds of nanoseconds at best. These speeds are typical of the electronics used for space-borne charged particle instruments similar to PICAP. The beam pulse time was thus much less than the temporal resoluiton of the linear electronics. It was impossible to resolve individual particles within a pulse temporally. Signals measured in detectors could result from not just one but multiple particles at any instance for a single pulse. This often saturates the detectors and the events are rejected just on that basis.

Upon reaching the beam vault, a magnet placed at the end of the beam line coarsely directed the particles towards the prototype instrument, effectively spreading the beam out without further collimation. By design, this was meant to fan out the multiple particles contained within each beam pulse. While this reduced the number of particles penetrating the detector stack, this also increased the number of detectors that were simultaneously penetrated off-center. The effect of the magnet ultimately rendered the anticoincidence elements S and D4 useless. Applying the broadest of identification criteria to these detectors often rejected the majority of events.

Electron and positron identification requires that a single particle is measured to have penetrated

D1–D3 before stopping in C. Rather than rely on anticoincidence, we first reduced the data by rejecting all events that saturate a G detector. The G detectors are set to measure 0.511-MeV signals from annihilation photons. If a few MeV electron were to enter and stop in a G detector, it would saturate the signal output. This creates an alternate anticoincidence requirement, which limits analysis to particles penetrating or stopping in C without further discarding events that also trigger the anticoincidence shield S. When pulses are fanned out by the magnet, a single negatron or positron in one pulse may penetrate the stack and stop in C while another particle(s) in that pulse may penetrate the shield simultaneously without interacting with G1–G4. In space, this event would be rejected, but here we keep events of this nature for analysis.

The anticoincidence requirement of G1–G4 not saturating often reduces the original data set by 70-80%. The remaining data includes single- and multiple-particle events, where these particles are all within the geometry. We attempt to select from the data for each beam trial, the subset of single-particle events in C, based on the distribution of residual energy loss in C. If there is sufficient data left after the initial G1–G4 cut, then there are evenly separated, discrete energy peaks in the C histograms (refer to Figures 5-4 and 5-5). The first peak was presumed to represent single particles stopping in C, which is fitted to a Gaussian with the form:

$$f(x) = f(x) = y_0 + A \exp\left(\frac{(x-x_0)^2}{2\sigma^2}\right) + B(x - x_0) \tag{5.1}$$

This is a Gaussian curve with a linear background, where x_0 is the location of the peak and σ is its characteristic width. The subsequent peaks, located at multiples of the energy of the first peak, represent multiple particles in a beam pulse stopping in C. The distribution is noticeably broader around the higher energy peaks, possibly due to variations in electron trajectory as a result of the particle spreading by the magnet and variations in the number of electrons from each beam pulse that successfully penetrate the stack and stop in C.

From the reisidual energy loss peak in C for single-particle events, a 2-σ cut was taken and apply to all of our data. This data selection process limited our further analysis to all the subset of events with an energy loss in C that falls within this range of channels. To further reject multi-particle events, we apply our electron detection requirements for D2 and D3. In order to reject protons, we have established an upper limit of 515 keV of energy deposition in D2 and D3. If two electrons were to penetrate D2 and D3 before stopping in C within the measurement timing, the signal measured would be around ∼600 keV and would also be rejected. Further analysis of our data was done exclusively with the subset events that satisfied this three-fold requirement (on C and D2/D3).

Using the muon calibration of C, we estimate the energy of the peak and determine if it is consistent with the expected residual energy loss of single electrons stopping in C. The muon calibration is also used to establish the electron detection thresholds for D2 and D3.

The muon calibration of C estimated a conversion gain of 7 keV per channel. We know from EGS4 simulations that negatrons and positrons lose on average of 600 keV before stopping in C. The residual energy loss measured in each single-particle peak for 4.5-MeV and 5.4-MeV negatrons and positrons is consistent with this energy loss of 600–900 keV before stopping in C, which appears to be reasonable considering the additional elements in the prototype not accounted for in the EGS4 model. With the subset of single particles stopping in C confirmed, a range of channels of this subset is selected and is the basis for the events considered for analysis and particle identification. We take this range to include channels within 2σ of the peak of the fitted curve.

We note, unfortunately, that this process was not possible for the majority of data collected during this experiment. In the case that most of the data is reduced, the trial is discarded from consideration. This includes trials when the angle of incidence was 35°, as well as every trial with 5.8-MeV positrons. In trials for both 5.8-MeV negatrons and both 6.8-MeV negatrons and positrons, applying the G1–G4 anticoincidence requirement did not reject every event; however, there were too few events for the C histograms to exhibit peaks, and single-particle events could not be selected. Some data was useable for determining identification criteria of D2 and D3.

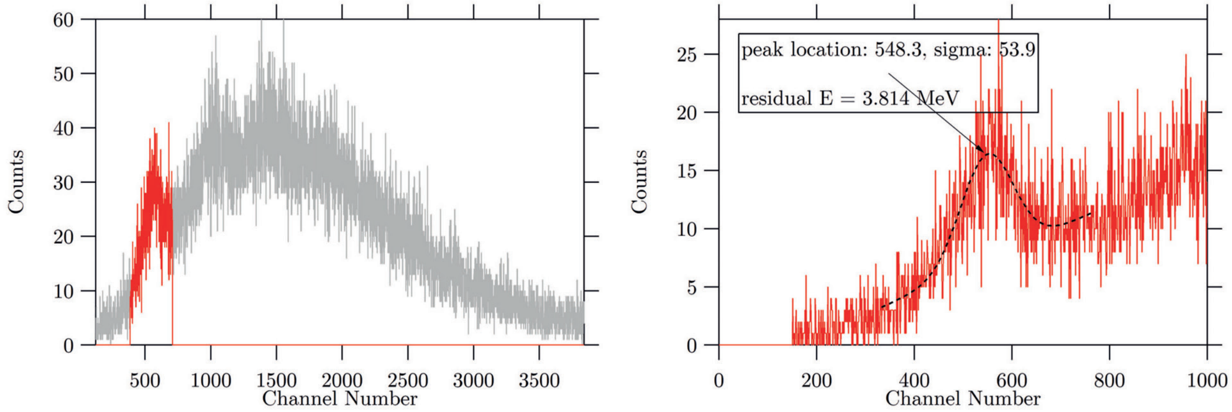

(a) 4.5-MeV negatrons

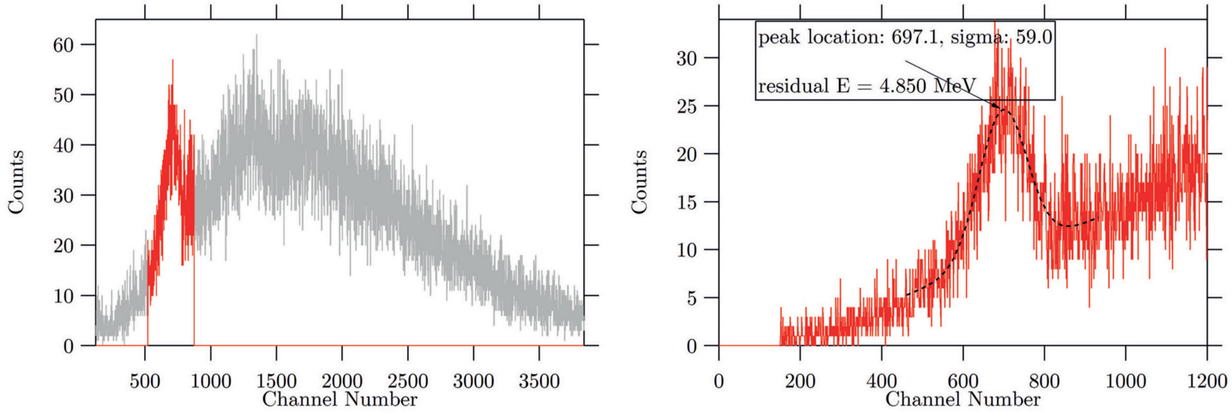

(b) 5.4-MeV negatrons

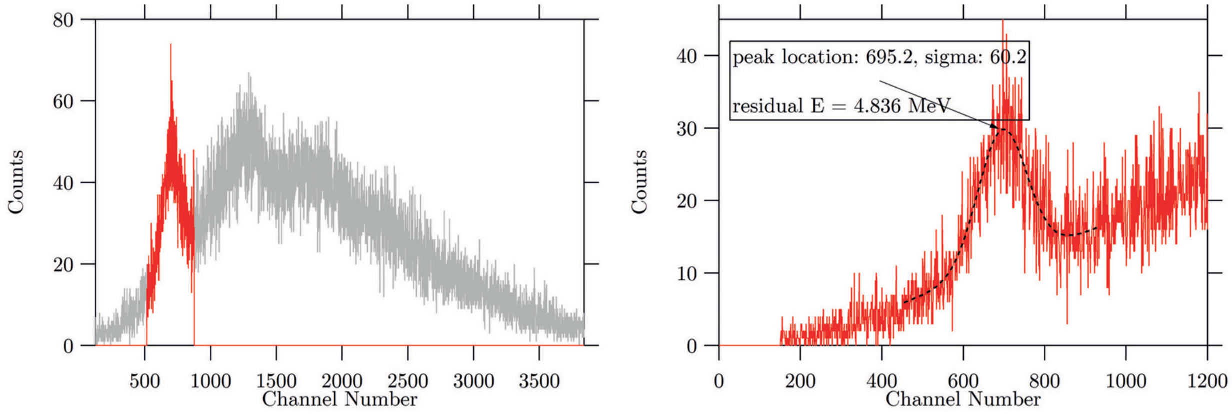

(c) 5.4-MeV negatrons, 12° incidence

Figure 5-4: Energy deposition histograms of negatrons in C. The left-side plots represent the raw data and the subset of data presumed to be representative of single negatrons stopping in C. The right-side plots show the fitting of events in that subset to a modified Gaussian curve. The energy was determined using the muon calibration, consistent with expected residual energy loss in C. Two negatron peaks can be seen for all beam energies.

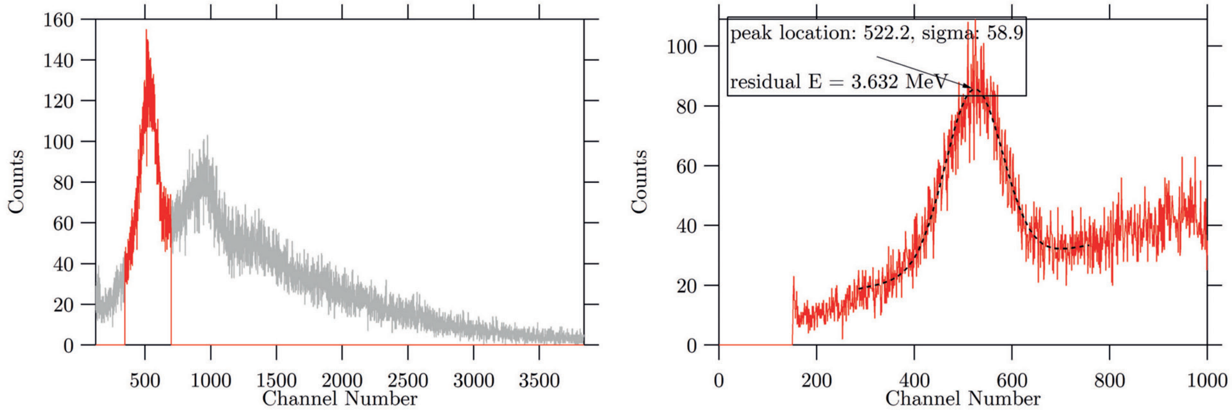

(a) 4.5-MeV positrons

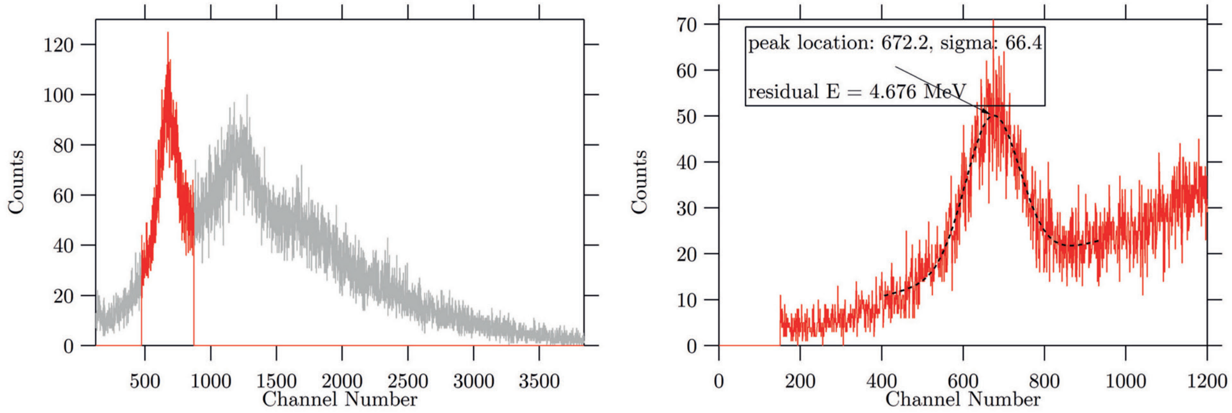

(b) 5.4-MeV positrons

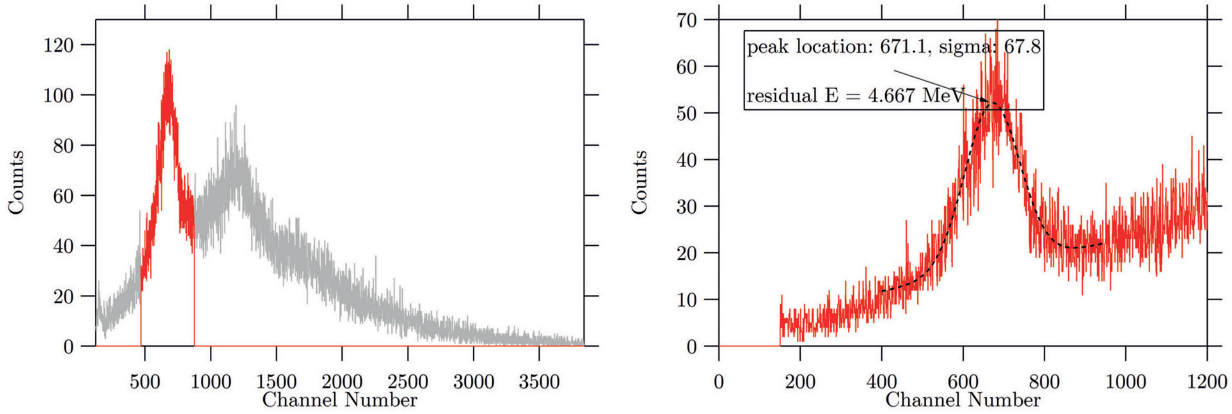

(c) 5.4-MeV positrons, 12° incidence

Figure 5-5: Energy deposition histograms of positrons in C. The left-side plots represent the raw data and the subset of data presumed to be representative of single positrons stopping in C. The right-side plots show the fitting of events in that subset to a modified Gaussian curve. The energy was again determined using the muon calibration, consistent with expected residual energy loss in C. Two positron peaks are clearly evident for all energies.

Atmospheric muons register a 388-keV energy loss signal in D2 and D3. This is similar to the energy loss expected for penetrating electrons, which is ∼270–310 keV. We have previously stated, for interpreting the proton experiment data, setting the lower limit of the the threshold to 135 keV, which is three times the intrinsic noise of the D2 and D3. The upper limit was set at 515 keV, which is five times the noise above the most probable electron energy loss of 290 keV in D2 and D3. From the muon calibration, we can determine single particle particle identification: The channel thresholds are consistent with histograms of D2 and D3 (Figures 5-6 and 5-7) corresponding to the single-particle events selected from the C histograms. Some of the beam trials can be used to confirm the validity of these channel thresholds for D2 and D3 (additional plots shown in Figures A-2 and A-1), despite it not being possible to select single-particle events with C histograms.

Table 5.2: Detection criteria for SSDs based on calibration with atmospheric muons.

Detector	Signal Required	Channel Threshold
D2	135–515 keV	630–2400
D3	135–515 keV	685–2610

5.5 Calibration of G1–G4 With ^{22}Na Source

The G1–G4 BGO scintillation detectors were calibrated with a ^{22}Na source, emitting 0.511-MeV γ-rays. As in previous cases to calibrate each detector, the stack is set to trigger on a signal from that individual G detector when exposed to the source for a set interval of time, typically five minutes. Because of gamma background considerations, we supplemented the standard calibration tests with five-minute trials of each detector triggering in the experimental vault without the presence of a source. This process had been notably neglected in previous testing, particularly in the MGH proton experiment. While it was originally done as a precaution to mitigate any gamma background concerns specific to this experiment, it would improve the G detector calibration by a process of reducing the intial ^{22}Na gamma spectra in the G detectors (e.g. Figure 5-8).

Reducing the spectra means effectively subtracting any background contributions from the

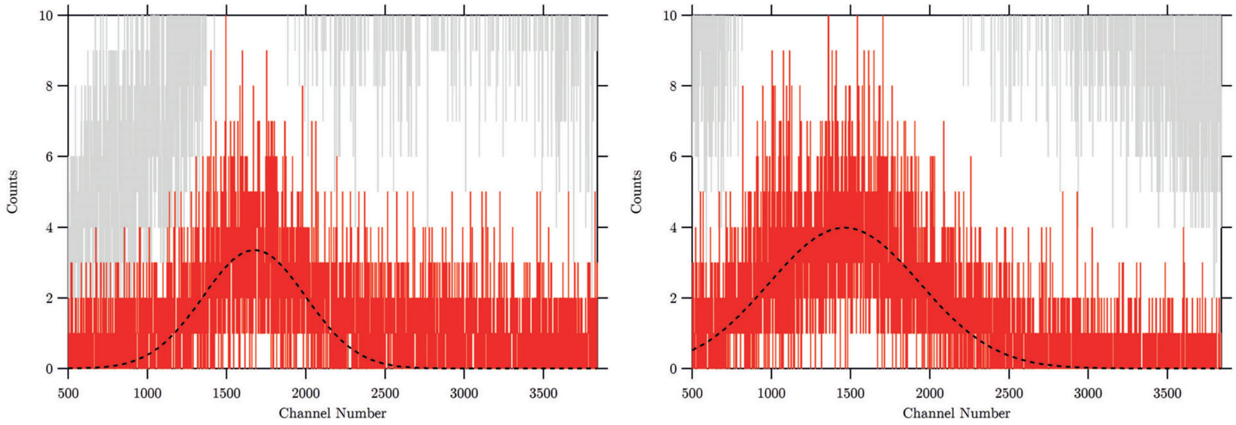

(a) D2, 4.5-MeV negatrons

(b) D3, 4.5-MeV negatrons

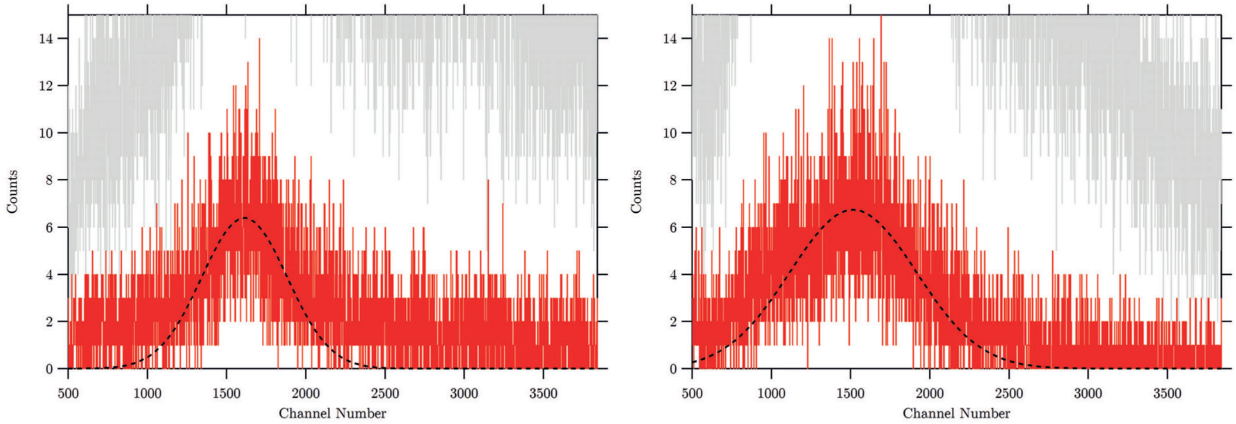

(c) D2, 5.4-MeV negatrons

(d) D3, 5.4-MeV negatrons

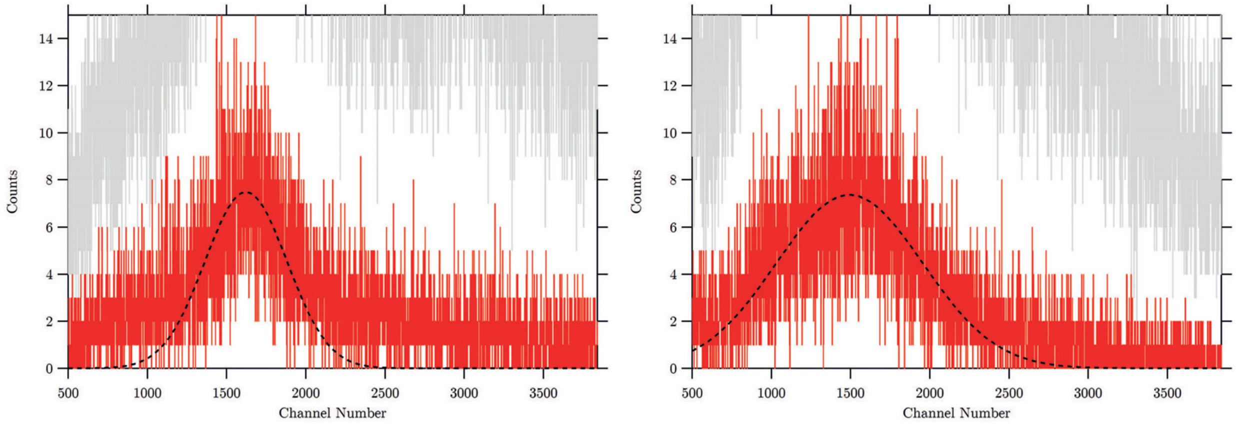

(e) D2, 5.4-MeV negatrons, 12° incidence

(f) D3, 5.4-MeV negatrons, 12° incidence

Figure 5-6: Energy depostion histograms of negatrons in D2 and D3 (selected for single negatrons stopping in C).

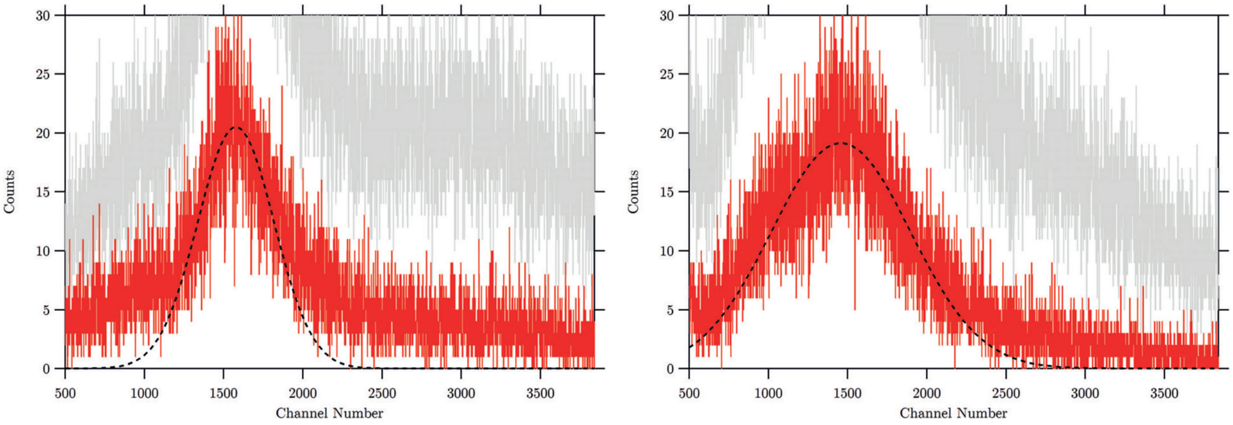

(a) D2, 4.5-MeV positrons (b) D3, 4.5-MeV positrons

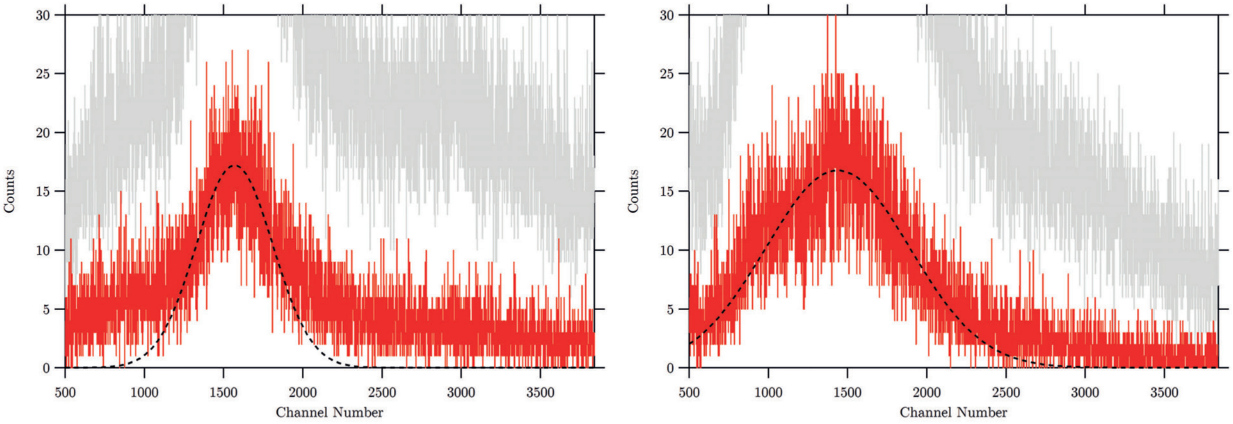

(c) D2, 5.4-MeV positrons (d) D3, 5.4-MeV positrons

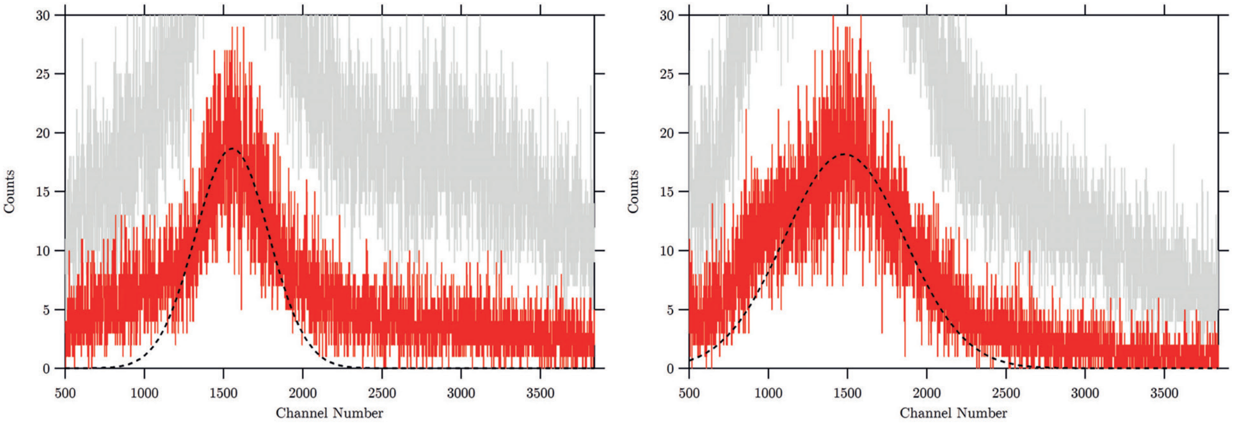

(e) D2, 5.4-MeV positrons, 12° incidence (f) D3, 5.4-MeV positrons, 12° incidence

Figure 5-7: Energy deposition histograms of positrons in D2 and D3 (selected for single negatrons stopping in C).

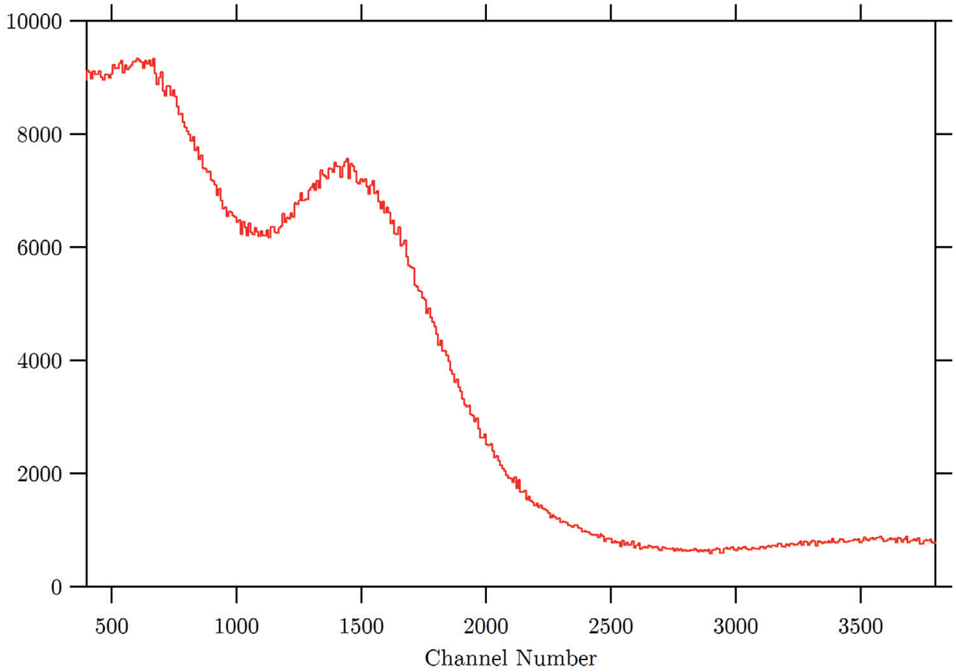

Figure 5-8: Typical ^{22}Na γ-ray spectrum in a G detector. This is the spectrum of the 0.511-MeV photopeak for G1.

signal due to the source. Data acquisition by the VME crate only occurs when the trigger logic, as set by the universal coincidence modules, is satisfied. A manually adjusted lower discriminator sets the minimum signal required for each detector channel to trigger. The instrument will not trigger as frequently in an interval of time in the absence of a gamma-emitting source, compared to when a source is placed nearby. A time interval of five minutes was used for data collection both with and without the source.

The spectrum taken without the ^{22}Na source can be subtracted from the initial gamma spectrum with the source (subtracting one histogram from the other, as shown in Figure 5-9). The resultant histogram (Figure 5-10) resembles those from previous calibrations to which we fit to a modified Gaussian $f(x)$ of the form:

$$f(x) = y_0 + A\exp\left(\frac{(x-x_0)^2}{2\sigma^2}\right) + B\exp\left(-C(x-x_0)\right) \tag{5.2}$$

This is simply the sum of a Gaussian and an expontential function where x_0 is the location of

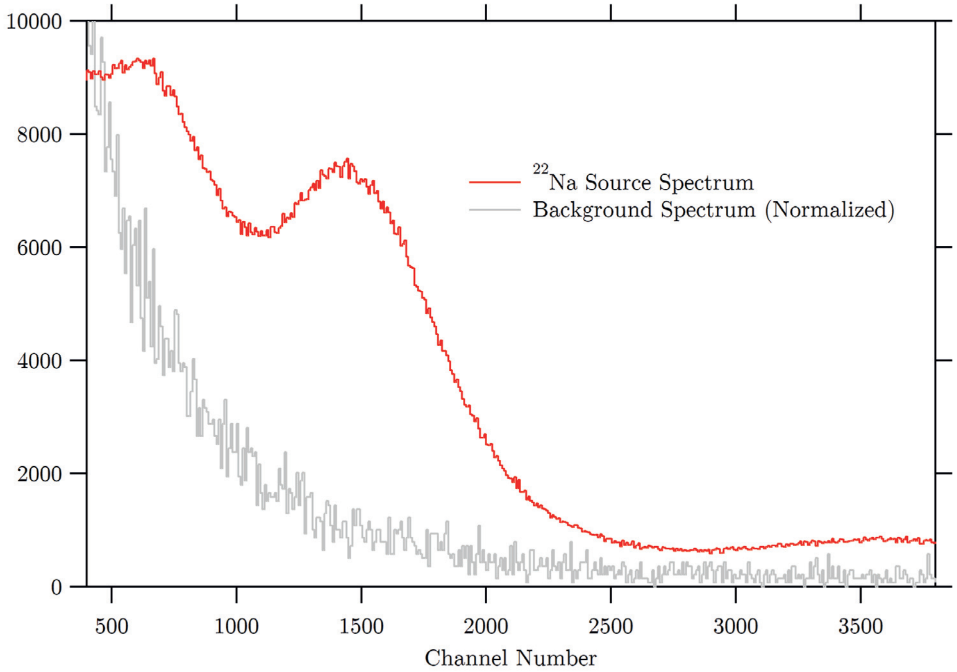

Figure 5-9: ^{22}Na γ-ray spectrum in a G detector (G1 shown). The second spectrum shown (in grey) was obtained by letting the detector trigger in the absence of the ^{22}Na, normalized to the same five-minute duration of data collection. This background spectrum is then subtracted from the source spectrum.

the peak and σ is the characteristic width of the peak, representing the standard deviation of the distribution. The other fitting parameters are A, B, C, and y_0.

Table 5.3: Criteria for a 0.511-MeV (± 100 keV) trigger in G1–G4 based on ^{22}Na calibration. These trigger thresholds will eventually be used for analysis in the next chapter.

Detector	0.511-MeV Signal (Channel Threshold)
G1	1210–1795
G2	965–1420
G3	1115–1635
G4	1065–1580

The presence of a gamma background contaminated and convuluted signals in G1–G4. The saturation of G detectors by the spread and fanning out of multiple-particle pulses had already severely limited the amount of data available. The remaining events contained contributions to these detectors from both the gamma background and annihilation produced from positrons stopping in C. Applying usual identification criteria for G1–G4 (based on the 0.511-MeV detection thresholds

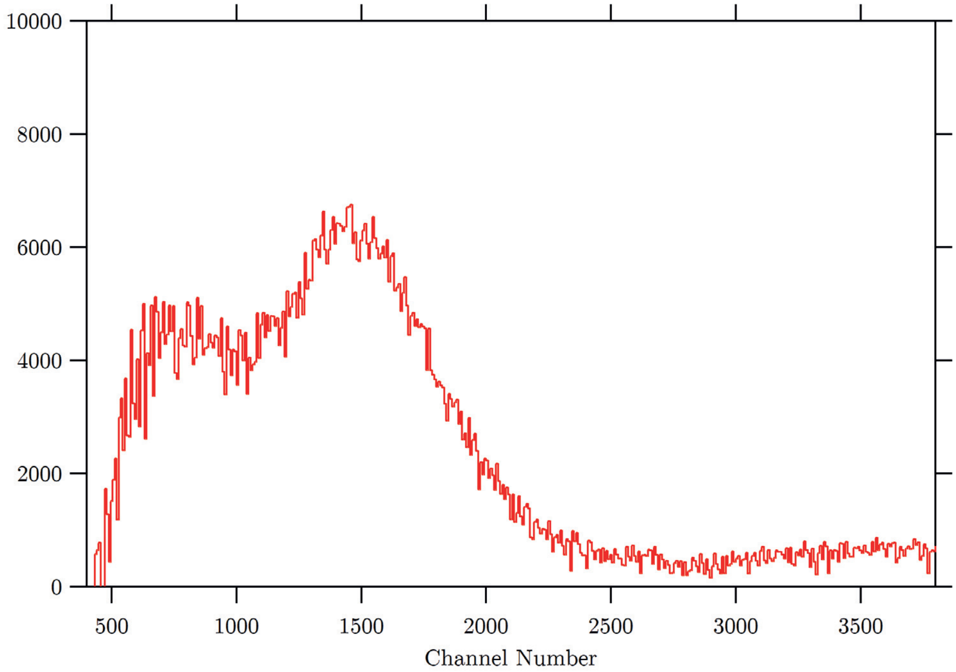

Figure 5-10: "Reduced" ^{22}Na γ-ray spectrum for G1 detector from subtracting the two histograms from Figure 5-9.

listed in Table 5.3) subsequently rejected the remaining data from electron identification, yet we did not believe that the detection rate would be severely low.

The goal of measuring negatron and positron response of the PICAP prototype instrument on an event-by-event basis was not directly met due to the challenges presented by the experimental environment; however, steps were taken in order to mitigate these challenges and calibrate the instrument to demonstrate functionality. The process of electron and positron identification requires, at mininum, that there be a single particle stopped in the C detector. This experiment presented the complication of a beam that frequently exposed the prototype to more particles than each detector's electronics could resolve temporally. This is especially apparent in the energy deposition spectra in the C detector for each trial, which reveal multiple discrete peaks separated by approximately the same amount of energy.

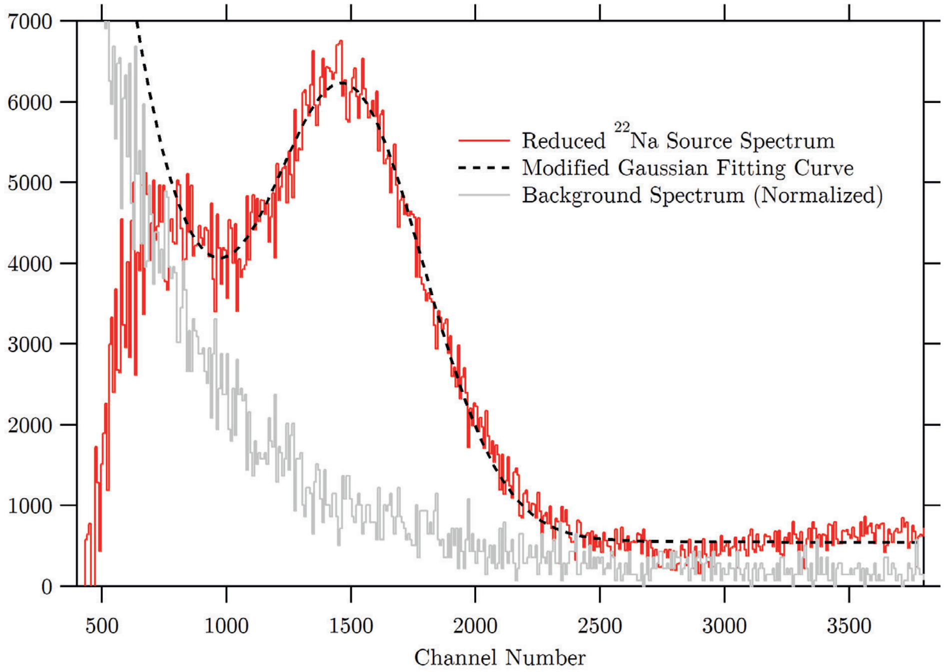

Figure 5-11: The “reduced” gamma spectrum with a modified Gaussian fitting curve (of the form in Equation 5.2). The location of the peak of the Gaussian (fitting parameter x_0) corresponds to 0.511 MeV of energy. G1–G4 were all calibrated in the manner for the purpose of this experiment.

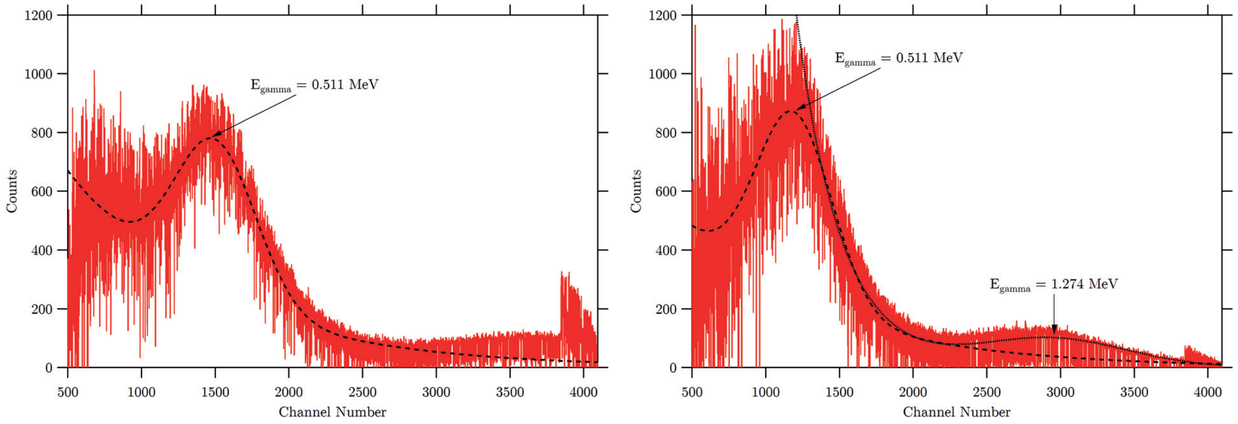

(a) G1, 0.511-MeV peak at 1502.6 ± 276.8

(b) G2, 0.511-MeV peak at 1192.3 ± 256.6

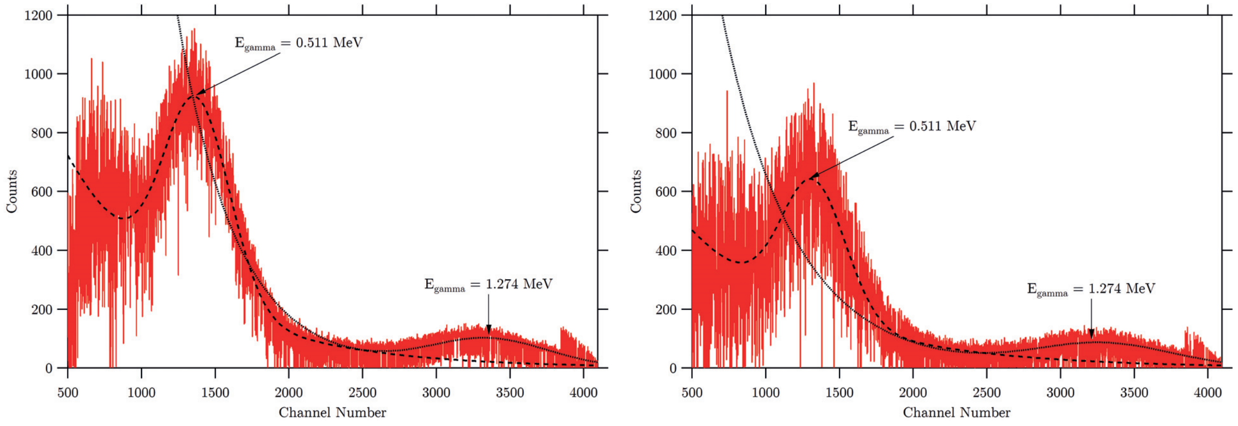

(c) G3, 0.511-MeV peak at 1375.2 ± 222.8

(d) G4, 0.511-MeV peak at 1324.6 ± 217.7

Figure 5-12: Gamma calibration spectra for G1–G4 with a ^{22}Na source. The 0.511-MeV annihilation peak is fitted with modified Gaussian peak (dotted line). The width of each peak consistently ranges from 15–20% of the value at each peak. When possible, an attempt was also made to fit what would seem to be a gamma peak at 1.274 MeV and was only used to check if the location of the first peak was consistent with 0.511-MeV of energy.

Chapter 6

ISU/IAC Electron Experimental Data: Maximum Likelihood Method

6.1 Circumstances Of Additional Analysis

On 9-10 December 2013, the PICAP prototype instrument was exposed to energetic negatron and positrons at Idaho State University's Idaho Accelerator Center (ISU/IAC), supplied by the facility's 44-MeV Short-Pulse Electron LINAC. The purpose of the experiment was to measure the prototype instrument's ability to identify electrons and positrons at multiple energies in PICAP's energy range of interest (∼2-10 MeV), in order to compare them to the baseline electron and positron responses established by EGS4 Monte Carlo simulations. The experiment posed challenges addressed in the previous chapter.

Preliminary analyses on the ISU/IAC experiment introduced the complication of the beam's multi-particle pulses, generated by the accelerator. The beam emitted pulses containing more than one negatron or positron (depending on the operation mode) at ∼nanosecond frequencies. The electronics used for signal processing were too slow (∼microseconds) to resolve particles in a pulse or even the length of the pulse. This is problematic as PICAP is intended to identify electrons and positrons on a single particle-by-particle basis. While this is possible in space, it was not feasible with the IAC data. To mitigate this issue, the moveable magnet oriented at the end beam line guided particles entering the experimental vault towards the aperture of the instrument in a spread out manner, as opposed to a collimated beam. The additional approach to dealing with this issue was to adjust the beam intensity, reducing it such that the rate of instances where multiple electrons stopped in C decreased.

Spreading out the particles in each pulse caused the anticoincidence shield S to trigger on nearly every event of every beam trial, rendering it useless for the experiment. Multiple particles often penetrated the detector stack despite spreading efforts, yet we were able to limit analysis to single particles stopping in C by taking narrow cuts centered about discrete residual energy loss peaks in the histograms of C, and confirming the validity of these cuts with their expected energy loss in D2 and D3. The energy loss at these peaks were confirmed with muon calibration and Monte Carlo data. Having to take small subsets of single-particle data severely limited the number of events for analysis. While adjusting the beam intensity reduced the number of events where multiple particles stopped in C, this also reduces the amount of useable data that can be collected during a trial of comparable duration. Furthermore, there was a non-trivial presence of background γ-rays produced as a byproduct of accelerator operation.

As we were warned in advance of this gamma-ray background, preliminary testing was performed by setting for the prototype instrument to trigger when exceeding a lower discriminator set for only G3, while the beam was in operation (generating 5.8-MeV positrons) but without particles entering the vault. Shielding efforts were made by stacking lead bricks along one wall of the vault. The prototype instrument and its mount/rotation plate were also surrounded by lead bricks only leaving the top and aperture side exposed. The number of triggers were then counted in five-minute intervals, with the beam powered on but stopped at the end of the line.

This testing revealed 38000, 43000, and 64000 random triggers of G3 in each five-minute interval, due to the background environment. This averages to hundreds of triggers per second, and unfortunately, most occur inside the nanosecond pulse window when the electrons enter the instrument, worsening this effect. The gamma background is problematic because PICAP electron identification requires that there be no signal in G1–G4 (for negatrons) and positron identification requires two coincident 0.511-MeV signals in two of the G detectors. Particle identification on an event-by-event basis is nearly impossible when there is a large accidental contribution of gammas to the G1–G4 detector channels; therefore, we were unable to directly measure a detection efficiency on an event-by-event basis from the data of the experiment.

The data contains unknown contribution levels of gamma interactions, originating from background accidentals and positron annihilation from within the detector stack. To determine how the instrument performed, we considered these two sources of gammas as unknown parameters in a statistical model that we assume governs the events counted experimentally. By applying a *maximum likelihood* method, we statistically estimated the parameters that maximize the probability of our observations. This chapter details this process and then applies it to the usable ISU/IAC data as well as similarly sized Monte Carlo data sets for comparison.

6.2 Maximum Likelihood Method

It might at first seem possible to use Monte Carlo simulation to model the beam and beam vault in addition to the instrument to determine the probabilties of γ-ray interaction with the PICAP prototype instrument. This would require prior knowledge of the initial conditions in the room, i.e. the location, velocity, and energy of all scattering electrons, as well as those traversing the instrument detector stack, as well as the location, velocity, and energy of all of the γ-rays inside the vault. Additionally, the position and material composition of all physical structures in the vault would need to be included. None of this required information (or any reasonable assumption to describe particle distributions) was available. The notion of modeling the instrument performance at the ISU/IAC was not realistically feasible.

The decision was made to determine whether the instrument output could be instead be modeled as an assumed input, with several unknown statistical probabilities describing how that instrument response occured. For instance, if we took an observed result where a G detector showed a 0.511-MeV signal, then either one of two things occurred to cause that response, an annihilation photon or an ambient γ-ray from the vault, ignoring all other possible sources for that instrument response. Now if we define parameters, G_p and G_b as probabilities for these two processes, respectively, then it should be possible to use a maximum likelihood analysis technique to determine the best-fit values of G_p and G_b, along with a similar analysis of the original Monte Carlo data with which to compare the instrument response.

A maximum likelihood analysis method is used when there is an observed result but the parameters of some statistical process that produced the data are unknown. The ISU/IAC data contains events with different combinations of triggers of G1–G4, yet it is largely unknown what portion of the triggers is due to the gamma background and what portion is due to positron annihilation (within the instrument; here we consider annihilation photons produced by positrons out of geometry, e.g. in the vault walls, as part of the background). For negatron beam trials, the expectation is that there should be little to no gamma contribution from annihilation photons. By contrast, for positron beam trials, we expect an increased contribution of gammas from annihilation of positrons stopping in the detector stack. By assuming an idealized statistical model that produced the experimental data, which is a probability distribution that is a function of the unknown parameters, we determine the set of parameters that maximizes the probability or likelihood of having made the observed measurements.

The statistics of the PICAP system are governed by the Poisson distribution. Whether it be analysis of Monte Carlo simulations or analysis of the performance of the prototype instrument, interpretation of the data depends on counting the number of independent events or triggers that satisfy the criteria set for a specific situation in any interval of time. In Chapter 3, Section 3.4, we introduced the idea of detection efficiencies of the PICAP scheme as a measure of an expectation value of particles identified, be it a positron or electron. The probability of counting a certain number of events in the Poisson distribution is:

$$P(k) = \frac{\lambda^k e^{-\lambda}}{k!} \tag{6.1}$$

P is the probability of k events occuring in an interval of time where λ is the average number of such events occuring in that interval of time. The Poisson distribution is a measure of the probability of observing a number of certain events, rather than the probability of that event occuring. We apply this to counting events in PICAP. P is the probability over the course of a beam run that a certain number of positrons are identified, where λ is the average or expected number of positrons to be identified from the beam run. The λ here is directly related to the probability that a particle is identified as a positron.

We could simply try to determine the parameters that maximize the Poisson probability (Equation 6.1) for some given observed data; however, large values of k may prove to be a computational challenge, so we define the likelihood function, $\mathcal{L}$, as the natural logarithm of the probability distribution P and by Stirling's approximation:

$$\mathcal{L} = \ln P = \ln \frac{\lambda^k e^{-\lambda}}{k!} = k \ln \lambda - \lambda - \ln k! \approx k \ln \lambda - \lambda - k \ln k + k \tag{6.2}$$

k is based on observed experimental data, but we do not know λ, which represents the detection rate or probability that we were trying to measure. The Poisson distribution governs the probability of counting a certain number of events. λ is the average event count based on the probability of the event occuring χ, such that $\lambda = \chi k_{\text{total}}$, where k_{total} is the total number of events.

Our statistical model is a set of probabilities represented by χ, which are functions of our unknown parameters, which we have defined above as G_b and G_p. In the next section, we first treat contributions from the gamma background and from annihilation photons separately and treat them as completely independent processes. We then combine the two processes to form a model that we assume describes the gamma triggers in G1–G4 that we observe from the ISU/IAC experiment. The parameters are then varied iteratively, calculating the probabilities and likelihoods after each change. Ultimately, a parameter space is mapped. The most likely parametric values are the values of G_b and G_p that maximize the likelihood. We will refer to gammas due to the gamma background as "background-gammas" and γ-ray photons emitted by positron annihilation as "positron-gammas."

6.3 Maximum Likelihood Method: Statistical Model

For each negatron or positron event, there are five possible outcomes of how many G detectors can be triggered by a 0.511-MeV signal. Zero, one, two, three, or all four of the detectors may register a signal. Each outcome can be further separated into sixteen specific cases (separated by semicolon):

Table 6.1: Possible 0.511-MeV Gamma Trigger Combinations of G1–G4

No. of G Detectors Triggered	No. of Cases	Possible Cases (Triggered Detectors)
0	1	none
1	4	G1; G2; G3; G4
2	6	G1/G2; G1/G3; G1/G4; G2/G3; G2/G4; G3/G4
3	4	G2/G3/G4; G1/G3/G4; G1/G2/G4; G1/G2/G3
4	1	G1/G2/G3/G4

Each case is defined by a unique combination of G detectors that are triggered. There is a likelihood associated with each outcome, which we will call $\mathcal{L}_0$, $\mathcal{L}_1$, $\mathcal{L}_2$, $\mathcal{L}_3$, and $\mathcal{L}_4$, the index indiciating the number of G detectors triggered. Each one of these likelihoods can be expanded as the sum of the likelihoods of each of the sixteen individual case listed in Table 6.1. For the ith case,

$$\mathcal{L}_i = k_i \ln \lambda_i - \lambda_i - \ln k_i! \tag{6.3}$$

k_i is the number of events in the experimental data that satisfies the ith case. For example,

$k_2^{(1,2)} = 44$ would mean that in 44 of the events, two G detectors were triggered by 0.511-MeV signals, specifially G1 and G2. While k_i is the observed count, λ_i is the expectation value for that number, or

$$\lambda_i = \chi_i k_{\text{total}} \tag{6.4}$$

where χ_i is the probability of the ith case occurring and k_{total} is simply the total events of an interval of time, such as over the course of a beam trial. Of k_{total} events with a probability of χ_i of the ith case, we expect λ_i events to occur.

χ_i is a function of every combination of probabilities for each case in Table 6.1. Now we define $P_b(i, G_b)$ and $P_p(i, G_p)$ as separate probabilites that i G detectors are triggered by a background-gamma or positron-gamma, respectively. G_b is the probability of a single background-gamma triggering a G detector, and G_p is the probability of a positron-gamma emitted from an annihilated positron triggering one of the G detectors from within the prototype instrument. For each beam run with viable data, these are the parameters whose value we estimate via the maximum likelihood.

The statistical model is meant to be an idealized probability. We first assumed that the γ-ray background is isotropic and interacts with G1–G4 each with the same probability. The first parameter we defined in the maximum likelihood method is called G_b, which is the probability that a background-gamma causes a 0.511-MeV trigger in a G detector. The probability that a background-gamma does not trigger a G detector is then $(1 - G_b)$. The overall background-gamma interaction just follows a simple binomial distribution. $P_b(n)$ is the probabilty of background-gammas triggering up to n unique G detectors. We have four G detectors, G1–G4, with five different cases ($n = 0, 1, 2, 3, 4$) ranging from none of the G detectors triggering due to the background to all four simultaneously triggering due to background:

$$\begin{aligned}
P_b(0) &= 1G_b^0(1-G_b)^4 &&= (1-G_b)^4 && (6.5)\\
P_b(1) &= 4G_b^1(1-G_b)^3 &&= 4G_b(1-G_b)^3 && (6.6)\\
P_b(2) &= 6G_b^2(1-G_b)^2 &&= 6G_b^2(1-G_b)^2 && (6.7)\\
P_b(3) &= 4G_b^3(1-G_b)^1 &&= 4G_b^3(1-G_b) && (6.8)\\
P_b(4) &= 1G_b^4(1-G_b)^0 &&= G_b^4 && (6.9)
\end{aligned}$$

The probabilities sum up to 1 and do not require normalization. Each probability can be divided by the number of possible combinations, listed in Table 6.1, to determine the probability per specific case.

We discovered that there were more gamma triggers in G1 and G2. If we refer back to the experimental arrangement and recall the lead shielding, the prototype instrument rests on its mount, G1 and G2 is oriented on the upward half and G3 and G4 are in the downward half (Figure 6-1). Lead bricks provided background shielding to the sides of the prototype instrument but left the top of the instrument unshielded. This was responsible for G1 and G2 experiencing a higher number of triggers compared to G3 and G4; therefore, we adjusted the probabilities by weighing the G_b parameter for G1 and G2 with an asymmetry factor A. The probability of a background-gamma triggering G1 and G2 is then AG_b and the probability of not triggering either detector becomes $(1 - AG_b)$. The adjusted probabilities with this factor is:

$$\begin{aligned}
P_b(0) &= (1 - AG_b)^2(1 - G_b)^2 && (6.10)\\
P_b(1) &= 2AG_b(1 - AG_b)(1 - G_b)^2 + 2G_b(1 - AG_b)^2(1 - G_b) && (6.11)\\
P_b(2) &= A^2G_b^2(1 - G_b)^2 + 4AG_b^2(1 - AG_b)(1 - G_b) + G_b^2(1 - AG_b)^2 && (6.12)\\
P_b(3) &= 2AG_b^3(1 - AG_b) + 2A^2G_b^3(1 - G_b) && (6.13)\\
P_b(4) &= A^2G_b^4 && (6.14)
\end{aligned}$$

The asymmetry factor was approximated by taking the ratio of single triggers in G1 and G2 to triggers in G3 and G4. This produced a value $A \approx 3$. To be completely thorough, an asymmetry factor could be assigned to each detector, but the complexity, computing power and time required were prohibitive. Additionally, trigger rates of G1 and G2 were nearly identical, as were those for G3 and G4, so further approximation was deemed of minimal value.

The interactions between positron-gammas and the G detectors are not as simple. In a negatron-positron annihilation, two positron-gammas are emitted in opposite directions and do not act completely independent of each other; however, we may consider basic geometric arguments to derive the probabilities of each case. We similarly defined an unknown parameter G_p which is the probability that a G detector is triggered by a positron-gamma.

We first consider one of the two positron-gammas which may trigger one of four G detectors. The total probability of triggering a G detector for this positron-gamma is $4G_p$. The total probability of this positron-gamma not triggering any of them is $(1-4G_b)$. Because positron-gammas are emitted in opposite directions, when one triggers or does not trigger a detector, the other positron-gamma can only physically interact with one of the other three G detectors. The other positron-gamma then has a total probability of $3G_b$ of triggering a detector or $(1-3G_b)$ or not triggering a detector. Note that we ignore the unlikely case that a positron annihilates close enough to a G detector such

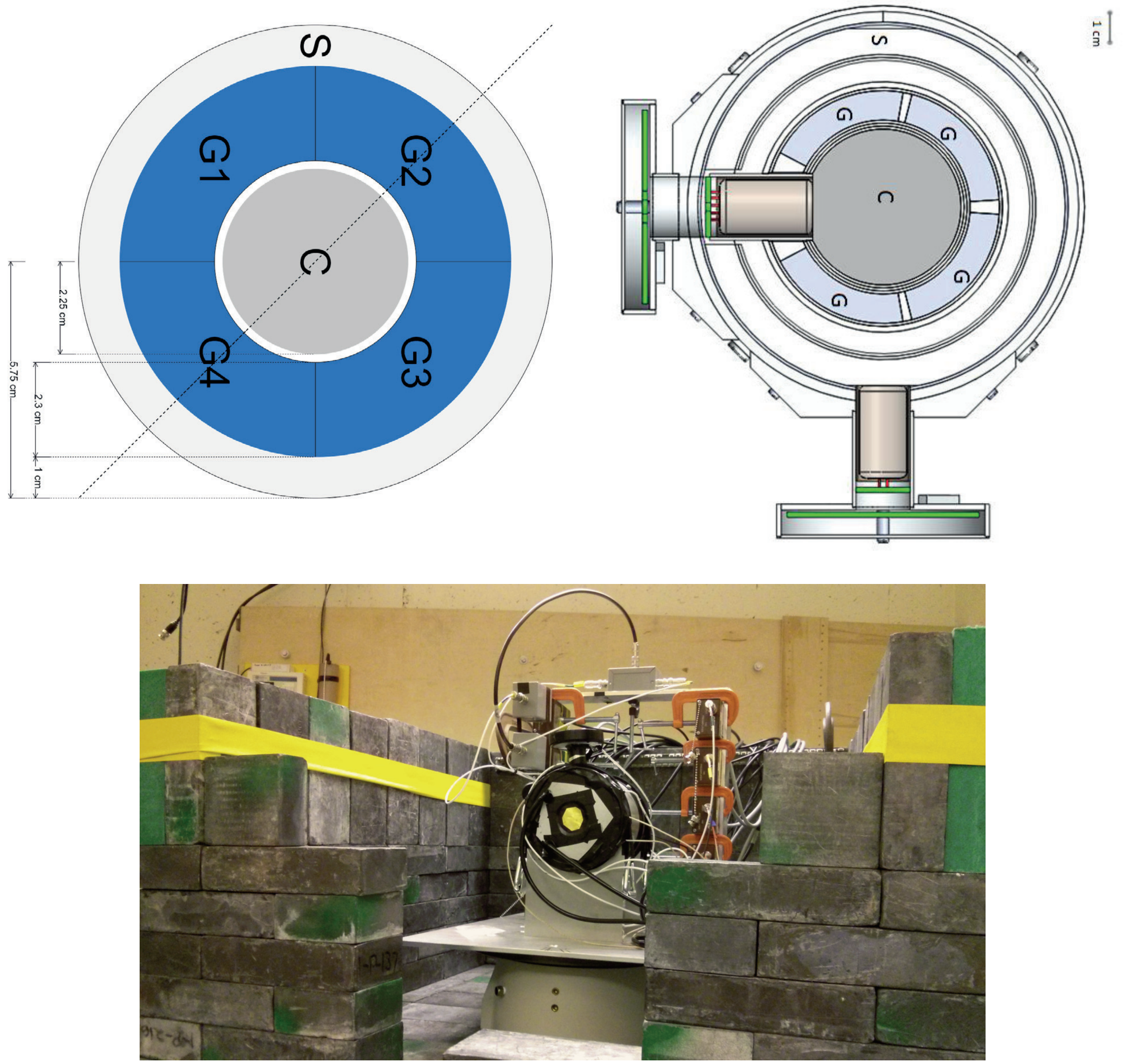

Figure 6-1: The top-down cross-section of the PICAP model and prototype drawing are rotated to reflect the orientation of the the G detectors when resting on its mount. The prototype instrument is less shielded by lead towards the top, resulting in increased exposure to background-gammas in G1 and G2, compared to G3 and G4.

that there are two 0.511-MeV triggers in that same detector. The probabilities then become:

$$P_p(0) = \quad (1-4G_p)(1-3G_p) \quad = (1-4G_p)(1-3G_p) \tag{6.15}$$

$$P_p(1) = \quad 2(4G_p)(1-3G_p) \quad = 8G_p(1-3G_p) \tag{6.16}$$

$$P_p(2) = \quad (4G_p)(3G_p) \quad = 12G_p^2 \tag{6.17}$$

$$P_p(3) = \quad P_p(4) = 0 \tag{6.18}$$

There are only two positron-gammas per annihilation, so there are only three probabilities. These are the total probabilities that zero, one, and two G detectors are triggered, which can be divided by one, four, and six respectively to obtain the probability for each individual case/combination of detectors. These probabilities do not add up to 1, so they are normalized using the sum of these equations. These represent the simplest case, but require further adjustment.

A positron-gamma may do one of three things: miss a G detector entirely, hit a G detector and produce a 0.511-MeV signal, or hit a G detector and fail to produce a 0.511-MeV signal. If the first positron-gamma passes above or below the G detector stack, the second one is also more likely to miss the other three detectors. Furthermore, if a positron-gamma enters a G detector but does not trigger a 0.511-MeV signal, then the other one is also likely to fail to produce a signal. $P_p(0)$ should increase as a result. For the opposite case, if one positron-gamma triggers a detector, then there is an increased probability that the other one triggers one of the other three detectors, suggesting that $P_p(2)$ should also increase. To account for these effects, a geometrically-based correlation factor F was added:

$$P_p(0) = (1-4G_p)(1-3G_p \div F) \quad = \quad (1-4G_p)\left(1-\frac{3G_p}{F}\right) \tag{6.19}$$

$$P_p(1) = 2(4G_p)(1-3G_p \times F) \quad = \quad 8G_p(1-3FG_p) \tag{6.20}$$

$$P_p(2) = (4G_p)(3G_p \times F) \quad = \quad 12FG_p^2 \tag{6.21}$$

$$P_p(3) = P_p(4) = 0 \tag{6.22}$$

F increases $P_p(0)$ and $P_p(2)$ but decreases $P_p(1)$ because we expect a second trigger if the first positron-gamma triggers a detector. For the PICAP prototype, F was calculated to be 2.36865. This value was determined computationally by integrating the gamma interaction probabilities over the height of C at the center of the detector [private communication, Clifford Lopate]. These probabilities also require normalization. The probability for each unique combination of detectors triggered (calculated by dividing by one, four, and six, respectively) is then:

$$P'_p(0) = (1 - 4G_p)(1 - 3G_p \div F) \quad = \quad \frac{(1 - 4G_p)}{\mathcal{N}}\left(1 - \frac{3G_p}{F}\right) \tag{6.23}$$

$$P'_p(1) = 2(4G_p)(1 - 3G_p \times F) \quad = \quad \frac{2G_p}{\mathcal{N}}(1 - 3FG_p) \tag{6.24}$$

$$P'_p(2) = (4G_p)(3G_p \times F) \quad = \quad \frac{2F}{\mathcal{N}}G_p^2 \tag{6.25}$$

$\mathcal{N}$ is the normalization, which is just the sum of the unnormalized probabilities. $P'_p(0)$ is the probability of the one case where no detectors are triggered by a positron-gamma. $P'_p(1)$ is the probability of each of the four possible cases that only one detector is triggered by a positron-gamma. $P'_p(2)$ is the probability of each of the six possible combinations of two detectors being triggered.

We complete our statistical model by combining both sets of probabilities into one set, denoted by χ_n were n is the number of G detectors triggered, which is obtained by multiplying the total of P_b and P_p (normalized) and sorting the cross-terms:

$$\begin{aligned}
\chi_0 &= P_b(0)P_p(0) \\
\chi_1 &= P_b(0)P_p(1) + P_b(1)P_p(0) \\
\chi_2 &= P_b(0)P_p(2) + P_b(1)P_p(1) + P_b(2)P_p(0) \\
\chi_3 &= P_b(1)P_p(2) + P_b(2)P_p(1) + P_b(3)P_p(0) \\
\chi_4 &= P_b(2)P_p(2) + P_b(3)P_p(1) + P_b(4)P_p(0) \\
\chi_5 &= P_b(3)P_p(2) + P_b(4)P_p(1) \\
\chi_6 &= P_b(4)P_p(2)
\end{aligned}$$

Because P_b and P_p were already normalized, these equations are also normalized; however, χ_5 and χ_6 are physically impossible, because there are at most four G detectors that can be triggered.

A background gamma simultaneously entering a G detector along with an annihilation gamma would cause a signal outside of the limits of our trigger requirements of 0.511-MeV ± 0.100 MeV, thus the event would be automatically rejected. Additionally, if broken down into probabilities per unique detector combination, certain terms that reflect permutations of detector combinations, had to be removed as well (e.g. G1 and G2 and G2 and G1 are the same combination of two-trigger events). χ_0 through χ_4 were renormalized, and the overall normalization factor is then these invalid probabilities, χ_5 and χ_6, and permutation cross-terms subtracted from 1:

$$\begin{aligned}
\chi_0 + \chi_1 + \chi_2 + \chi_3 + \chi_4 + \chi_5 + \chi_6 + (\text{other terms...}) &= 1 \\
\chi_0 + \chi_1 + \chi_2 + \chi_3 + \chi_4 &= 1 - \chi_5 - \chi_6 - \ldots \\
\frac{\chi_0 + \chi_1 + \chi_2 + \chi_3 + \chi_4}{1 - \chi_5 - \chi_6 - \ldots} &= 1
\end{aligned}$$

χ is the complete representation of our statistical model for determine the values of G_b and G_p that maximizes the likelihood $\mathcal{L}$ for a given data set. In the next section, we present the results of this process.

6.4 Maximum Likelihood Calculation

For the ISU/IAC data, we had already limited our analyses to subsets of negatron and positron beam data deemed to contain single particles stopping in C. Additional cuts were made on D2 and D3 energy loss histograms (discussed in Chapter 5). The anticoincidence shield S was almost always triggered due to the spreading out of electrons by the magnet in the beam vault and was ignored. A 0.511-MeV trigger in G1–G4 was defined by a signal of 0.411–0.611 MeV (refer to Table 5.3 for channel thresholds used). The events in each trial were then counted and sorted for each of the sixteen combination of detectors triggered (Table 6.1). We recall:

$$\mathcal{L}_i = k_i \ln \lambda_i(G_b, G_p) - \lambda_i(G_b, G_p) - \ln k_i! = k_i \ln \chi_i(G_b, G_p)k_{\text{total}} - \chi_i(G_b, G_p)k_{\text{total}} - \ln k_i! \quad (6.26)$$

For each case, the number of events counted is k. There is an associated probability χ based on our statistical model, where λ for that case is χk_{total}, where k_{total} is the sum of all the events. χ is based on two parameters G_b and G_p. A brute-force approach was used to determine the values of G_b and G_p that maximizes the likelihood $\mathcal{L}$ by a two-parameter (G_b and G_p) mapping and finding the peak.

For each pair of parametric values (G_b, G_p) the probability was calculated for each case and from that, a likelihood for calculated for each of the sixteen cases. The total likelihood for each pair of parameters is just the sum of the likelihoods for all sixteen cases (each corresponding to the product of the probabilities). This calculation is repeated after varying G_b and G_p iteratively in small increments for values spanning from 0 to 0.25. G_p could not exceed 0.25 by the way we defined our statistical model for interaction of positron gammas.

In the analysis software, values for probabilities and likelihoods for each pair of parameters populated elements of two-dimensional arrays. By using the arrays, we mapped out the likelihood for a range of values of (G_b, G_p), which were visualized as three-dimensional plots, with contours of equal likelihood. The maximum likelihood is located at the point where the contour plot peaks, which determines the best estimate of the parameters, G_b and G_p.

We limited this method to beam trials where there was a sufficient number of events after selecting single-particle events and there was a corresponding trial for both positrons and negatrons. This limited the analysis to 4.5-MeV negatrons and positrons at normal incidence, 5.4-MeV negatrons and positrons at normal incidence, and 5.4-MeV negatrons and positrons at 12° incidence. Fortunately, these are particles energies that corresponded to the highest expected detection efficiencies for electrons and positrons based on EGS4 Monte Carlo simulations (Figures 3-4 and 3-5, respectively).

Maximum likelihood contour plots were also generated for similarly sized subsets of events from the EGS4 Monte Carlo data. For these subsets from the Monte Carlo data, Poisson noise was randomly generated in G1–G4 to simulate additional random gamma triggers in these detectors. Additional noise was added to G1 and G2 to simulate the asymmetry of gamma interaction in these detectors. These subset of events were then randomly selected and sorted and counted by the number of 0.511-MeV triggers in G1–G4 as was done with the experimental data.

The error in the most likely parameter, G_b and G_p, estimations is defined by the likelihood $\mathcal{L}$ decreasing by 0.5, corresponding to a 1-σ error estimate.

For negatrons, the most likely value of G_p was consistently calculated to be 0; that is, the probability that a G detector is triggered by a positron-gamma is 0. This is expected in the absence of positrons. There should then be an increase in the calculated value of the most-likely G_p for positrons, as is also observed. Taking for example Figure 6-2, the plots compare the results of the maximum likelihood analysis on the experimental trials for 4.5-MeV positrons and negatrons on top with the results of the same analysis performed on a subset of data from Monte Carlo simulations with 4.5-MeV positrons and negatrons. For the negatron data in the absence of positrons, G_p is consistent with 0. In the presence of positrons, it is evident that G_p at the maximum likelihood is not zero, indicating the detection of positrons. Figure 6-2, plot (b), shows a near 24-σ experimental detection of positrons. A 1-σ error estimate corresponds to where the likelihood $\mathcal{L}$ is estimated to be decreased by 0.5.

When comparing experimental data with the Monte Carlo data, the values of the contours and likelihoods are not entirely similar because they are tied to the total number of events. This is not as relevant as the observation that there visual similarities in the contour shapes between plots for experiment and simulation data. Similar qualitative and quantitative trends are evident in Figure 6-3. We anticipated a performance difference between the theoretical model and the prototype that

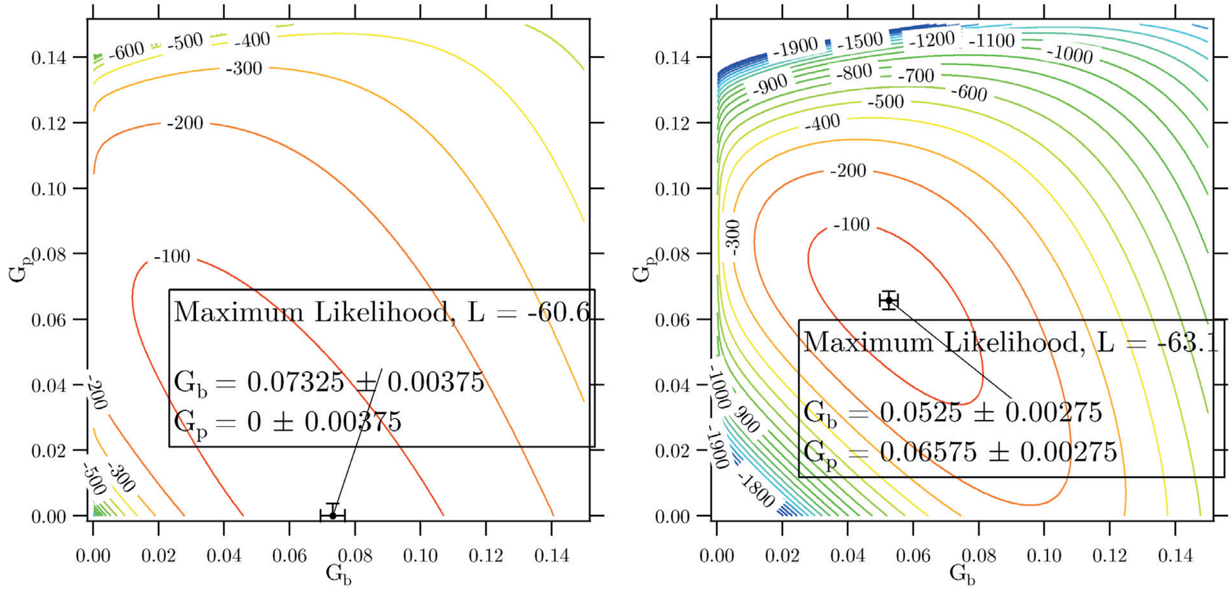

(a) 4.5-MeV negatrons (experimental) (b) 4.5-MeV positrons (experimental)

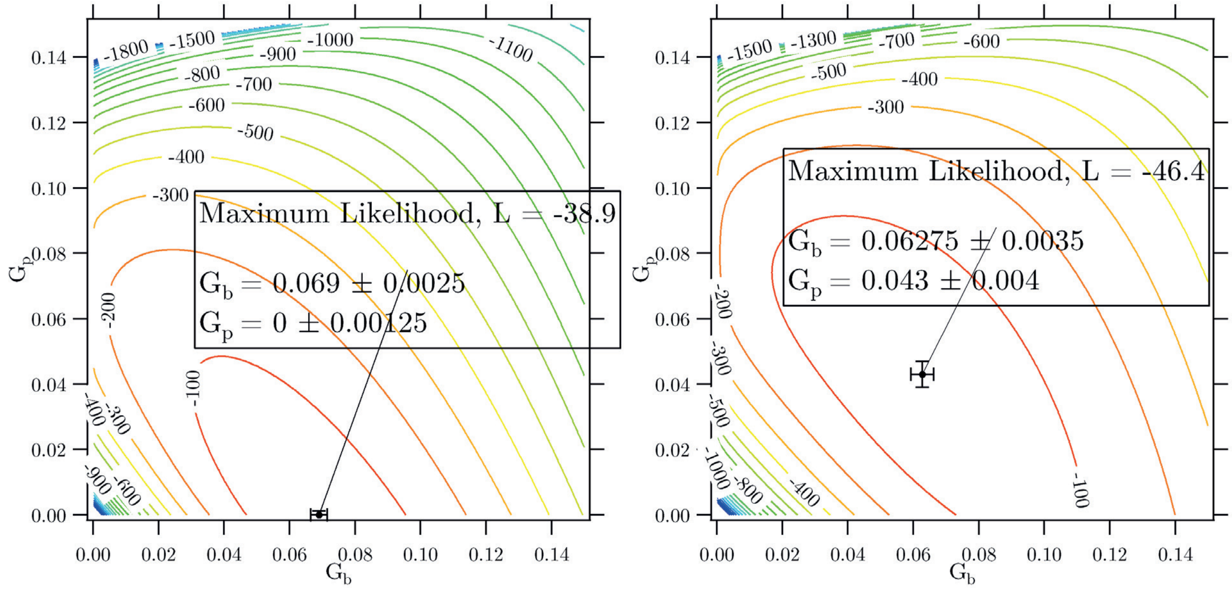

(c) 4.5-MeV negatrons (simulation) (d) 4.5-MeV positrons (simulation)

Figure 6-2: Likelihood contour plots for 4.5-MeV negatrons and positrons at normal incidence, compared to those for 4.5-MeV negatrons and positrons, simulated in EGS4. Plots compare vertically (a) to (c) and (b) to (d). Plot (b) shows a nearly 24-σ detection of positrons.

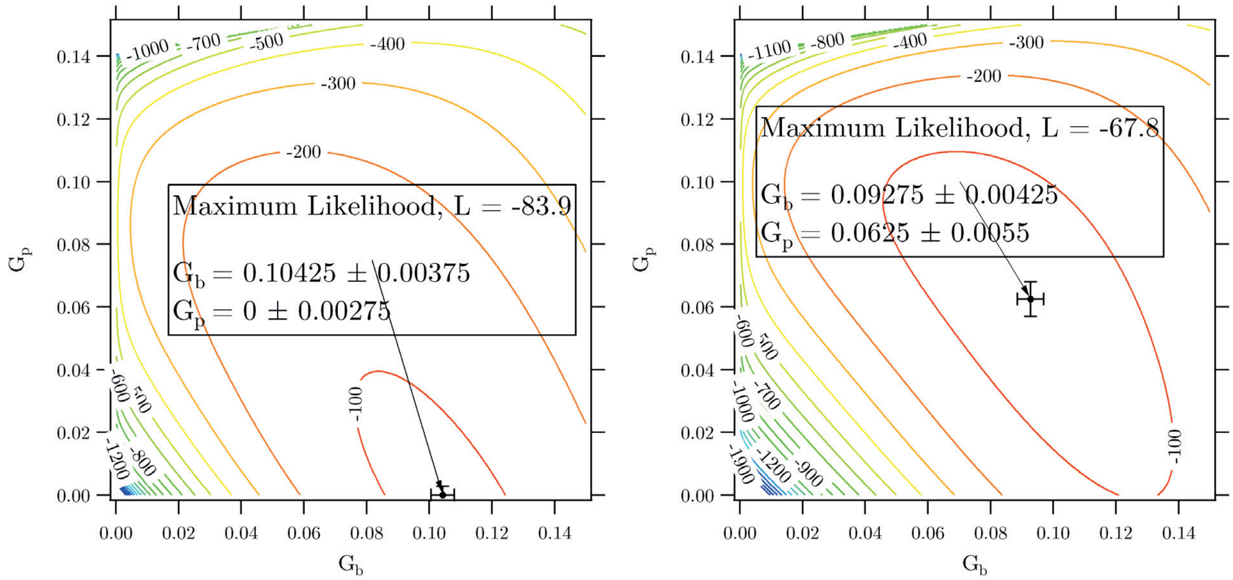

(a) 5.4-MeV negatrons (experimental)

(b) 5.4-MeV positrons (experimental)

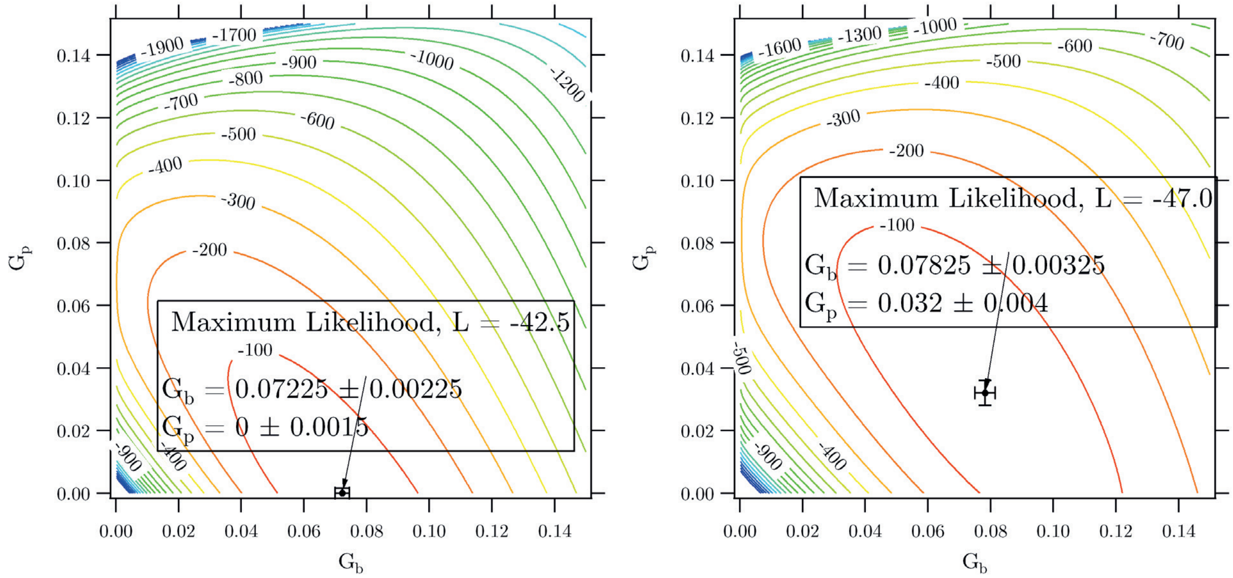

(c) 5.5-MeV negatrons (simulation)

(d) 5.5-MeV positrons (simulation)

Figure 6-3: Likelihood contour plots for 5.4-MeV negatrons and positrons at normal incidence, compared to those for 5.5-MeV negatrons and positrons, simulated in EGS4. Plots compare vertically (a) to (c) and (b) to (d). Plot (b) shows a 11-σ detection of positrons.

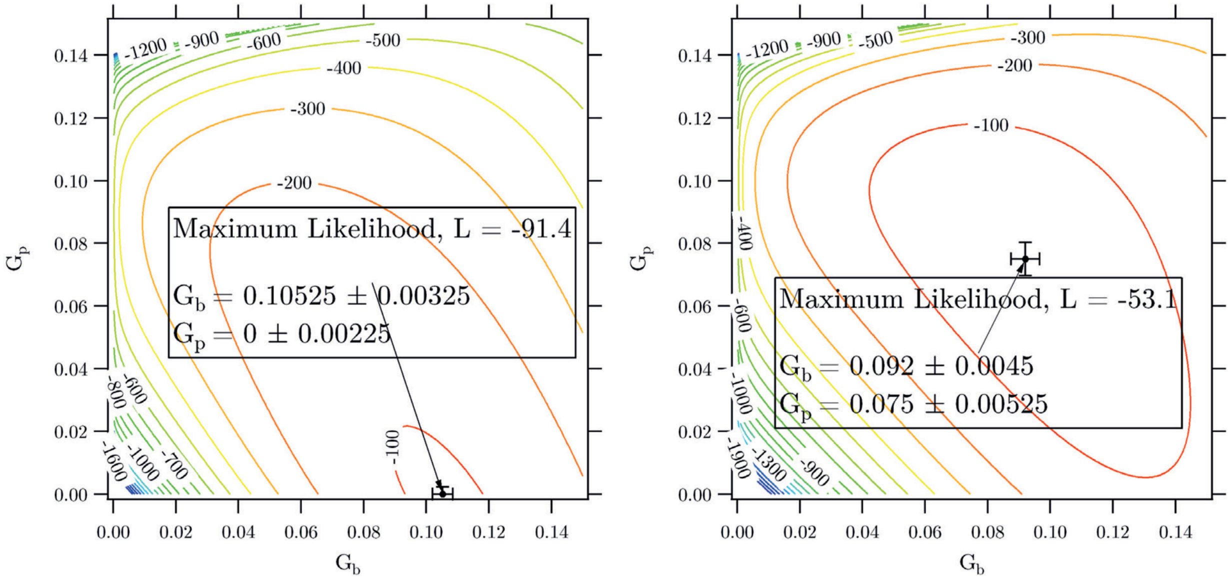

(a) 5.4-MeV negatrons (experimental)

(b) 5.4-MeV positrons (experimental)

Figure 6-4: Likelihood contour plots for 5.4-MeV negatrons and positrons at 12° incidence. Note that the results of the maximum likelihood method here is consistent with that of 5.4-MeV negatrons and positrons at normal incidence. The plot on the right shows a 14-σ detection of positrons.

we ultimately were unable to measure; however, their responses under this analysis method show that the instrument concept functions as intended. If we did not have any modeling data, such as the case shown in Figure 6-4 for 5.4-MeV negatrons and positrons, where the angle of incidence was 12°, our analysis reveals us that positrons were detected with some precision (14-σ). This is regardless of whether or not there was any prior knowledge of what the detection rate or efficiency is expected to be. From a previous calculation (Equation 3.5), we expected that the response of the prototype would fall within a factor of 2 of the response of the model, and the values for G_p certainly do agree within a factor of 2, when comparing the experimental and simulation data.

It should also be noted that the gamma background varied between negatron and positron beam runs of the same energy. This is expected, because more positrons means more of them stop and produce 0.511-MeV γ-rays in the vault structure. Quantitative and qualitative agreement between results of applying the maximum likelihood method to experimental and simulation data show that the PICAP prototype instrument detects positrons within expectation established by the EGS4

Monte Carlo simulations.

The maximum likelihood analysis showed that the prototype can distiguish when positrons are present and when they are not present. This qualitative similarity of the response of simulation data under the same analysis supports this conclusion. We will discuss and conclude the results of each phase of the project in the final chapter of this work.

CHAPTER 7

DISCUSSIONS AND CONCLUSIONS

7.1 Summary of Results

Positron Identification by Coincident Annihilation Photons (PICAP) is an instrument concept and detector scheme to the measure moderate energy positrons (~2–10 MeV). The goal of this work is to determine the viability of PICAP as the basis of future instrumentation, suitable for flight missions in deep space. To support the concept, the evolution of PICAP from an idea to a tested prototype was detailed. A baseline design was refined and modeled with computer simulations. A real, prototype instrument was designed and assembled based on the modeling. After a series of initial tests establishing functionality and detector calibration, the PICAP prototype instrument underwent energetic particle exposure at two accelerator facilities to determine the proton and negatron/positron response and validate expectations from modeling. This chapter is a summary of the results of the process, showing the success of the proof-of-concept in relation to the scientific goals.

PICAP began as a theoretical, baseline model, an idealized configuration of detector geometries centered about a detector stack for the identification of positrons. Particles penetrating these detectors exhibit energy loss unique to the particle mass, charge, and energy (dE/dx). Protons are rejected from identification based on their greater energy loss, due to being more massive and slower at similar energies. Particles within the energy interval of interest stop in a central detector (denoted C), which is surrounded by a toroidal array of four γ-ray detectors (G1, G2, G3, and G4). If no signal is detected in G1–G4, then the particle is detected as an "electron," which collectively includes both negatrons and positrons, regardless of charge. PICAP is incapable of specifically identifying negatrons; a positron is identified if a 0.511-MeV signal is detected in two different G detectors, indicating positron annihilation. A fourth SSD, called D4, and anticoincidence shield S works together to reject particles energetic enough to penetrate the entire stack, particles entering from the side, or particles that scatter from within the stack.

For the baseline design, the electron (e^- or e^+) detection efficiency reached ~50% for negatrons and ~20% for positrons, both with energies of 5–8 MeV. The electron detection efficiency of positrons is significantly lower because the detection of a single annihilation photon invalidates an event for electron identification. The positron detection efficiency, the percentage of positrons identified as positrons, of the baseline PICAP design was at a maximum of ~1.2% for positrons with energies of 4.5–6 MeV. The percentage of negatrons being misidentified as positrons was at most ~0.001% towards the upper limit of the energy interval of interest. This is the expected response of baseline design, which is an idealized representation of the smallest form-factor that PICAP can occupy. An instrument based closely on this design should be capable of meeting scientific goals with minimal mass (as well as power and telemetry requirements), making it suitable for payloads on deep-space missions.

A PICAP prototype instrument was designed and assembled based on the baseline design. In addition to structural and electronic elements, there were notable changes in adapting the original design to a physical prototype. There were significant reductions in the active areas of the silicon SSDs. The active surface area of the detectors used for D1, D2, and D3 was 300 mm^2, which is about 60% the area of these detectors in the model. The detector used for D4 had an area of 2000 mm^2 which is less that 25% of the area of D4 in the baseline design, but the anticoincidence shield S is extended to account for the reduction in the size of D4.

G1–G4 were modeled as four toroidal segments of CsI that were each 2.3-cm thick. The total mass of CsI required would be 1.1 kg. It was then calculated that one cm of BGO was equivalent in photon absorption probability to 2.3 cm of CsI. Switching from CsI to BGO reduced the volume occupied by G1–G4 by over 50% and the mass by 30% to a total of 600 g, without reducing the detection efficiency.

The first major test of the PICAP prototype instrument was the proton accelerator experiment at the Francis H. Burr Proton Therapy Center at Massachusetts General Hospital (MGH) on 1 June 2013. The instrument was exposed to proton beams at energies up to 200 MeV at multiple angles of incidence. The purpose of the experiment was to determine the instrument's response to energetic protons and demonstrate its ability to discriminate protons from positrons and electrons. Positron identification criteria were applied to proton data to determine the number of events identified as electrons or positrons.

A high proton rejection efficiency is essential to demonstrating the viability of PICAP, since positrons are rare, compared to protons in space. The MGH proton experiment showed that less than 0.01% of protons were misidentified as electrons, while less than 0.001% of protons were misidentified as positrons. Consider an example of some flux of particles accepted into the PICAP detector stack: 10^4 positrons, 10^5 negatrons, and 10^6 protons (Table 7.1).

Table 7.1: Example of approximate PICAP particle detection rates in space.

	Number of Particles	Percentage Identified As Positrons	Number Identified As Positrons	Percentage Identified As Electrons	Number Identified As Electrons
protons	10^6	0.001%	10	0.01%	100
negatrons	10^5	0.001%	1	50%	50000
positrons	10^4	1%	100	20%	2000

Our example showed that proton contamination of the positron identification channel could be as great as 10%. While this seems significant, this would be within an acceptable statistical precision of 10% after having observed 100 positrons, where the uncertainty is the square root of the number of events counted. PICAP would also be calibrated for background substraction from measurements. This example represents a dramatic case and it should be noted that the majority of positron misidentifications (5) were from one particularly trial (refer to Table 4.6), 179.1-MeV protons at a 12°angle of incidence, which may be an outlier. It is simply highly unlikely that a proton is identified as a positron due to the stringent two-photon detection requirement.

Following the success of the proton experiment, the prototype instrument was transported to the Idaho Accelerator Center at Idaho State University (IAC/ISU) for electron accelerator testing. The experiment was conducted on 9–10 December 2013 with the purpose of measuring the prototype instrument's response to negatrons and positrons. The ultimate goal was to determine a detection efficiency of negatrons and positrons as electrons and positrons and validate of the EGS4 Monte-Carlo simulations. The prototype instrument was exposed to negatrons and positrons with energies of 4.5–8.8 MeV incident at multiple angles from the IAC's 44-MeV LINAC, chosen based on the energies where the baseline detection efficiencies are the highest.

The accelerator facility presented two challenges that affected our ability to determine the detection efficiency or rate directly. The LINAC emitted pulses of electrons with widths of tens of nanoseconds, often containing more than one particle. At the end of the beam line, a magnet was positioned to direct the particles towards the final target, the PICAP prototype instrument, without further collimation. This process physically fans out the beam. This was by design as an attempt to mitigate the problem of multi-event pulses; however, by almost continuously spreading the particle beam, the anticoincidence shield S was triggered, rendering it useless for its intended function. In addition, despite the fanning of the beam, multiple particles still penetrated the instrument in many cases. The electronics used to process the signals from the prototype's detectors operate at a rate on the order of microseconds, typical for space radiation instruments. With the combination of the nanosecond rate of pulse emission and the fact that each pulse often contained multiple particles, the electronics were unable to temporally resolve every particle individually. Events with only a single particle stopping in C were selected. The beam current was also adjusted in an attempt to minimize multiple-particle events. Unfortunately, several trials had too few valid events for further analysis, including those when lowering the beam current limited the amount of usable data.

The other major challenge at the IAC/ISU electron experiment was the presence of a significance γ-ray background when the beam was in operation. The gamma background was responsible for hundreds of random triggers of the G1–G4 per second, most occurring in conjunction with the particle pulses. We were unable to directly apply the coincident annihilation photon requirement for positron identification due to multiple G detectors often being triggered by background gammas for an event.

The number of electrons and positrons could not be individually counted, so detection efficiencies could be not directly determined. A maximum likelihood analysis was applied to decouple contributions to gamma detections in G1–G4 due to the background and due to positrons stopping and annihilating within the detector stack. This is a statistical approach where the unknown levels of gamma contributions from the background and from positrons were parametrized as probabilities of G triggers. G_b is the probability that a G detector registers a 0.511-MeV ($\pm$ 100 keV) trigger due to a background-gamma, and G_p is the probability that a 0.511-MeV ($\pm$ 100 keV) signal is measured in a G detector due to a positron annihilation photon.

The maximum likelihood method was applied to data for 4.5- and 5.4-MeV negatrons and positrons. For comparison, the same analytical process was applied to EGS4 Monte-Carlo data for those energies, with Poisson noise added to the signals of G1–G4 to simulate a gamma background. The likelihood for each set of data was mapped out for a range of values of the unknown parameters that spanned all possible values of (G_b, G_p) and contour plots of likelihood were produced to visualize the parameter space (Figures 6-2, 6-3, and 6-4). Immediate conclusions that can be drawn are that the maximum of the likelihood function indicates that there was no gamma contribution from positron annihilation for negatron trials, as expected; while for positron trials, the gamma contribution from positrons was above zero with high statistical validity. The background gamma contribution remains reasonably constant over all trials. It is clear the PICAP instrument identifies positrons as positrons and does not identify negatrons as positrons—a key goal of the instrument.

Comparing of the values of G_p between experimental and simulation data sets shows a difference at about a factor of ∼1.5–2, which agrees quantitatively by the differences we estimated from the model. While the Poisson noise introduced may not have perfectly recreated the gamma background, the contour plots also show good qualitative agreement between experiment and simulation. While the model and prototype are not exact matches, quantiative and qualitative agreement shows that the results are reasonable and valid. PICAP is capable of distiguishing between the absense and presence of positrons and works as intended.

7.2 Estimates Of PICAP Measurements In Space

In order to access these moderate energy positrons, measurements have to be made beyond Earth's magnetosphere. PICAP was devised for the detection of such moderate energy positrons minimizing mass, power, and telemetry requirement for an instrument that could be sent into deep space. Proving the viability of the concept requires demonstrating PICAP's capability in a similarly sized, ground-based prototype instrument, that could feasibly be adaptable to a space-flight design.

Mass is the main constraint in the design. Based on the baseline design, a PICAP space-flight instrument was originally budgeted for ∼4 kg, including all electronics and structural elements and a 15% contingency [Connell et al., 2008]. The majority of mass budgeted for the instrument was for G1–G4. In switching to BGO from CsI, we reduced the mass of G1–G4 to 600 g. External laboratory electronics were used and are not included in the mass of the prototype. The total mass of the prototype instrument was 3.3 kg. Built-in onboard electronics would require about 1 kg of additional mass. A total of 4.3 kg is reasonably close to the initial estimate of the baseline design.

This mass was not chosen at random, but based on typical allotments for charged particle instruments in deep space. For example, we can consider fairly recent Announcements of Opportunity

(AO) for missions such as Solar Probe Plus, Solar Orbiter, and Europa, which elicit proposals. The AOs outline for these deep-space missions allotted mass and power to proposed instruments. For mass, charged particle instrument allocation for these missions were typically budgeted between 4 and 8 kg. Instruments like these are almost always secondary payloads, and PICAP fits well within these constraints.

PICAP's power budget was also designed based on real AO estimates. The above mentioned mission AOs allot between 3–5 W per charged particle instrument. Our experience in space instrumentation has shown that microsecond electronics can be built at an allotment of ~0.5 W per channel. PICAP's nine channels could be built for less than 5 W. While higher speed electronics are available, they raise the required power above normal alllocations for proposed charged particle space instruments. Slower electronics would extend the time required for collection of events.

The primary background concern in space is protons, which may contribute to the background in other ways. Pions (particularly π^+) that are produced in the instrument would escape or decay to a muon that escapes, which would trigger D4 or the anticoincidence shield. In rare instances, inelastic proton collisions with molecules in the C detector may produce unstable nuclides capable of β^+ decay; however, the half-lives of carbon and nitrogen nuclides that may result from such collisions is far longer than the coincidence threshold required (based on the electronics, on the order of microseconds) between particles stopping in C and the detection of annihilation radiation [Connell et al., 2008], which makes this case highly unlikely. The proton experiment at MGH showed PICAP's exceptional capability of rejecting protons from positron and electron identification.

As protons are expected to be the main source of background, a gamma background of the magnitude that was present at the IAC/ISU facilty would not be expected in deep space where a PICAP-type instrument is intended to perform. Any gamma background would be the result of positron annihilation in the spacecraft on which such an instrument would be mounted. For example, a proton may cause the creation of a β^+ emitter. In order for this event to be identified as a positron, it could be coincident with the detection of two 0.511-MeV annihilation photons created by the spacecraft at two separate instances, because only one of two of the photons created from outside of the detector stack is likely to interact with a G detector in the stack. This would be unlikely even if background gamma created by the spacecraft was nearly as prevalent as the gamma background at the IAC.

If a high-energy γ-ray were to pair produce in the C detector, creating a negatron and positron, a positron detection would occur if the positron remains in C and annihilates while the negatron escapes through the aperture triggering D2 and D3. One would presume that if a negatron created from pair production were able to escape the detector stack by geometry, the corresponding positron would be energetic enough to escape C as well. A negatron escaping through the aperture from C is also geometrically unlikely. The surface area of C is 93.7 cm^2, while the active areas of D2 and D3 are 3 cm^2 by comparison.

With the current prototype design and sources of background considered, we can estimate its suitability to measure positrons in space, relative to scientific goals. Based on the geometrical factor calculated for the baseline design [Connell et al., 2008] and the steady-state GCR electron flux in the Heliosphere [Ferreira et al., 2001], the baseline design would detect electrons at a rate of 0.0048 particles per second, over the moderate energy range of 2–10 MeV. Again if we assume that the negatron population is an order of magnitude greater than the positron population and approximate the positron detection efficiency to be ∼1%, the baseline design would be capable of detecting 100 positrons, a 10% measurement, in 240 days. This is suitable for measuring charge-sign effects over Solar cycle time scales of 11 (or 22) years.

At the IAC/ISU, we were unable to determine a detection rate of positrons, but we know that the maximum likelihood parameter, G_p, does not differ by more than a factor of 2 between the prototype and model. We had addressed differences expected in positron detection capability between the model and prototype. Our prototype is slightly smaller than the model used to calculate positron collection in the baseline design (used in Connell et al. [2008] to make estimates of positron measurements). The active area of D2 and D3 is 61% of the area of D2 and D3 in the baseline model and G1–G4 only surrounds 80% of the space around C due to having to accommodate the PMT for the C detector. The surface area of C was increased by 19%. The detection efficiency of PICAP for positrons scales as $1.19 \times (0.9 \times 0.98 \times 0.8)^2$. These are variations in performance we would expect to see at an accelerator facility.

In space, we have to consider the directionality of the particle distribution. The geometrical factor of PICAP for collection of particles scales as $(0.61)^2$, from the reduction in size of D2 and D3 of the instrument. Cumulatively, the product leads to a scaling factor for the time needed to collect a fixed number of positrons (e.g. 100 for a 10% measurement):

$$0.61 \times 0.61 \times 1.19 \times (0.9 \times 0.98 \times 0.8)^2 = 0.22 \tag{7.1}$$

This is an estimate of the cumulative effect on the total detection rate of the prototype instrument, compared to the theoretical model, considering an isotropic particle flux. If we had actually built a space instrument to these exact specifications, the effects cause a potential reduction of the positron efficiency from 1.2% to 0.7% and an increase in collection time by 2.68. Together, these would increase the time needed for the measurement of 100 positrons. The detection efficiencies of electrons and false identification of protons would presumably scale accordingly, and it comes down to an issue of the rate of positron detection. The prototype we have tested would take $(0.22)^{-1} \approx 3$ times longer than the estimates made by Connell et al. [2008] to achieve a 10% measurement (over 1000 days, or about three years). This is still a reasonable time scale if positron and electron fluxes are being monitored over the course of 11-year Solar cycles.

The prototype, which was assembled with compromises and not meant for space-flight, would be capable of the intended scientific applications. A comparable space-flight instrument would be even more capable, absent of some of the compromises that were made to build the prototype.

Because the prototype demonstrated the capability of positron detection in an environment of significant γ-ray background, a PICAP-type instrument should exhibit improved performance in environments with considerably lowerγ-ray background considerations. If PICAP is capable of making a long-duration 10% measurement, it would be able to do so also for SPEs where the particle flux would be tens to thousands of times greater over a shorter span of time. Increased particle rates may result in a significant increase in background. To address any potential concerns, we consider a typical Solar flare (Figure 7-1).

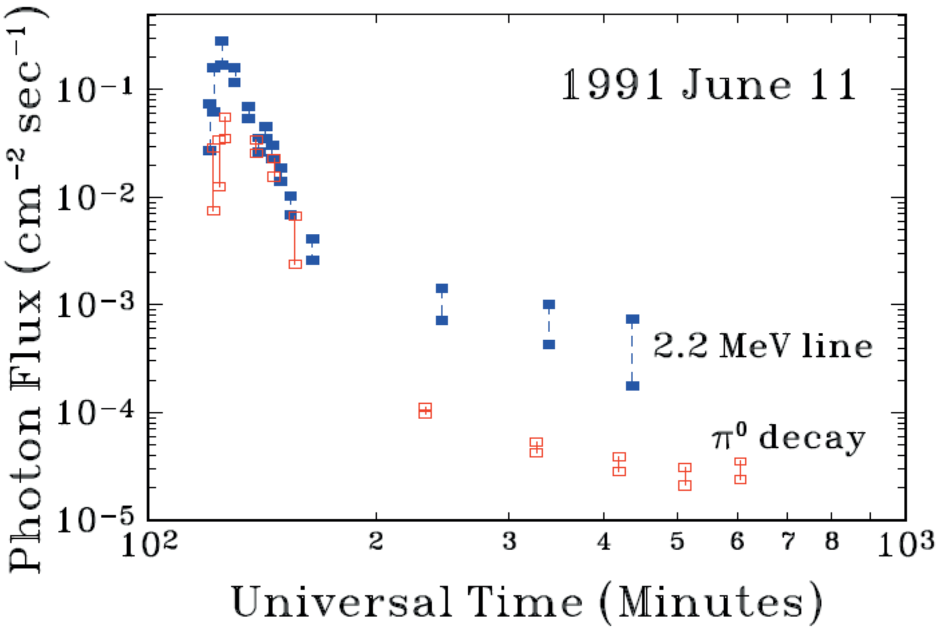

Figure 7-1: Time evolution of photon flux of a Solar flare [Ramaty and Mandzhavidze, 2000].

If we take the maximum photon flux from the Solar flare in Figure 7-1 to be ~0.5 cm^{-2} s^{-1} [Ramaty and Mandzhavidze, 2000] and the effective area of a single G detector to be ~20 cm^{-2}, then the photon rate could be as high as ~10 per second, over a span of hundreds of minutes, assuming that all of the photons are 0.511-MeV. This would be a marked improvement in environment when compared to the average of hundreds of background triggers per second (often coinciding with beam pulses) at the IAC. It stands that protons are the main background concern to PICAP, and we have shown that the proton rejection rate is high.

Adaptability is an important advantage of the PICAP design. Depending on the application and/or project budget, more mass may be allocated. Given more mass, we would prioritize increasing the amount of crystal scintillator used for the G detectors. Increasing the amount of crystal scintillator increases the positron detection efficiency on the order of the square of mass, based on a thin-target approximation. For example, doubling the mass of crystal quadruples the positron detection effiency, without fundamentally changing how the instrument functions. The potential for improvement in performance is valuable when considering what a PICAP-type instrument would be required to do.

A limited history of moderate energy positron measurements was presented in the Chapter 1 of this work. Measurements of positrons in these energy regimes are rare, due to the lack of instruments designed to detect these positrons. The majority of positron measurements made in space have been with massive, and power-intensive magnet spectrometers that are flown aboard balloon-borne payloads or aboard satellites in low-Earth orbit, including PAMELA and AMS-02. Summarized in Figure 1-5, these instruments primarily make measurements from a few GeV up to 50 or a few hundred GeV. We explored two main fields of study in Galactic cosmic rays (GCRs) and Solar energetic particle events (SPEs).

Moderate energy positrons are secondary particles of interactions between Galactic cosmic rays and the interstellar medium. Upon passage into the Sun's Heliosphere, GCRs undergo modulation, spatial and temporal variations under the influence of the solar wind plasma and Solar magnetic field. Predictions were made on how cosmic ray modulation varied between 11-year Solar magnetic cycles, including the long-term investigation of charge-sign effects of particle drifts.

Solar cycles are characterized by the cyclic amount of activity varying between what are known as Solar maximum and Solar minimum. Each cycle is also characterized with the direction of the polarity of the Solar magnetic field, called A+ and A-. Predictions of cyclical variations of positron and negatron fluxes may be confirmd with positron flux measurements. Consider the following example (based on data from Clem and Evenson [2008], Lopate [1991]):

Solar Cycle	Negatron Flux (cm^2-sr-s-MeV)	Positron Flux (cm^2-sr-s-MeV)	Expected Positron Fraction	10% Error
Minimum, A-	6.0×10^{-7}	1.2×10^{-7}	0.17	0.017
Maximum,	1.0×10^{-7}	1.0×10^{-8}	0.09	0.09
Minimum, A+	1.2×10^{-6}	6.0×10^{-8}	0.05	0.005

Table 7.2: Example of predicted variations in GCR electron intensities over the course of an A- and A+ Solar cycle, between Solar minimum and Solar maximum.

We can take the energy of particles in Table 7.2 to have moderate energy ∼5 MeV. The negatron flux varies by a factor of 6 during the A- cycle and a factor of 12 during the A+ cycle. Assuming that negatrons outnumber positrons 10 times, we can predict to measure variations in the positron fractions during Solar minima (Table 7.2) by about a factor of two from the initial level at the maxima. A PICAP-based instrument capable of making 10% positron measurements, would be able to monitor these variations over timescales during the duration of a Solar cycle and confirm (or invalidate) predictions made about GCR modulation.

Moderate energy positrons may also originate from Solar particle events during which charged particles are accelerated and energized, such as in a flare. These involve high-energy nuclear interactions that generate both positrons and γ-rays that must traverse some path through the Solar atmosphere, depending on the depth at which they are generated. Their detection (or lack of) would constrain models that predict the energy spectra and time-intensity profile of SPE acceleration models. For instance, we can better understand the density of ambient material and the strength of the source of these events by measuring the positrons flux and γ-rays signals emitted.

A PICAP-based instrument could be used to be measure the positron flux directly rather than the positron fraction, having been normalized to an accurate measurement of the total electron flux. From just γ-ray measurements alone, the density of ambient Solar material through which they propagated may be extrapolated, but only if there is adequate knowledge of the source of the γ-rays. With the addition of positron measurements, we can extrapolate the density to the value that gives both independently measured γ-ray and positron signals (or a noted absense of positron signals). Density is often a parameter of SPE models, and this would improve and further contrain theories of particle production and acceleration.

7.3 Future Considerations

The viability of PICAP as an instrument concept is driven by its potential to be adapted for spaceflight for positron measurements beyond previously explored near-Earth regimes. Having modeled the baseline design and testing a ground-based prototype instrument based on said design, the logical step forward is to advance this project Technology Readiness Level (TRL). TRL is a NASA-developed assessment scale of the maturity and progress of a technology towards the eventual goal of becoming qualified and proven for spaceflight. PICAP's TRL started at Level 3, which is a characteristic proof-of-concept, and through this work, advanced to Level 5, which is the demonstration of a prototype and its components in a relevant environment(s). Advancing the TRL of the PICAP concept to this level allows it be potentially considered for space instrument development should an applicable AO presents itself.

The PICAP prototype instrument was tested as successfully as possible with available ground-based particle accelerators. The associated challenges have been described in detail. Furthering the research requires testing in an improved environment. This environment exists higher in the Earth's atmosphere, a source of secondary negatrons and positrons, accessible by balloon or aircraft. Provided that the electronics can be powered, the same prototype instrument could be used and would be more practical for testing on an airplane. Increasing the TRL of the PICAP would eventually involve the development and assembly of a newer, standalone version of the PICAP prototype that resembles more of a space-flight instrument. Additionally, a ground-based accelerator does not allow for simultaneous multi-directional testing, as opposed to an atmospheric or space environment.

The PICAP could be expanded to have two or more apertures or viewing cones (e.g., bidirectionality by replacing D4 with aperture SSDs). Depending on the intended application, this would likely introduce a new set of design considerations, such as varying the SSD thickness, the height of the central stopping detector C, and the amount of inorganic crystal scintillator to use for the γ-ray detectors. Each major change to the design would require further modeling and computer simulation.

Where PICAP itself is a dedicated electron and positron detection technique, it may inherently perform other functions. As is, it might serve as an ion detector, strictly using the dE/dx vs. E technique, and/or a very simple γ-ray detector. These additional capabilities depend mainly upon the electronics.

For instance, while we expect to travel beyond low-Earth orbit in order to study positrons related to Solar modulation of GCRs and SPEs, another scientific application has recently emerged in the study of thunderstorms and lightning within the Earth's atmosphere. Thunderstorms produce powerful γ-ray bursts called Terrestrial gamma-ray flashes (TGFs) up to many tens of MeV [Fishman et al., 1994]. These bursts of γ-rays sometimes produce negatrons and positrons that propagate as beams into space along magnetic field lines. The TGFs are related to the electric fields responsible for electrifying thunderstorms and generating lighting, which are poorly understood.

PICAP-like techniques have been used to propose the development of a modular instrument concept called THunderstorm Energetic Radiation MOnitor (THERMO). A THERMO instrument is organized in cells, consisting of modules dedicated to measuring γ-rays directly from TGFs and detecting 0.511-MeV annihilation photons and modules dedicated to electron and positron identification, based partly on the PICAP concept but at much higher efficiencies, with mass being less of a constraint. The proposed THERMO instrument is meant to be able to measure the γ-ray spectrum, as well as the electron and positron spectrum, while distinguishing between each species.

There are scientifically relevant applications to measuring positrons in a previously seldom explored energy regime. Exploring this moderate energy regime requires transporting an instrument deeper into space. For that, we introduced the PICAP detector scheme and motivated its design for its capability to identify charged particles and do so while still being suitable for flying into deep space (i.e. using optimal mass and power). The detector scheme became a prototype. While the experiment was less than ideal at certain respects, we showed that the prototype perfomance is consistent with baseline expectations that were laid, validating the Monte-Carlo modeling. The baseline design is capable of data collection suitable for long-duration monitoring of the type of scientific phenomena that originally motivated the concept. The PICAP system works as intended and is a viable option for any resource budget.

APPENDICES

APPENDIX A

A.1 Proton Energy Loss in PICAP Detector Stack

Table A.1: Table listing idealized proton energy losses in each region of central detector stack from D1–D3, through C, and through D4 at normal incidence. All energies given are in MeV.

Incident Proton Energy (MeV)	ΔE(D1)	ΔE(D2)	ΔE(D3)	ΔE(C)	ΔE(D4)	Final Energy (MeV)
2.000	2.000	—	—	—	—	0.000
2.100	1.940	0.160	—	—	—	0.000
12.200	0.344	11.856	—	—	—	0.000
12.300	0.344	11.947	0.008	—	—	0.000
18.100	0.255	5.916	11.929	—	—	0.000
18.200	0.236	5.886	11.342	0.736	—	0.000
66.600	0.091	1.829	1.829	62.850	—	0.000
66.700	0.091	1.829	1.829	60.722	2.227	0.000
68.300	0.091	1.829	1.829	52.710	11.840	0.000
68.400	0.091	1.829	1.829	52.418	10.586	1.645
69.507	0.091	1.829	1.829	49.729	9.563	6.465
119.964	0.060	1.198	1.198	23.584	1.377	92.546
137.336	0.053	1.064	1.064	20.877	1.198	113.080
145.061	0.051	1.016	1.016	19.937	1.118	121.923
157.680	0.049	0.979	0.979	18.629	1.064	135.981
160.576	0.046	0.950	0.979	18.346	1.052	139.204
179.071	0.045	0.891	0.891	16.865	0.958	159.421
196.159	0.041	0.826	0.826	15.783	0.891	177.790
214.870	0.040	0.798	0.798	14.710	0.826	197.697

These values were primarily used for the proton experiment at Massachusetts General Hospital's Francis H. Burr Proton Beam Therapy Center on 1 June 2013. These numbers were generated by a program, called `range_anl` [private communication, Connell], based on heavy charged particle range tables by Barkas and Berger [1964]. Within the program, the layers of matter are defined, each with a specified material, thickness, and areal density. The particle charge, mass number, and angle of incidence is also specified, yielding the energy lost in each layer penetrated. If the particle is not energetic enough to penetrate a layer, the program returns the layer in which the particle stops, as well as how deep it is projected to travel.

The values for proton energies were strategically chosen to include the beam energies (69.5, 145.1, 160.6, 179.1, and 214.9 MeV) as well as the energies to which these protons are reduced with the 2-cm aluminum beam degrader. Energies required to barely penetrate each detector in the stack are also listed. For example, from the top row, a 2-MeV proton would lose all of its energy and be stopped by D1 (50 μm of Si), but a 2.1-MeV proton would penetrate D1 completely and stop in D2. A 214.9-MeV proton penetrates the entire stack with 197.7 MeV remaining.

A.2 Additional Histograms For the IAC/ISU Experiment

The following are energy deposition histograms for D2 and D3 for several trial runs that were otherwise unusable for the maximum likelihood of analysis due a lack of data for events with single particles stopping in the C scintillator. These histograms do justify the criteria set in D2 and D3 (Table 5.2) for identifying negatrons and positrons and show in part that the prototype was working. It was difficult to discerne features in the signals in the other detectors in the stack (such as D1, D4, and S).

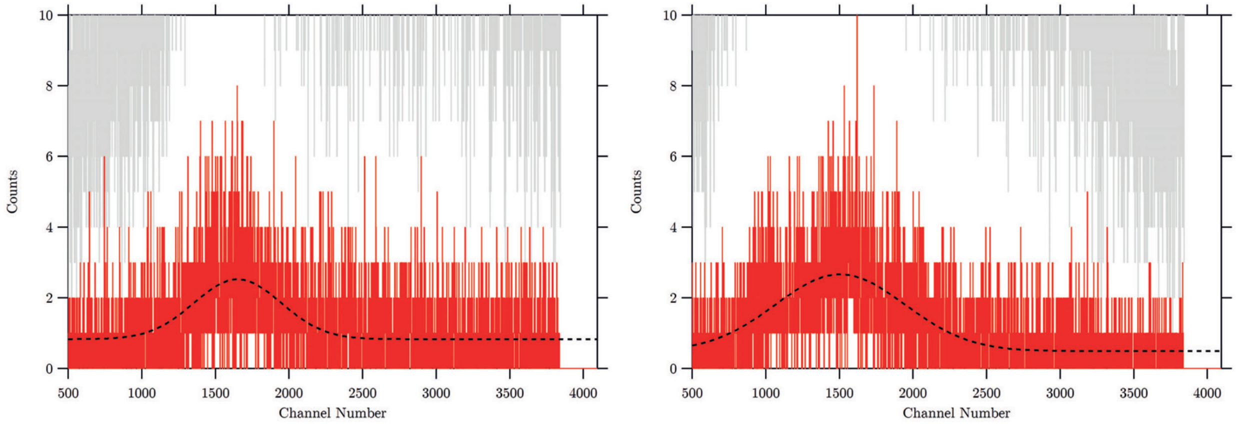

(a) D2, 6.8-MeV positrons

(b) D3, 6.8-MeV positrons

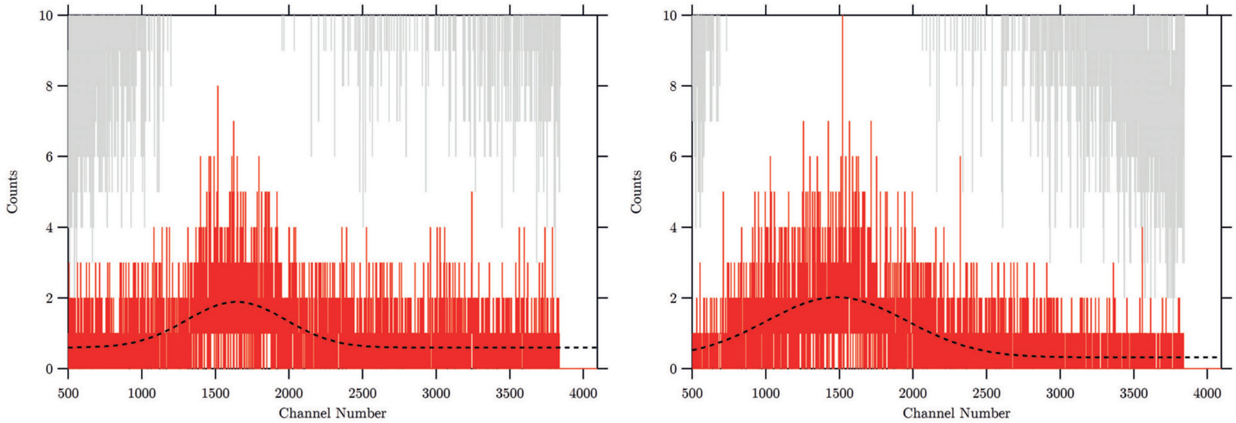

(c) D2, 6.8-MeV positrons, 12°incidence

(d) D3, 6.8-MeV positrons, 12°incidence

Figure A-1

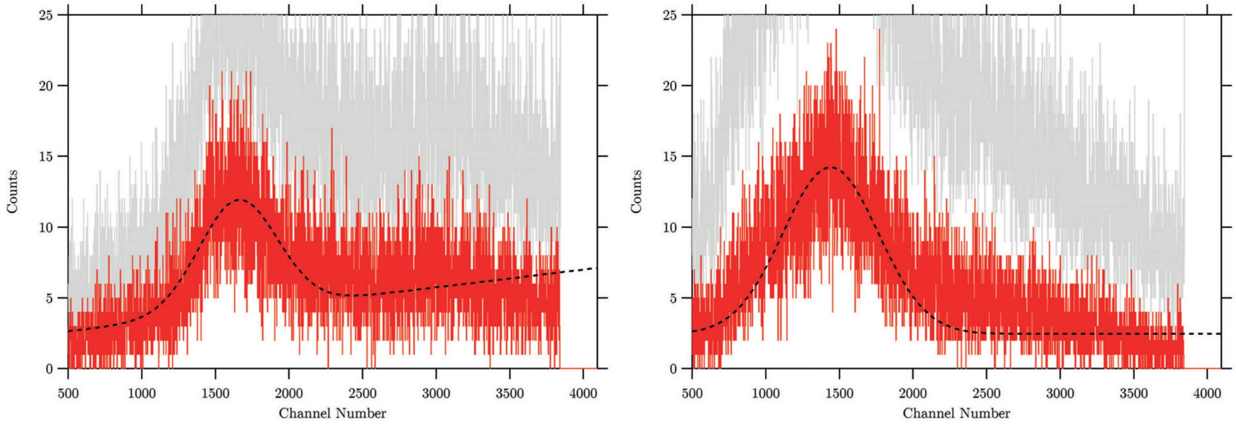

(a) D2, 5.8-MeV negatrons (b) D3, 5.8-MeV negatrons

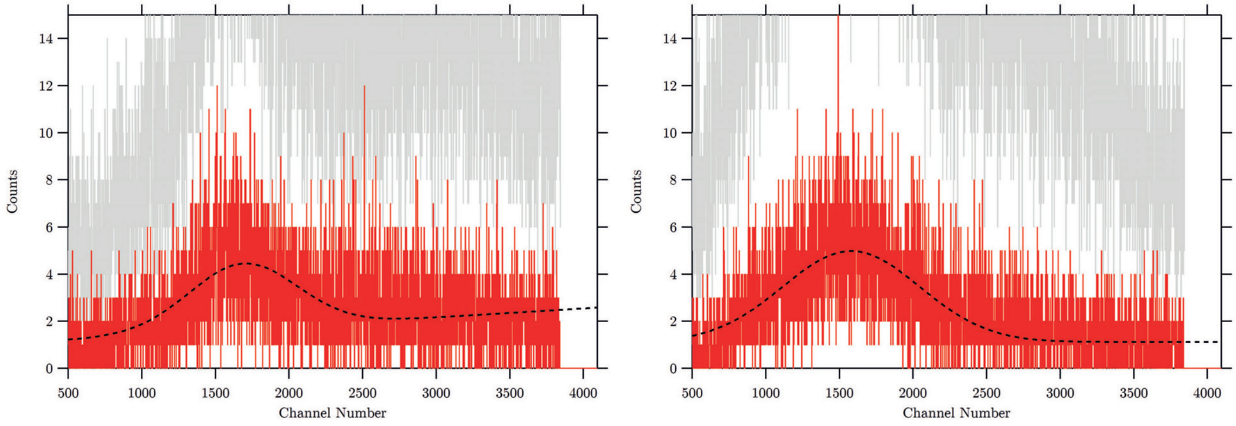

(c) D2, 5.8-MeV negatrons, 12°incidence (d) D3, 5.8-MeV negatrons, 12°incidence

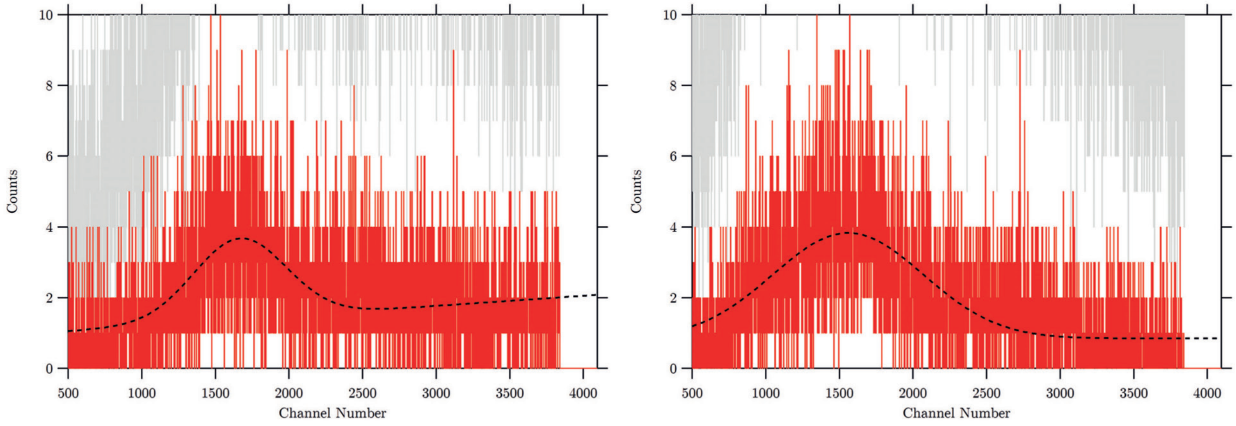

(e) D2, 6.8-MeV negatrons (f) D3, 6.8-MeV negatrons

Figure A-2

A.3 Maximum Likelihood Calculations

No. of Detectors Triggered	No. of Cases	Possible Cases (Triggered Detectors)
0	1	none
1	4	G1; G2; G3; G4
2	6	G1/G2; G1/G3; G1/G4; G2/G3; G2/G4; G3/G4
3	4	G2/G3/G4; G1/G3/G4; G1/G2/G4; G1/G2/G3
4	1	G1/G2/G3/G4

These are the total probabilities that there is a 0.511-MeV signal triggered in zero, one, two, three, and all four of the G detectors by a background γ-ray.

$$\begin{aligned}
P_b(0) &= 1G_b^0(1-G_b)^4 &&= (1-G_b)^4\\
P_b(1) &= 4G_b^1(1-G_b)^3 &&= 4G_b(1-G_b)^3\\
P_b(2) &= 6G_b^2(1-G_b)^2 &&= 6G_b^2(1-G_b)^2\\
P_b(3) &= 4G_b^3(1-G_b)^1 &&= 4G_b^3(1-G_b)\\
P_b(4) &= 1G_b^4(1-G_b)^0 &&= G_b^4
\end{aligned}$$

G_b is the probability that a background-gamma triggers a G detector. These probabilities are normalized.

We introduced an asymmetry factor A to account for the increased triggers in G1 and G2, so that $G_b \to AG_b$ for these detectors. The probabilities are calculated on a per-case basis where each case is a unique combination of G detectors triggered. The index in the superscript contains the number(s) of the detectors that are triggered in each case:

$$P_b(0) = (1 - AG_b)(1 - AG_b)(1 - G_b)(1 - G_b) = (1 - AG_b)^2(1 - G_b)^2$$

$$\begin{aligned}
P_b^{(1)}(1) &= (AG_b)(1 - AG_b)(1 - G_b)(1 - G_b) = AG_b(1 - AG_b)(1 - G_b)^2 \\
P_b^{(2)}(1) &= (1 - AG_b)(AG_b)(1 - G_b)(1 - G_b) = AG_b(1 - AG_b)(1 - G_b)^2 \\
P_b^{(3)}(1) &= (1 - AG_b)(1 - AG_b)(G_b)(1 - G_b) = G_b(1 - AG_b)^2(1 - G_b) \\
P_b^{(4)}(1) &= (1 - AG_b)(1 - AG_b)(1 - G_b)(G_b) = G_b(1 - AG_b)^2(1 - G_b)
\end{aligned}$$

$$\begin{aligned}
P_b(1) &= P_b^{(1)}(1) + P_b^{(2)}(1) + P_b^{(3)}(1) + P_b^{(4)}(1) \\
&= 2AG_b(1 - AG_b)(1 - G_b)^2 + 2G_b(1 - AG_b)^2(1 - G_b)
\end{aligned}$$

$$\begin{aligned}
P_b^{(1,2)}(2) &= (AG_b)(AG_b)(1 - G_b)(1 - G_b) = A^2G_b^2(1 - G_b)^2 \\
P_b^{(1,3)}(2) &= (AG_b)(1 - AG_b)(G_b)(1 - G_b) = AG_b^2(1 - AG_b)(1 - G_b) \\
P_b^{(1,4)}(2) &= (AG_b)(1 - AG_b)(1 - G_b)(G_b) = AG_b^2(1 - AG_b)(1 - G_b) \\
P_b^{(2,3)}(2) &= (1 - AG_b)(AG_b)(G_b)(1 - G_b) = AG_b^2(1 - AG_b)(1 - G_b) \\
P_b^{(2,4)}(2) &= (1 - AG_b)(AG_b)(1 - G_b)(G_b) = AG_b^2(1 - AG_b)(1 - G_b) \\
P_b^{(3,4)}(2) &= (1 - AG_b)(1 - AG_b)(G_b)(G_b) = G_b^2(1 - AG_b)^2
\end{aligned}$$

$$\begin{aligned}
P_b(2) &= P_b^{(1,2)}(2) + P_b^{(1,3)}(2) + P_b^{(1,4)}(2) + P_b^{(2,3)}(2) + P_b^{(2,4)}(2) + P_b^{(3,4)}(2) \\
&= A^2G_b^2(1 - G_b)^2 + 4AG_b^2(1 - AG_b)(1 - G_b) + G_b^2(1 - AG_b)^2
\end{aligned}$$

$$\begin{aligned}
P_b^{(1,2,3)}(3) &= (AG_b)(AG_b)(G_b)(1 - G_b) = A^2G_b^3(1 - G_b) \\
P_b^{(1,2,4)}(3) &= (AG_b)(AG_b)(1 - G_b)(G_b) = A^2G_b^3(1 - G_b) \\
P_b^{(1,3,4)}(3) &= (AG_b)(1 - AG_b)(G_b)(G_b) = AG_b^3(1 - AG_b) \\
P_b^{(2,3,4)}(3) &= (1 - AG_b)(AG_b)(G_b)(G_b) = AG_b^3(1 - AG_b)
\end{aligned}$$

$$\begin{aligned}
P_b(3) &= P_b^{(1,2,3)}(3) + P_b^{(1,2,4)}(3) + P_b^{(1,3,4)}(3) + P_b^{(2,3,4)}(3) \\
&= 2AG_b^3(1 - AG_b) + 2A^2G_b^3(1 - G_b)
\end{aligned}$$

$$P_b(4) = (AG_b)(AG_b)(G_b)(G_b) = A^2G_b^4$$

These probabilities are also normalized.

$$\begin{aligned}
P_p(0) &= (1 - 4G_p)(1 - 3G_p) && = (1 - 4G_p)(1 - 3G_p) \\
P_p(1) &= 2(4G_p)(1 - 3G_p) && = 8G_p(1 - 3G_p) \\
P_p(2) &= (4G_p)(3G_p) && = 12G_p^2
\end{aligned}$$

$$\begin{aligned}
P_p(0) = (1-4G_p)(1-3G_p \div F) &= (1-4G_p)\left(1-\frac{3G_p}{F}\right)\left(\frac{1}{\mathcal{N}}\right) \\
P_p(1) = 2(4G_p)(1-3G_p \times F) &= 8G_p(1-3FG_p)\left(\frac{1}{\mathcal{N}}\right) \\
P_p(2) = (4G_p)(3G_p \times F) &= 12FG_p^2\left(\frac{1}{\mathcal{N}}\right) \\
\text{where } \mathcal{N} &= (1-4G_p)\left(1-\frac{3G_p}{F}\right) + 8G_p(1-3FG_p) + 12FG_p^2
\end{aligned}$$

We obtain the probability for each specific case by dividing $P_p(0)$, $P_p(1)$, and $P_p(2)$ by one, four, and six, respectively.

$$\begin{aligned}
P'_p(0) &= (1-4G_p)\left(1-\frac{3G_p}{F}\right)\left(\frac{1}{\mathcal{N}}\right) \\
P'_p(1) &= 2G_p(1-3FG_p)\left(\frac{1}{\mathcal{N}}\right) \\
P'_p(2) &= 2FG_p^2\left(\frac{1}{\mathcal{N}}\right) \\
\text{where } \mathcal{N} &= (1-4G_p)\left(1-\frac{3G_p}{F}\right) + 8G_p(1-3FG_p) + 12FG_p^2
\end{aligned}$$

These are the per-case probabilities.

$$\begin{aligned}
P'_p(0) &= P_p(0) \\
P'_p(1) &= P_p^{(1)}(1) = P_p^{(2)}(1) = P_p^{(3)}(1) = P_p^{(4)}(1) \\
P'_p(2) &= P_p^{(1,2)}(2) = P_p^{(1,3)}(2) = P_p^{(1,4)}(2) = P_p^{(2,3)}(2) = P_p^{(2,4)}(2) = P_p^{(3,4)}(2)
\end{aligned}$$

$$\begin{aligned}
\chi_0 &= P_b(0)P_p(0) \\
\chi_1 &= P_b(0)P_p(1) + P_b(1)P_p(0) \\
\chi_2 &= P_b(0)P_p(2) + P_b(1)P_p(1) + P_b(2)P_p(0) \\
\chi_3 &= P_b(1)P_p(2) + P_b(2)P_p(1) + P_b(3)P_p(0) \\
\chi_4 &= P_b(2)P_p(2) + P_b(3)P_p(1) + P_b(4)P_p(0) \\
\chi_5 &= P_b(3)P_p(2) + P_b(4)P_p(1) \\
\chi_6 &= P_b(4)P_p(2)
\end{aligned}$$

The brute-force likelihood calculation is done by further separating each probability χ into each specific case defined by the combination of G detectors triggered. The equations are normalized as is, but when multiplying and expanding each expression, there are several cross-terms that must be removed. These cross-terms include those in which 1) the same detector is triggered more than once, 2) there are multiple permutations of a detection combination, and 3) there is a number of detectors that cannot physically be triggered. The latter terms are collectively grouped under χ_5 and χ_6, which are physically impossible given that there are only four G detectors. χ_0–χ_4 have to be renormalized by dividing like so:

$$\begin{aligned}\chi_0 + \chi_1 + \chi_2 + \chi_3 + \chi_4 + \chi_5 + \chi_6 + (\text{other terms...}) &= 1 \\ \chi_0 + \chi_1 + \chi_2 + \chi_3 + \chi_4 &= 1 - \chi_5 - \chi_6 - \ldots \\ \mathcal{N} = 1 - \chi_5 - \chi_6 - \ldots\end{aligned}$$

$$\begin{aligned}\chi_0 &= P_b(0)P_p(0) = \\ \chi_1^{(1)} &= P_p(0)P_b^{(1)}(1) + P_p(1)P_b(0) \\ \chi_1^{(2)} &= P_p(0)P_b^{(2)}(1) + P_p(1)P_b(0) \\ \chi_1^{(3)} &= P_p(0)P_b^{(3)}(1) + P_p(1)P_b(0) \\ \chi_1^{(4)} &= P_p(0)P_b^{(4)}(1) + P_p(1)P_b(0) \\ \chi_2^{(1,2)} &= P_p(0)P_b^{(1,2)}(2) + P_p(1)(P_b^{(1)}(1) + P_b^{(2)}(1)) + P_p(2)P_b(0) \\ \chi_2^{(1,3)} &= P_p(0)P_b^{(1,3)}(2) + P_p(1)(P_b^{(1)}(1) + P_b^{(3)}(1)) + P_p(2)P_b(0) \\ \chi_2^{(1,4)} &= P_p(0)P_b^{(1,4)}(2) + P_p(1)(P_b^{(1)}(1) + P_b^{(4)}(1)) + P_p(2)P_b(0) \\ \chi_2^{(2,3)} &= P_p(0)P_b^{(2,3)}(2) + P_p(1)(P_b^{(2)}(1) + P_b^{(3)}(1)) + P_p(2)P_b(0) \\ \chi_2^{(2,4)} &= P_p(0)P_b^{(2,4)}(2) + P_p(1)(P_b^{(2)}(1) + P_b^{(4)}(1)) + P_p(2)P_b(0) \\ \chi_2^{(3,4)} &= P_p(0)P_b^{(3,4)}(2) + P_p(1)(P_b^{(3)}(1) + P_b^{(4)}(1)) + P_p(2)P_b(0)\end{aligned}$$

Bibliography

O. Adriani, G. C. Barbarino, G. A. Bazilevskaya, R. Bellotti, M. Boezio, E. A. Bogomolov, M. Bongi, V. Bonvicini, S. Bottai, A. Bruno, F. Cafagna, D. Campana, P. Carlson, M. Casolino, G. Castellini, C. De Santis, V. Di Felice, A. M. Galper, A. V. Karelin, S. V. Koldashov, S. A. Koldobskiy, S. Y. Krutkov, A. N. Kvashnin, A. Leonov, V. Malakhov, L. Marcelli, M. Martucci, A. G. Mayorov, W. Menn, M. Mergé, V. V. Mikhailov, E. Mocchiutti, A. Monaco, N. Mori, R. Munini, G. Osteria, B. Panico, P. Papini, M. Pearce, P. Picozza, M. Ricci, S. B. Ricciarini, M. Simon, R. Sparvoli, P. Spillantini, Y. I. Stozhkov, A. Vacchi, E. Vannuccini, G. I. Vasilyev, S. A. Voronov, Y. T. Yurkin, G. Zampa, N. Zampa, M. S. Potgieter, and E. E. Vos. "Time Dependence of the Electron and Positron Components of the Cosmic Radiation Measured by the PAMELA Experiment between July 2006 and December 2015". *Physical Review Letters*, 116 (24):241105, June 2016. doi: 10.1103/PhysRevLett.116.241105.

M. Aguilar, G. Alberti, B. Alpat, A. Alvino, G. Ambrosi, K. Andeen, H. Anderhub, L. Arruda, P. Azzarello, A. Bachlechner, and et al. First Result from the Alpha Magnetic Spectrometer on the International Space Station: Precision Measurement of the Positron Fraction in Primary Cosmic Rays of 0.5-350 GeV. *Physical Review Letters*, 110(14):141102, April 2013. doi: 10.1103/PhysRevLett.110.141102.

I. Ahmad, S. M. Austin, B. B. Back, R. R. Betts, F. P. Calaprice, K. C. Chan, A. Chishti, P. Chowdhury, C. Conner, R. W. Dunford, J. D. Fox, S. J. Freedman, M. Freer, S. B. Gazes, J. S. Greenberg, J. P. Greene, A. L. Hallin, T. Happ, D. Henderson, N. I. Kaloskamis, E. Kashy, W. Kutschera, J. Last, C. J. Lister, M. Liu, M. R. Maier, D. M. Mercer, D. Mikolas, P. A. A. Perera, M. D. Rhein, D. E. Roa, J. P. Schiffer, T. A. Trainor, P. Wilt, J. S. Winfield, M. Wolanski, F. L. H. Wolfs, A. H. Wuosmaa, G. Xu, A. R. Young, and J. E. Yurkon. A solenoidal spectrometer for positron-electron pairs produced in heavy-ion collisions. *Nuclear Instruments and Methods in Physics Research A*, 370:539–557, February 1996. doi: 10.1016/0168-9002(95)00829-2.

AMS. First results from the alpha magnetic spectrometer (ams) experiment. *AMS-02 Press Releases*, Apr 2013. URL `http://www.ams02.org/wp-content/uploads/2013/04/Press_AMS_en.pdf`.

W. H. Barkas and M. J. Berger. Tables of Energy Losses and Ranges of Heavy Charged Particles. NASA SP-3013. *NASA Special Publication*, 3013, 1964.

W. H. Barkas, J. N. Dyer, and H. H. Heckman. Resolution of the Σ^--Mass Anomaly. *Physical Review Letters*, 11:26–28, July 1963. doi: 10.1103/PhysRevLett.11.26.

M. J. Berger, J. H. Hubbell, S. M. Seltzer, J. Chang, J. S. Coursey, R. Sukumar, D. S. Zucker, and K Olsen. Xcom: Photon cross section database (version 1.5). [online]. Nov 2010. URL `https://www.nist.gov/pml/xcom-photon-cross-sections-database`.

M. J. Berger, J. S. Coursey, M. A. Zucker, and J Chang. Estar, pstar, and astar: Computer programs for calculating stopping-power and range tables for electrons, protons, and helium ions (version 2.0.1). [online]. Jul 2017. URL `http://physics.nist.gov/Star`.

B. B. Bickford. Picap final report, 2012.

J. B. Birks. *The Theory And Practice Of Scintillation Counting.* Pergamon, 1964. ISBN 9781483156064.

H. V. Cane and W. C. Erickson. Energetic particle propagation in the inner heliosphere as deduced from low-frequency (<100 kHz) observations of type III radio bursts. *Journal of Geophysical Research*, 108:1203, May 2003. doi: 10.1029/2002JA009488.

E. L. Chupp, D. J. Forrest, P. R. Higbie, A. N. Suri, C. Tsai, and P. P. Dunphy. Solar Gamma Ray Lines observed during the Solar Activity of August 2 to August 11, 1972. *Nature*, 241:333–335, February 1973. doi: 10.1038/241333a0.

J. Clem and P. Evenson. Cosmic Ray Positron Fraction Observations during the A- Magnetic Solar Minimum. *International Cosmic Ray Conference*, 1:477–480, 2008.

J. M. Clem, P. Evenson, D. Huber, R. Pyle, C. Lopate, and J. A. Simpson. Charge sign dependence of cosmic ray modulation near a rigidity of 1 GV. *Journal of Geophysical Research*, 105:23099–23106, October 2000. doi: 10.1029/2000JA000097.

T. L. Cline and E. W. Hones. Interplanetary positrons near 1 MeV from other than the $\pi \rightarrow \mu \rightarrow$ e process. *International Cosmic Ray Conference*, 1:159, 1970.

T. L. Cline and G. Porreca. Cosmic ray electrons and positrons of energies 2 to 9. 5 MeV observed in interplanetary space. *International Cosmic Ray Conference*, 1:145, 1970.

J. J. Connell, J. R. Kalainoff, and C. Lopate. Design concept and modeling of a new Positron Identification by Coincident Annihilation Photons (PICAP) system. *Nuclear Instruments and Methods in Physics Research A*, 593:431–439, August 2008. doi: 10.1016/j.nima.2008.05.051.

J. K. Daugherty, R. C. Hartman, and P. J. Schmidt. A measurement of cosmic-ray positron and negatron spectra between 50 and 800 MV. *The Astrophysical Journal*, 198:493–505, June 1975. doi: 10.1086/153626.

S. E. S. Ferreira, M. S. Potgieter, R. A. Burger, B. Heber, H. Fichtner, and C. Lopate. Modulation of Jovian and galactic electrons in the heliosphere: 2. Radial transport of a few MeV electrons. *Journal of Geophysical Research*, 106:29313–29322, December 2001. doi: 10.1029/2001JA000170.

G. J. Fishman, P. N. Bhat, R. Mallozzi, J. M. Horack, T. Koshut, C. Kouveliotou, G. N. Pendleton, C. A. Meegan, R. B. Wilson, W. S. Paciesas, S. J. Goodman, and H. J. Christian. Discovery of Intense Gamma-Ray Flashes of Atmospheric Origin. *Science*, 264:1313–1316, May 1994. doi: 10.1126/science.264.5163.1313.

A. M. Galper, R. Sparvoli, O. Adriani, G. Barbarino, G. A. Bazilevskaya, R. Bellotti, M. Boezio, E. A. Bogomolov, M. Bongi, V. Bonvicini, S. Bottai, A. Bruno, F. Cafagna, D. Campana, P. Carlson, M. Casolino, G. Castellini, C. De Donato, C. De Santis, V. Di Felice, A. V. Karelin, S. V. Koldashov, S. A. Koldobskiy, S. Y. Krutkov, A. N. Kvashnin, A. A. Leonov, V. V. Malakhov, L. Marcelli, M. Martucci, A. G. Mayorov, W. Menn, M. Mergè, V. V. Mikhailov, E. Mocchiutti, N. Mori, R. Munini, G. Osteria, F. Palma, B. Panico, P. Papini, M. Pearce, P. Picozza, M. Ricci, S. B. Ricciarini, M. Simon, P. Spillantini, Y. I. Stozhkov, A. Vacchi, E. Vannuccini, G. I. Vasilyev, S. A. Voronov, Y. T. Yurkin, G. Zampa, and N. Zampa. The PAMELA experiment: a decade of Cosmic Ray Physics in space. In *Journal of Physics Conference Series*, volume 798 of *Journal of Physics Conference Series*, page 012033, January 2017. doi: 10.1088/1742-6596/798/1/012033.

D. E. Groom, N. V. Mokhov, and S. I. Striganov. Muon Stopping Power and Range Tables 10 MeV-100 TeV. *Atomic Data and Nuclear Data Tables*, 78:183–356, July 2001. doi: 10.1006/adnd.2001.0861.

G. J. Hurford, R. A. Mewaldt, E. C. Stone, and R. E. Vogt. Measurements of the Flux of Low-Energy Solar-Flare Positrons. *International Cosmic Ray Conference*, 2:1613, 1973.

J. D. Jackson. *Classical Electrodynamics*. John Wiley & Sons, Inc., 3rd edition, 1999. ISBN 9780471309321.

J. R. Jokipii and E. H. Levy. Effects of particle drifts on the solar modulation of galactic cosmic rays. *The Astrophysical Journal*, 213:L85–L88, April 1977. doi: 10.1086/182415.

J. R. Jokipii, E. H. Levy, and W. B. Hubbard. Effects of particle drift on cosmic-ray transport. I - General properties, application to solar modulation. *The Astrophysical Journal*, 213:861–868, May 1977. doi: 10.1086/155218.

E. Kirsch, E. Keppler, and K. Richter. Possible detection of flare-generated positrons by HELIOS 1 on 3 Jun 1982. *International Cosmic Ray Conference*, 4, August 1985.

A. Kounine. The Alpha Magnetic Spectrometer on the International Space Station. *International Journal of Modern Physics E*, 21:1230005, August 2012. doi: 10.1142/S0218301312300056.

W. R. Leo. *Techniques for Nuclear and Particle Physics Experiments: A How-to Approach*. Springer-Verlag, 2nd edition, 1994. ISBN 3540572805.

C. Lopate. Jovian and Galactic Electrons (2-30 MeV) in the Heliosphere from 1 to 50AU. *International Cosmic Ray Conference*, 2:149, August 1991.

R. A. Mewaldt, E. C. Stone, and R. E. Vogt. A search for solar flare positrons. *International Cosmic Ray Conference*, 5:1668–1673, August 1975.

R. J. Murphy, C. D. Dermer, and R. Ramaty. High-energy processes in solar flares. *The Astrophysical Journal Supplement Series*, 63:721–748, March 1987. doi: 10.1086/191180.

W.R. Nelson, Hideo Hirayama, and D.W.O. Rogers. Egs4 code system. *SLAC Report No. SLAC-265*, 12 1985.

A. Ore and J. L. Powell. Three-Photon Annihilation of an Electron-Positron Pair. *Physical Review*, 75:1696–1699, June 1949. doi: 10.1103/PhysRev.75.1696.

E. N. Parker. The passage of energetic charged particles through interplanetary space. *Planetary and Space Science*, 13:9–49, January 1965. doi: 10.1016/0032-0633(65)90131-5.

P. Picozza, A. M. Galper, G. Castellini, O. Adriani, F. Altamura, M. Ambriola, G. C. Barbarino, A. Basili, G. A. Bazilevskaja, R. Bencardino, M. Boezio, E. A. Bogomolov, L. Bonechi, M. Bongi, L. Bongiorno, V. Bonvicini, F. Cafagna, D. Campana, P. Carlson, M. Casolino, C. de Marzo, M. P. de Pascale, G. de Rosa, D. Fedele, P. Hofverberg, S. V. Koldashov, S. Y. Krutkov, A. N. Kvashnin, J. Lund, J. Lundquist, O. Maksumov, V. Malvezzi, L. Marcelli, W. Menn, V. V. Mikhailov, M. Minori, S. Misin, E. Mocchiutti, A. Morselli, N. N. Nikonov, S. Orsi, G. Osteria, P. Papini, M. Pearce, M. Ricci, S. B. Ricciarini, M. F. Runtso, S. Russo, M. Simon, R. Sparvoli, P. Spillantini, Y. I. Stozhkov, E. Taddei, A. Vacchi, E. Vannuccini, S. A. Voronov, Y. T. Yurkin, G. Zampa, N. Zampa, and V. G. Zverev. PAMELA A payload for antimatter matter exploration and light-nuclei astrophysics. *Astroparticle Physics*, 27:296–315, April 2007. doi: 10.1016/j.astropartphys.2006.12.002.

M. S. Potgieter. Solar Modulation of Cosmic Rays. *Living Reviews in Solar Physics*, 10:3, June 2013. doi: 10.12942/lrsp-2013-3.

R. Ramaty and N. Mandzhavidze. *Solar Flares: Gamma Rays*, page 2292. November 2000. doi: 10.1888/0333750888/2292.

R. Ramaty, R. J. Murphy, B. Kozlovsky, and R. E. Lingenfelter. Gamma-ray lines and neutrons from solar flares. *Solar Physics*, 86:395–407, July 1983. doi: 10.1007/BF00157213.

D. V. Reames. Particle acceleration at the Sun and in the heliosphere. *Space Science Reviews*, 90: 413–491, October 1999. doi: 10.1023/A:1005105831781.

G. H. Share and R. J. Murphy. Gamma-Ray Measurements of Flare-to-Flare Variations in Ambient Solar Abundances. *The Astrophysical Journal*, 452:933, October 1995. doi: 10.1086/176360.

J. A. Simpson. Elemental and Isotopic Composition of the Galactic Cosmic Rays. *Annual Review of Nuclear and Particle Science*, 33:323–382, 1983. doi: 10.1146/annurev.ns.33.120183.001543.

J. D. Sullivan. Geometrical factor and directional response of single and multi-element particle telescopes. *Nuclear Instruments and Methods*, 95:5, 1971. doi: 10.1016/0029-554X(71)90033-4.

A. H. Wuosmaa, I. Ahmad, S. M. Fischer, J. P. Greene, G. Hackman, V. Nanal, G. Savard, J. P. Schiffer, P. Wilt, S. M. Austin, B. A. Brown, S. J. Freedman, and J. J. Connell. β^+ Decay Partial Half-Life of ^{54}Mn and Cosmic Ray Chronometry. *Physical Review Letters*, 80:2085–2088, March 1998. doi: 10.1103/PhysRevLett.80.2085.

M. Yoshimori, K. Suga, S. Nakayama, and H. Ogawa. Positron annihilation radiation and $>$ 10 MeV gamma-rays from the 1997 November 6 flare. *International Cosmic Ray Conference*, 8: 3025, August 2001.